Electronic Properties of Bilayer Graphene in a Steady Magnetic Field

Narjes Kheirabadi

PhD Thesis

Submitted for the degree of Doctor of Philosophy

January 16, 2018

Declaration

Publication based on chapters 3 and 5

N. Kheirabadi, E. McCann and V. I. Fal'ko. *Magnetic ratchet effect in bilayer graphene*. Phys. Rev. B **94**, 165404 (2016).

Preprint based on chapter 4

N. Kheirabadi, E. McCann. *Lifshitz transition in bilayer graphene under in–plane magnetic field*. Unpublished.

Preprint based on chapter 6

N. Kheirabadi, E. McCann, and V. I. Fal'ko. *Second harmonic generation current in bilayer graphene under in–plane magnetic field*. Unpublished.

N. Kheirabadi

January 16, 2018

Abstract

In this thesis, we consider the electronic properties of bilayer graphene in a steady, parallel magnetic field. Using the tight–binding model, and taking into account relevant tight–binding parameters, we find a new contribution to the electronic Hamiltonian describing the orbital effect of the magnetic field.

We consider the effect of the magnetic field on the Lifshitz transition, in which the Fermi surface breaks up into separate pockets at very low energy, due to trigonal warping. We show that the predicted band structure is dramatically altered when taking the new magnetic field contribution into account.

We consider the effect of the magnetic field on non–linear dynamics in the presence of an ac laser field and spatial inversion asymmetry. Bilayer graphene is particularly interesting from this point of view because inversion symmetry can be broken either through asymmetry of disorder, the presence of a substrate or through interlayer asymmetry induced by an external gate voltage, the latter yielding tunable non–linear properties. Using the Boltzmann transport equation, we determine the intraband contribution to the dc current, known as the magnetic ratchet effect, and the second harmonic current. We also take into account a perpendicular magnetic field component, which produces cyclotron motion and cyclotron resonance. We discuss the dependence of these non–linear currents on the polarisation of light, the direction of the in–plane field, and the cyclotron frequency.

Acknowledgment

First of all, a big thanks to my God.

Second, I thank Dr. McCann because of his attempts and patience during my PhD for my progress. Third, I appreciate Prof. Fal'ko as being the supervisor of the work in the beginning and his precious scholarship.

With a very especial thanks to my parents and my brother because of their support during the last three years.

I also appreciate John Wallbank because of useful discussions with him.

Contents

List of Figures

Chapter 1

Introduction

This thesis is about the electronic properties of bilayer graphene and, in particular, the orbital effect of an in–plane magnetic field on them. The main discovery is a new contribution to the low–energy Hamiltonian arising from the magnetic field. Subsequently, we model the influence of this contribution on the electronic band structure, focussing on a low–energy feature known as the Lifshitz transition, as well as its influence on electronic scattering that produces an intraband contribution to nonlinear optical processes (dc current and second harmonic generation). This introductory chapter sets the scene by providing background information about graphene (monolayer and bilayer), the Lifshitz transition, and the non–linear optical properties of graphene.

1.1 Graphene

1.1.1 Monolayer Graphene

Carbon has many different physical forms, including diamond, graphite, and amorphous carbon. Diamond and graphite have been known since ancient times. Fullerene, the third form of carbon, was discovered in 1985 by Kroto et al.[1], and carbon nanotubes (CNTs) were discovered in 1991 by Iijima [2]. Thus, only three–dimensional (3D) (diamond and graphite), one–dimensional (1D; CNTs),

and zero–dimensional (0D; fullerenes) allotropes of carbon were known in the carbon community (Fig. 1.1). Although it was realized in 1991 that carbon nanotubes

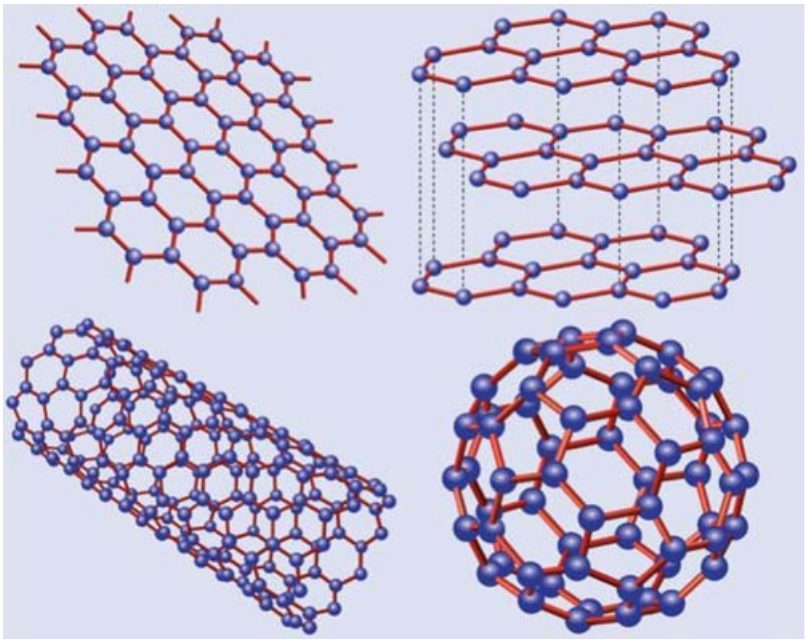

Figure 1.1: Graphene, top left, is a hexagonal lattice of carbon atoms. Graphite, top right, includes graphene layers, carbon nanotubes are rolled–up tubes of graphene, bottom left. Fullerenes, are molecules consisting of wrapped graphene by the introduction of pentagons on the hexagonal lattice. Figure taken from AH Casto Neto et al, Rev Mod. Phys. **81**, 109 (2009).

are effectively a rolled up two–dimensional (2D) graphene sheet, which is single layer of a 3D graphitic crystal, the isolation of graphene itself was quite elusive, resisting any attempt until 2004 [3].

Theoretically, graphene was studied first by Wallace [4] over 60 years ago when he wanted to understand the electronic properties of graphite. The issue with graphene was its fabrication, until 2004, when Geim and Novoselov fabricated graphene monolayers and multilayers in the laboratory. This experimental step led to the Nobel prize for physics [5].

After the initial production of graphene by mechanical exfoliation, different methods have been invented to fabricate graphene. As an example, large–area uniform polycrystalline graphene films are now being grown by chemical vapour deposition on copper foils and films, and show promise for many applications [6]. Other ways to produce graphene are epitaxial growth of graphene on silicon carbide (SiC), chemically derived graphene and graphene produced by electrochem-

ical exfoliation [7]. Typically, graphene characterisation can be done by transmission electron microscopy, scanning tunnelling microscopy, Raman spectroscopy and photoemission [7].

Graphene is a very good candidate for electronic devices because of its high electrical mobility [8] and the possibility to control its Fermi level using a metallic back gate. This two–dimensional allotrope of carbon also serves as the basis for the understanding of the electronic properties of other allotropes.

Moreover, graphene has high mechanical strength [9], its charge carriers behave like massless Dirac fermions with a linear dispersion relation [10], and it is a tunable optical material [11]. In addition, graphene has also been considered and intensively researched for high frequency transistor applications [12]. In fact, as graphene possesses degrees of freedom related to charge, pseudospin, spin and valley [13; 14], different types of transistor can be fabricated in the laboratory.

Scattering mechanisms including Coulomb scattering, lattice disorder scattering and electron-phonon scattering play roles in realistic graphene devices [7]. In addition, in this two–dimensional material, Dirac fermions behave in unusual ways when compared to ordinary electrons if subjected to magnetic fields [15], leading to new physical phenomena, such as the anomalous integer quantum Hall effect [5; 16], in which the sequence of steps in the conductance is shifted by $1/2$ in units of conductance quantum with respect to the standard sequence [13].

1.1.2 Bilayer Graphene

Bilayer graphene [5] is a material consisting of two coupled layers of graphene where the layers are exactly aligned (AA stacked) or where half of the atoms lie directly over the centre of a hexagon in the lower graphene sheet, Bernal–stacked form (AB–stacked)(Fig. 1.2). It has been shown that the AB–stacked arrangement is more stable than the AA one [17]. In this thesis, we study AB–stacked bilayer graphene.

Bilayer graphene has four atoms in its unit cell as the result of there being

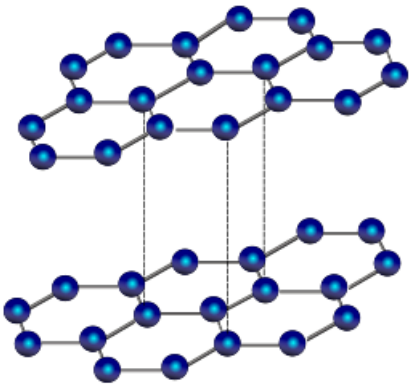

Figure 1.2: AB–Stacked Bilayer graphene. Half of the atoms in the upper graphene sheet lie directly over the centre of a hexagon in the lower graphene sheet

two coupled layers. The band gap of bilayer graphene is generally zero, so it is a semimetal. It displays fascinating electronic properties including pseudospin and chirality. Pseudospin means that there is a twofold lattice degree of freedom hat acts like spin 1/2, chirality means that the pseudospin direction is related to the direction of the electronic momentum [18; 19; 20]. In addition, for bilayer graphene, there is the possibility to create and tune a gap between the conduction and the valence bands using potential asymmetry of the layers [19] which makes it a new material for applications.

Lifshitz transition

The band structure of bilayer graphene is quadratic at low energy, the Fermi level can be changed using external gates, and the band structure can be modified by external perturbations [21]. In monolayer and bilayer graphene, there is a triangular–shaped distortion of the Fermi circle, known as trigonal warping. In bilayer graphene this is particularly strong at very low energy. This change of Fermi surface is so much that, within a few meV of the change neutrality point, the distorted circle breaks into four different pockets; a process known as a Lifshitz transition (Fig. 1.3). More details about the Lifshitz transition will come in Chapter 4.

Chapter 2 describes the tight–binding model of bilayer graphene and, in Chapter 3, we take into account the effect of an in–plane magnetic field. The influence

of their field on the Lifshitz transition is described in Chapter 4.

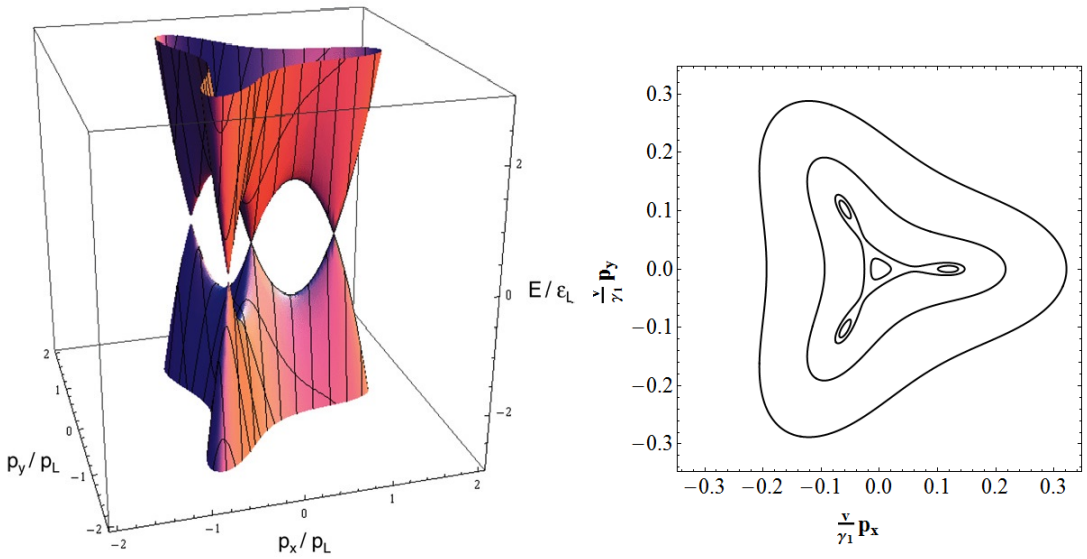

Figure 1.3: Left: The electronic structure of bilayer graphene, where a Lifshitz transition as the result of trigonal warping is depicted for $\epsilon_L = 1$ meV. Figure taken From E McCann et al, Rep.Prog.Phys.**76**, 056503 (2013). Right: Numerical calculations showing constant energy contours as described in Chapter 4. Parameter values are constant energy contours in $\left(\nu p_x/\gamma_1, \nu p_y/\gamma_1\right)$ for $\epsilon/\gamma_1 = -0.002$, $\epsilon/\gamma_1 = -0.004$, $\epsilon/\gamma_1 = -0.020$, and $\epsilon/\gamma_1 = -0.059$.

1.2 Nonlinear Optics

For a linear optical device the current of density **J** produced under an applied electric field **E** is proportional to that electric field:

$$J_i = \sum_j \sigma_{ij}^{(1)} E_j \tag{1.1}$$

where $\sigma_{ij}^{(1)}$ is the first order conductivity tensor element, i, j are Cartesian spatial indices. For a non–linear device, however, the produced current under an applied electric field can be written as an expansion in powers of the electric field:

$$J_i = \sum_j \sigma_{ij}^{(1)} E_j + \sum_{jk} \sigma_{ijk}^{(2)} E_j E_k + \sum_{jkl} \sigma_{ijkl}^{(3)} E_j E_k E_l + ... \tag{1.2}$$

where $\sigma_{ijk}^{(2)}$ and $\sigma_{ijkl}^{(3)}$ are second and third order conductivity tensor elements, respectively.

Nonlinear optical effects were studied in 1870 by John Kerr. He demonstrated that the refractive index of a number of solids and liquids is slightly changed by the application of a strong dc field; this phenomenon is named the dc Kerr effect [22].

In order to observe second order effects, spatial inversion should be broken because, under inversion symmetry, the current is odd while the second order term in electric field is even.

Different physical regimes for optics in graphene are determined by the ratio of the Fermi energy to the photon energy, Fig. 1.4. At zero temperature, we consider the photon energy $\hbar\omega$, $\hbar$ is the Planck constant and ω is angular frequency, the highest occupied energy level is the Fermi energy E_F, Dirac point is zero of energy and τ^{-1} is the scattering rate of electrons. For a typical value of the Fermi energy in graphene, of the order of 100 to 400 meV, if $\omega \leq E_F/\hbar$, the transition is intraband and electron dynamics can be described semiclassically by the Boltzmann kinetic equation, Fig. 1.4 (c). An energy of 100 meV corresponds to radiation of angular frequency 152 Trad/s and a linear frequency equal to 24.25 THz which is in the mid–infrared range of the light spectrum.

For $E_F/\hbar \leq \omega \leq 2E_F/\hbar$ the transition is an indirect interband one and classical and quantum results emerge. Finally, for $\omega \geq 2E_F/\hbar$, direct interband transitions happen.

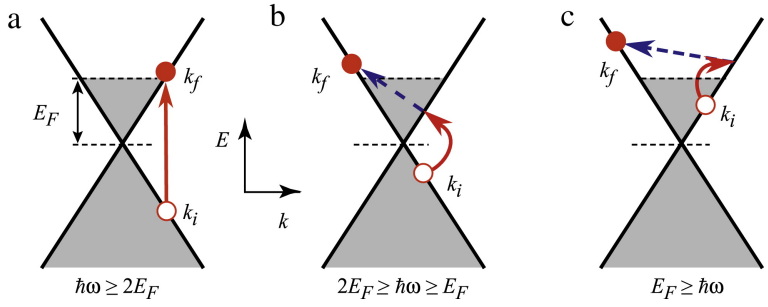

Figure 1.4: Schematic diagram of the possible optical transitions in graphene: (a) direct interband transition, (b) indirect interband transition, (c) indirect intraband transition. Solid and dashed arrows show electron–photon interaction (solid arrows) and electron scattering caused by impurities or phonons (dashed arrows). Initial and final states of a photoexcited carrier with wave vectors k_i and k_f are shown by open and solid circles, respectively. Inequalities define the corresponding photon energy ranges. Figure taken from MM Glazov, et al. Phys. Rep. **535**, 101 (2009).

Graphene shows remarkable optical properties. For example, it can be optically visualized despite being only a single atom thick [23; 24; 25]. Graphene produces an unexpectedly high opacity for an atomic monolayer in vacuum, and the fine structure constant defines the visual transparency of graphene, for example it absorbs $\pi\alpha \approx 2.3\%$ of red light, where α is the fine–structure constant. Such a high absorbency of light makes it visible to the naked eye [26](Fig. 1.5, left). In addition, its light transmittance is linear over most of the visible spectrum (Fig. 1.5) [26; 27; 28].

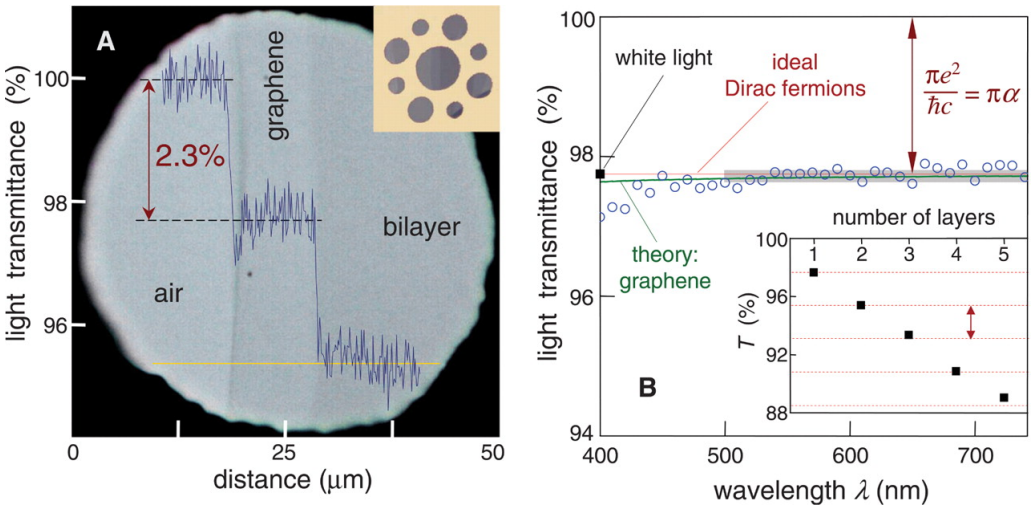

Figure 1.5: (A) Figure of a 50 μm space partially covered by graphene and its bilayer. The line scan profile shows the intensity of transmitted white light along the yellow line. (B) Transmittance spectrum of single–layer graphene (open circles). The red line is the transmittance expected for two–dimensional Dirac fermions and it is linear, whereas the green curve takes into account a nonlinearity and triangular warping of graphene's electronic spectrum. The gray area indicates the standard error for the measurements. (Inset) Transmittance of white light as a function of the number of graphene layers (squares). Figure taken from RR Nair et al, Science **6**, 1308 (2008).

In this thesis, we study two nonlinear optical effects, first, the magnetic quantum ratchet effect, then, second harmonic generation. In the quantum ratchet effect an optical device produces a dc current under the ac electric field of laser light. It is called a "ratchet" because the electronic device makes a dc current from an oscillating electric field. To have this effect, spatial symmetry should be broken because it is a second order effect [29; 30].

Another nonlinear optical effect is second harmonic generation. In this phenomenon, photons with the same frequency interacting with a nonlinear mate-

rial are effectively combined to generate new photons with twice the energy, and therefore twice the frequency. Historically, second harmonic generation was not discovered until there was a source of strong optical frequency fields, namely, the laser, which occured in 1961 at Michigan University [22; 31; 32; 33].

Finally, we consider some parameter values. First of all, in this thesis we consider that the typical photon energy is from the mid infrared, 124 meV, to microwave and radiowaves 12.4neV; hence the regime of the work is semiclassical and we can use Boltzmann kinetic equations and intraband optical processes happen (Fig. 1.4) (c). Moreover, the graphene Fermi energy order is around 100 to 400 meV [29]. In the whole of this thesis we also assume that $E_F \gg \hbar\tau^{-1}$ so that electrons are long–lived quasiparticles and that $E_F \gg k_B T$, so that electrons form a degenerate gas, k_B is the Boltzmann constant and T is temperature.

1.3 The content of the thesis

This thesis has seven Chapters. After this introduction, in the second Chapter, the theoretical background to the work is reviewed, namely, the graphene structure, its reciprocal lattice, and the tight–binding model are described. Then, the structure of bilayer graphene is depicted and it is shown that the four component electronic Hamiltonian of bilayer graphene may be written as a two component one at low energy.

In Chapter 3, the tight–binding Hamiltonian of bilayer graphene in the presence of an in–plane magnetic field is derived. In this Chapter, by considering skew interlayer coupling, we have found a new term in the bilayer graphene Hamiltonian.

In Chapter 4, the influence of the in–plane magnetic field on the electronic band structure is described. In particular we show how it has a profound effect on the Lifshitz transition.

Chapter 5 describes the role that in–plane magnetic field plays in creating an interband contribution to a non–linear optical effect, namely, the production of a dc current in the magnetic field.

In the sixth Chapter, the ac current produced by the magnetic ratchet is determined including first and second harmonics. Consequently, the deduced ac current is related to linear and nonlinear optics, respectively.

Finally, in the last Chapter, a general conclusion of the original material of this thesis is provided.

Chapter 2

Theoretical background

2.1 Introduction

To determine the tight–binding Hamiltonian of a crystal, its Bravais lattice should be known. Graphene is *not* a Bravais lattice, but, by considering two sublattices, A and B, the graphene honeycomb lattice can be viewed as two triangular Bravais lattices [15] (Fig. 2.1). Based on this point of view, the primitive lattice vectors

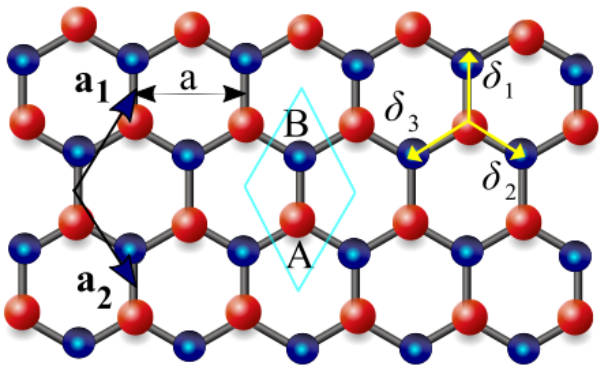

Figure 2.1: The honeycomb lattice of monolayer graphene. The red (blue) spheres indicate A (B) sublattices, while the solid lines between atoms represent covalent bands. The blue rhombus shows the unit cell of monolayer graphene unit cell, which includes two sublatices. Accordingly, δ_i vectors, ($i = 1$ to 3) for three nearest neighbours of a typical A sublattice have been depicted.

are $\mathbf{a}_1 = a\left(1/2, \sqrt{3}/2\right)$ and $\mathbf{a}_2 = a\left(1/2, -\sqrt{3}/2\right)$ where $a = 2.46\mathring{A}$ is the graphene lattice constant [34]. Furthermore, each carbon atom has one electron in its free p_z orbital; so, each carbon atom contributes one electron to the low–energy bands. As a result, the monolayer graphene Hamiltonian should be a 2×2 matrix. In addition, the triangular Bravais lattice results in a triangular reciprocal lattice.

The primitive vectors in the reciprocal lattice space satisfying $\mathbf{a_i} \cdot \mathbf{b_j} = 2\pi\delta_{ij}$ are (Fig. 2.2)

$$\mathbf{b}_1 = \left(\frac{2\pi}{a}, \frac{2\pi}{\sqrt{3}a}\right), \quad \mathbf{b}_2 = \left(\frac{2\pi}{a}, -\frac{2\pi}{\sqrt{3}a}\right). \tag{2.1}$$

The symmetry lines in the reciprocal lattice of monolayer graphene are the $\Gamma - K$, $\Gamma - M$ and $K - M$ lines (Fig. 2.2). At special points in the Brillouin zone, the group of the wave vector may be larger than that on symmetry lines which thread it; these are called symmetry points [35; 36]. The symmetry points in graphene are point Γ, the centre of the Brilloiun zone points, points K which are corners of the Brilloiun zone and points M which are the centres of the edge of the Brillouin zone [37]. There are two types of K points in the reciprocal lattice named as k_+

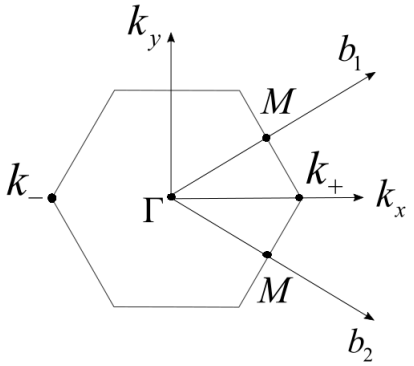

Figure 2.2: The reciprocal lattice of monolayer graphene where $\mathbf{b}_1$ and $\mathbf{b}_2$ are primitive lattice vectors. The $k_\pm$ symmetry points are located in the corners of the first Brillouin zone, Γ is in the centre of the first Brillouin zone, and M points are located in the centres of the edge of the Brillouin zone.

and k_- valleys. By use of primitive vectors in the reciprocal lattice, it is possible to show that the wave vector corresponding to point k_ξ valley is

$$k_\xi = \xi\left(\frac{4\pi}{3a}, 0\right), \tag{2.2}$$

where $\xi = \pm 1$ is a valley index.

2.2 General tight–binding model

The eigenstates of the one–electron Hamiltonian, $\hat{H} = -\hbar^2\nabla/2m + U(\mathbf{r})$, where potential $U(\mathbf{r}+\mathbf{R}) = U(\mathbf{r})$ for all $\mathbf{R}$ in a Bravais lattice, can be chosen to have the form of a plane wave times a function with the periodicity of the Bravais lattice [38]:

$$\psi_{n\mathbf{k}}(\mathbf{r}) = e^{i\mathbf{k}\cdot\mathbf{r}} u_{n\mathbf{k}}(\mathbf{r}). \tag{2.3}$$

This is Bloch's theorem and it is the basis of our work. For our case of study consider a system with n atomic orbitals ϕ_j $(j = 1...n)$ in the unit cell. We will use Bloch functions with a periodic function related to the molecular orbitals in a unit cell, and an exponential function which describes a plane wave [13; 38]. The form of this Bloch wave function is:

$$\Phi_j(\mathbf{k}, \mathbf{r}) = \frac{1}{\sqrt{N}} \sum_{i=1}^{N} e^{i\mathbf{k}\cdot\mathbf{R}_{j,i}} \phi_j(\mathbf{r} - \mathbf{R}_{j,i}), \tag{2.4}$$

where the sum is over N different unit cells, labelled by index $i = 1...N$, $\mathbf{r}$ is the position vector and $\mathbf{k}$ is the wave vector of the Bloch wave function. Coordinate $\mathbf{R}_{j,i}$ denotes the position of the jth orbital in the ith unit cell. Within tight binding theory, an electronic wave function $\Psi_j(\mathbf{k}, \mathbf{r})$ is given by a linear superposition of n different Bloch functions

$$\Psi_j(\mathbf{k}, \mathbf{r}) = \sum_{l=1}^{n} c_{j,l}(\mathbf{k}) \Phi_l(\mathbf{k}, \mathbf{r}), \tag{2.5}$$

where $c_{j,l}$ are coefficients of the expansion. The energy $E_j(\mathbf{k})$ of the jth band is given by

$$E_j(\mathbf{k}) = \frac{\langle \Psi_j \mid H \mid \Psi_j \rangle}{\langle \Psi_j \mid \Psi_j \rangle}, \tag{2.6}$$

where H is the Hamiltonian. Substituting the expansion of the wave function (Eq. 2.5) into the energy gives

$$E_j(\mathbf{k}) = \frac{\sum_{i,l}^{n} c_{ji}^{*} c_{jl} \langle \Phi_i \mid H \mid \Phi_l \rangle}{\sum_{i,l}^{n} c_{ji}^{*} c_{jl} \langle \Phi_j \mid \Phi_l \rangle}, \tag{2.7}$$

$$= \frac{\sum_{i,l}^{n} H_{i,l} c_{ji}^{*} c_{jl}}{\sum_{i,l}^{n} S_{il} c_{ji}^{*} c_{jl}}, \tag{2.8}$$

where the transfer integral matrix elements H_{il} and overlap integral matrix elements S_{il} are defined by

$$H_{il} = \langle \Phi_i \mid H \mid \Phi_l \rangle , \qquad S_{il} = \langle \Phi_i \mid \Phi_l \rangle . \tag{2.9}$$

We minimize the energy E_j with respect to the coefficient c_{jm}^{*} and set $\partial E_j / \partial c_{jm}^{*} = 0$ by calculating the derivative,

$$\frac{\partial E_j}{\partial c_{jm}^{*}} = \frac{\sum_{l}^{n} H_{ml} c_{jl}}{\sum_{i,l}^{n} S_{il} c_{ji}^{*} c_{jl}} - \frac{\sum_{i,l}^{n} H_{il} c_{ji}^{*} c_{jl} \sum_{l}^{n} S_{ml} c_{jl}}{\left(\sum_{i,l}^{n} S_{il} c_{ji}^{*} c_{jl} \right)^2}. \tag{2.10}$$

The second term contains a factor equal to energy E_j itself Eq. 4.16. Then, by setting $\partial E_j / \partial c_{jm}^{*} = 0$, we find

$$\sum_{l=1}^{n} H_{ml} c_{jl} = E_j \sum_{l=1}^{n} S_{ml} c_{jl}, \tag{2.11}$$

The energy bands may be determined using

$$\det(\hat{H} - E_j S) = 0. \tag{2.12}$$

2.3 Tight–binding model for graphene

For graphene, which has two sublattices, for a general wave function $\psi_j = (c_{j1} \quad c_{j2})^T$, then

$$\hat{H} = \begin{pmatrix} H_{AA} & H_{AB} \\ H_{BA} & H_{BB} \end{pmatrix}, \quad S = \begin{pmatrix} S_{AA} & S_{AB} \\ S_{BA} & S_{BB} \end{pmatrix}. \tag{2.13}$$

To determine the transfer integral matrix and overlap matrix, we replace index $j = 1$ for the A sublattice and $j = 2$ for the B sublattice. Substitution of the Bloch wave function (Eq. 2.5) in Eq. 2.9 results in:

$$H_{AA} = \frac{1}{N} \sum_{i=1}^{N} \sum_{j=1}^{N} e^{i\mathbf{k}\cdot(\mathbf{R}_{A,j} - \mathbf{R}_{A,i})} \left\langle \phi_A(\mathbf{r} - \mathbf{R}_{A,i}) \mid H \mid \phi_A(\mathbf{r} - \mathbf{R}_{A,i}) \right\rangle, \tag{2.14}$$

where $\mathbf{k} = (k_x, k_y)$ is the wave vector in the graphene plane. Eq. 2.14 includes a double summation over all A sites of the lattice. If we assume that the dominant contribution arises from the same site $j = i$ within every unit cell, then

$$H_{AA} \approx \frac{1}{N} \sum_{i=1}^{N} \left\langle \phi_A(\mathbf{r} - \mathbf{R}_{A,i}) \mid H \mid \phi_A(\mathbf{r} - \mathbf{R}_{A,i}) \right\rangle. \tag{2.15}$$

The matrix element $\langle \phi_A \mid H \mid \phi_A \rangle$ within the summation has the same value on every A site, i.e. it is independent of the site index i. We set it to be equal to a parameter

$$\epsilon_{2p} = \left\langle \phi_A(\mathbf{r} - \mathbf{R}_{A,i}) \mid H \mid \phi_A(\mathbf{r} - \mathbf{R}_{A,i}) \right\rangle, \tag{2.16}$$

that is equal to the energy of the $2p_z$ orbital. Then, we keep the same site contribution

$$H_{AA} \approx \frac{1}{N} \sum_{i=1}^{N} \epsilon_{2p} = \epsilon_{2p}. \tag{2.17}$$

It is possible to take into account the contribution of other terms in the double summation (Eq. 2.14), such as next–nearest neighbour contributions. They generally have a small effect on the electronic band structure and will not be discussed here. The B sublattice has the same structure as the A sublattice, and the car-

bon atoms on the two sublattices are chemically identical. This means that the diagonal transfer integral matrix element corresponding to the B sublattice has the same values as that of the A sublattice

$$H_{BB} = H_{AA} \approx \epsilon_{2p}. \tag{2.18}$$

A calculation of the diagonal elements of the overlap integral matrix proceeds in a similar way as for those of the transfer integral. In this case, the overlap between a $2p_z$ orbital on the same atom is equal:

$$\langle \phi_A(\mathbf{r} - \mathbf{R}_{A,i}) \mid \phi_A(\mathbf{r} - \mathbf{R}_{A,i}) \rangle = 1. \tag{2.19}$$

Then, assuming that the same site contribution dominates,

$$\begin{aligned} S_{AA} &= \frac{1}{N} \sum_{i=1}^{N} \sum_{j=1}^{N} e^{i\mathbf{k}\cdot(\mathbf{R}_{A,j} - \mathbf{R}_{A,i})} \langle \phi_A(\mathbf{r} - \mathbf{R}_{A,i}) \mid \phi_A(\mathbf{r} - \mathbf{R}_{A,j}) \rangle , \\ &\approx \frac{1}{N} \sum_{i=1}^{N} \langle \phi_A(\mathbf{r} - \mathbf{R}_{A,i}) \mid \phi_A(\mathbf{r} - \mathbf{R}_{A,i}) \rangle , \\ &= \frac{1}{N} \sum_{i=1}^{N} 1, \\ &= 1. \end{aligned} \tag{2.20}$$

Again, as the B sublattice has the same structure as the A sublattice,

$$S_{BB} = S_{AA} = 1. \tag{2.21}$$

For the off–diagonal matrix elements, substitution of Eq. 2.5 into the transfer integral Eq. 2.9 results in

$$\begin{aligned} H_{AB} &\approx \frac{1}{N} \sum_{i=1}^{N} \sum_{l=1}^{3} e^{i\mathbf{k}\cdot(\mathbf{R}_{B,l} - \mathbf{R}_{A,i})} \langle \phi_A(\mathbf{r} - \mathbf{R}_{A,i}) \mid H \mid \phi_B(\mathbf{r} - \mathbf{R}_{B,l}) \rangle , \\ &\simeq -\frac{1}{N} \sum_{i=1}^{N} \sum_{j=1}^{3} e^{i\mathbf{k}\cdot(\mathbf{R}_{B,j} - \mathbf{R}_{A,i})} \gamma_0, \end{aligned}$$

$$= -\gamma_0 f(\mathbf{k}), \tag{2.22}$$

where $f(\mathbf{k}) = \sum_{j=1}^{3} e^{i\mathbf{k}\cdot\delta_j}$ (Fig. 2.1). Eq. 2.22 describes the hopping between different nearest neighbour sublattices. The matrix element between neighbouring atoms, $\langle \phi_A \mid H \mid \phi_B \rangle$, has the same value for each neighbouring pair, i.e. it is in dependent of indices i and l. Here, we have defined parameter γ_0, so that

$$\gamma_0 = -\left\langle \phi_A(\mathbf{r} - \mathbf{R}_{A,i}) \mid H \mid \phi_B(\mathbf{r} - \mathbf{R}_{B,l}) \right\rangle . \tag{2.23}$$

Here, δ_l is the position vector of atom B_l relative to the A_i atom, $\delta_l = \mathbf{R}_{B,l} - \mathbf{R}_{A,i}$. According to Fig. 2.1, we can show that

$$\delta_1 = \left(0, \frac{a}{\sqrt{3}}\right), \quad \delta_2 = \left(\frac{a}{2}, -\frac{a}{2\sqrt{3}}\right), \quad \delta_3 = \left(-\frac{a}{2}, -\frac{a}{2\sqrt{3}}\right). \tag{2.24}$$

The overlap integral matrix is

$$\begin{aligned} S_{AB} \quad &= \frac{1}{N} \sum_{i=1}^{N} \sum_{j=1}^{N} e^{i\mathbf{k}\cdot(\mathbf{R}_{B,j} - \mathbf{R}_{A,i})} \left\langle \phi_A(\mathbf{r} - \mathbf{R}_{A,i}) \mid \phi_B(\mathbf{r} - \mathbf{R}_{B,j}) \right\rangle , \\ &\simeq \frac{1}{N} \sum_{i=1}^{N} \sum_{j=1}^{3} e^{i\mathbf{k}\cdot(\mathbf{R}_{B,j} - \mathbf{R}_{A,i})} s_0, \\ &= s_0 f(\mathbf{k}), \end{aligned} \tag{2.25}$$

where $f(\mathbf{k}) = \sum_{l=1}^{3} e^{i\mathbf{k}\cdot\delta_l}$ and $\langle \phi_A(\mathbf{r} - \mathbf{R}_{A,i}) \mid \phi_B(\mathbf{r} - \mathbf{R}_{B,j}) \rangle = s_0$. Therefore, the tight–binding Hamiltonian and overlap matrices of bilayer graphene are

$$\hat{H} = \begin{pmatrix} \epsilon_{2p} & -\gamma_0 f(\mathbf{k}) \\ -\gamma_0 f^*(\mathbf{k}) & \epsilon_{2p} \end{pmatrix}, \quad S = \begin{pmatrix} 1 & s_0 f(\mathbf{k}) \\ s_0 f^*(\mathbf{k}) & 1 \end{pmatrix}. \tag{2.26}$$

For δ_l determined in Eq. 2.24, $f(\mathbf{k})$ is

$$\begin{aligned} f(\mathbf{k}) \quad &= \sum_{l=1}^{3} e^{i\mathbf{k}\cdot\delta_l}, \\ &= e^{ik_y a/\sqrt{3}} + e^{ik_x a/2} e^{-ik_y a/2\sqrt{3}} + e^{-ik_x a/2} e^{-ik_y a/2\sqrt{3}}, \end{aligned}$$

$$= e^{ik_y a/\sqrt{3}} + 2e^{-ik_y a/2\sqrt{3}} \cos(k_x a/2). \tag{2.27}$$

The interaction between two different sublattices is described by off-diagonal elements of H matrix, H_{AB} (Eq. 2.22), that is proportional to parameter γ_0 and the function $f(\mathbf{k})$ (Eq. 2.27).

Based on Eq. 2.12, the eigenvalues of monolayer graphene are determined by the following determinant:

$$\det \begin{pmatrix} \epsilon_{2p} - E & -(\gamma_0 + Es_0)f(\mathbf{k}) \\ -(\gamma_0 + Es_0)f^*(\mathbf{k}) & \epsilon_{2p} - E \end{pmatrix} = 0, \tag{2.28}$$

$$\Rightarrow (E - \epsilon_{2p})^2 - ([E - \epsilon_{2p}]s_0 + \epsilon_{2p}s_0 + \gamma_0)^2 \left|f(\mathbf{k})\right|^2 = 0, \tag{2.29}$$

$$\Rightarrow E_\pm = \frac{\epsilon_{2p} \pm \gamma_0 \left|f(\mathbf{k})\right|}{1 \mp s_0 \left|f(\mathbf{k})\right|}. \tag{2.30}$$

where $\epsilon_{2p} = 0$ while $\gamma_0 = 3.033$ eV, $s_0 = 0.129$ [34]. However, in the whole of this thesis, the overlap matrix has been considered equal to the unit matrix because, at low–energy, s_0 only appears in quadratic–in–momentum terms and is, thus, irrelevant.

Exactly at the K_ξ point (corners of the BZ), $\mathbf{k} = \mathbf{K}_\xi$, we find that

$$f(\mathbf{K}_\xi) = e^0 + e^{i\xi 2\pi/3} + e^{-i\xi 2\pi/3} = 0. \tag{2.31}$$

This indicates that there is no coupling between A and B sublattices exactly at the K_ξ points. Since the two sublattices are both hexagonal Bravais lattices of carbon atoms, they support the same quantum states leading to a degeneracy point in the spectrum at K_ξ (Fig. 2.3). According to Fig. 2.3, the band structure of monolayer graphene is gapless and, near to the corner of the Brillouin zone, it is linear. The exact cancellation of the three factors describing coupling between the A and B sublattices, Eq. 2.31, no longer holds when the wave vector is not exactly equal to that of the K_ξ point. We introduce a momentum $\mathbf{p}$ that is measured from the

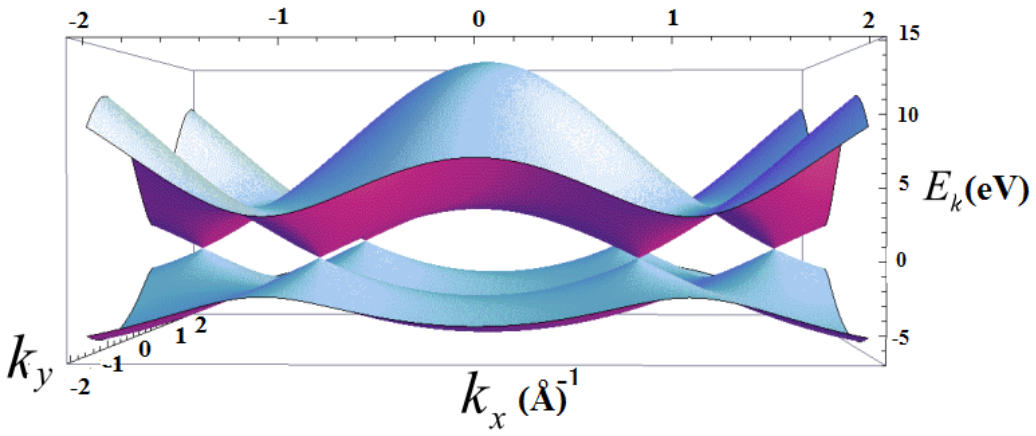

Figure 2.3: The band structure of monolayer graphene in the Brillouin zone. Accordingly, near to the corner of the Brillouin zone, near to the Dirac points, the band structure of monolayer graphene is linear.

centre of the K_ξ point,

$$\mathbf{p} = \hbar\mathbf{k} - \hbar\mathbf{K}_\xi. \tag{2.32}$$

Then, the coupling between A and B sublattices is proportional to

$$f(\mathbf{k}) = e^{ip_y a/\sqrt{3}\hbar} + 2e^{-ip_y a/\sqrt{3}\hbar}\cos\left(\frac{2\pi\xi}{3} + \frac{p_x a}{2\hbar}\right), \tag{2.33}$$

$$\approx \left(1 + \frac{ip_y a}{\sqrt{3}\hbar}\right) + 2\left(1 - \frac{ip_y a}{2\sqrt{3}\hbar}\right)\left(-\frac{1}{2} - \frac{\xi\sqrt{3}p_x a}{4\hbar}\right), \tag{2.34}$$

$$\approx -\frac{\sqrt{3}a}{2\hbar}\left(\xi p_x - ip_y\right). \tag{2.35}$$

To derive this equation, linear terms in momentum, $\mathbf{p} = (p_x, p_y)$, have been considered which is valid for $pa/\hbar \ll 1$. These approximations for $f(\mathbf{k})$ result in an effective Hamiltonian in the vicinity of the K_ξ point:

$$H = v\begin{pmatrix} 0 & \xi p_x - ip_y \\ \xi p_x + ip_y & 0 \end{pmatrix}, \tag{2.36}$$

where $v = \sqrt{3}a\gamma_0/2\hbar$. Eigenvalues and eigenstates of this Hamiltonian dependent

on the valley index are

$$E_{\pm} = \pm vp, \quad \psi_{\pm} = \frac{1}{\sqrt{2}} \begin{pmatrix} 1 \\ \pm\xi e^{i\xi\phi} \end{pmatrix}. \tag{2.37}$$

The eigenstates of graphene based Hamiltonians (Eq. 2.37) have two components: one component refers to A sites, and another one refers to B sites. This is similar to what happens in the description of spin up and spin down electrons, but it is dependent on different sublattices (pseudospin) instead of spin. If all of the electrons were to be on A sites, graphene would have up pseudospin. Or, if all of the electrons were to be on B sites, graphene would have down pseudospin. However, electron density is shared equally between A and B sublattices and the pseudospin vector is in the plane of graphene.

Based on the eigenstates of monolayer graphene, Eq. 2.37, the direction of the pseudospin is dependent on ϕ, momentum direction in space. We calculate the expectation value of the pseudospin operator $\langle\sigma\rangle = (\langle\sigma_x\rangle, \langle\sigma_y\rangle, \langle\sigma_z\rangle)$ with respect to the eigenstate $\psi_{\pm}$, the result is $\langle\sigma\rangle_{e/h} = \pm(\xi\cos\phi, \sin\phi, 0)$. In this situation we say that monolayer graphene electrons are chiral. This means that the direction of pseudospin (in the graphene plane) depends on the direction of electronic momentum.

2.4 Tight–binding model for bilayer graphene

The unit cell of AB–stacked bilayer graphene is depicted in Fig. 2.4. There are four atoms in the unit cell, two dimer sites which are on top of each other and two non–dimer–sites. The primitive lattice and the lattice constant a are the same as for monolayer graphene. The unit cell has the same area in the plane as in the monolayer. Therefore, the reciprocal lattice and first Brillouin zone are the same as in monolayer graphene [13]. In addition, there are four energy bands in its band structure (Fig. 2.5).

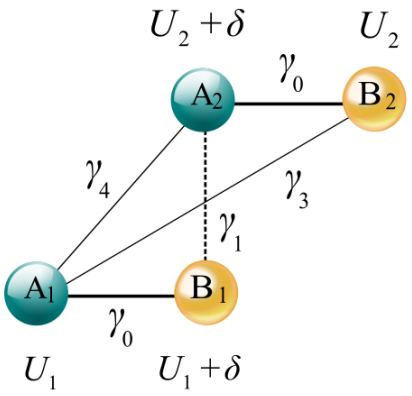

Figure 2.4: The side view of 4 atoms in the unit cell of AB stacked bilayer graphene. A_1 and B_1 atoms on the top layer and A_2 and B_2 on the bottom layer have been depicted. Straight lines indicate intralayer coupling γ_0, vertical interlayer coupling γ_1 and skew interlayer couplings γ_3, γ_4. Parameters U_1, U_2, δ indicate different on-site energies, as described in the main text.

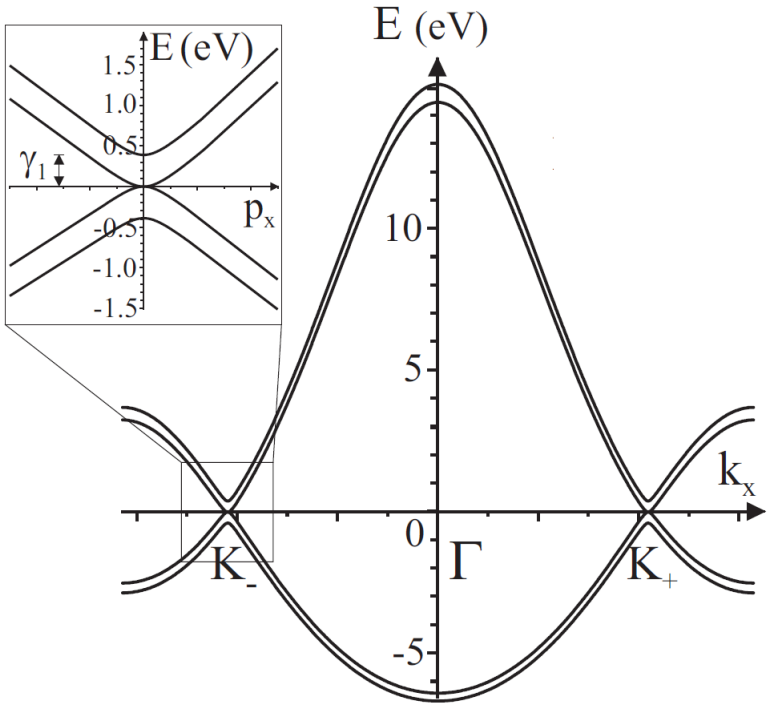

Figure 2.5: The band structure of bilayer graphene considering nearest neigbor hopping parameters where $\gamma_0 = 3.033eV$, $\epsilon_{2p} = 0$, $\gamma_1 = 0.39eV$ and $s_0 = 0.129$. Figure taken from E McCann, Graphene Nanoelectronics, Berlin Heidelberg : Springer, 237 (2012).

Because there are four atoms in the unit cell, the Hamiltonian is 4×4 as well. In the tight–binding description of bilayer graphene in a basis of $(A_1, B_1, A_2, B_2)^\dagger$

the Hamiltonian is [20]

$$\begin{pmatrix} U_1 & -\gamma_0 f(\mathbf{k}) & \gamma_4 f(\mathbf{k}) & -\gamma_3 f^*(\mathbf{k}) \\ -\gamma_0 f^*(\mathbf{k}) & U_1+\delta & \gamma_1 & \gamma_4 f(\mathbf{k}) \\ \gamma_4 f^*(\mathbf{k}) & \gamma_1 & U_2+\delta & -\gamma_0 f(\mathbf{k}) \\ -\gamma_3 f(\mathbf{k}) & \gamma_4 f^*(\mathbf{k}) & -\gamma_0 f^*(\mathbf{k}) & U_2 \end{pmatrix}, \tag{2.38}$$

Consequently, the Hamiltonian near the K_ξ point is

$$H = \begin{pmatrix} U_1 & v\pi^\dagger & -v_4\pi^\dagger & v_3\pi \\ v\pi & U_1+\delta & \gamma_1 & -v_4\pi^\dagger \\ -v_4\pi & \gamma_1 & U_2+\delta & v\pi^\dagger \\ v_3\pi^\dagger & -v_4\pi & v\pi & U_2 \end{pmatrix}. \tag{2.39}$$

Here, with a being the lattice constant and γ_i being tight–binding hopping parameter, $v_i = \sqrt{3}a\gamma_i/2\hbar$ are velocities corresponding to three different hopping factors in bilayer graphene, $i = 0, 1, 3, 4$, $v_0 = v$. This Hamiltonian has been written based on the next–nearest approximation in the tight–binding model.

Parameter v characterizes the strength of in–plane nearest–neighbour $\mathbf{A}_1 - \mathbf{B}_1$ and $\mathbf{A}_2 - \mathbf{B}_2$ hopping, γ_1 describes vertical interlayer coupling, v_3 characterizes the strength of skew interlayer $\mathbf{A}_1 - \mathbf{B}_2$ hopping and v_4 characterizes the strength of skew interlayer $\mathbf{A}_1 - \mathbf{A}_2$, $\mathbf{B}_1 - \mathbf{B}_2$ hoppping. Parameters U_1, U_2 are the on–site energies of the two layers and δ describes an energy difference between sites which have neighbouring atoms directly above or below them (dimer sites) and those sites which do not [39; 20]. Numerical values of these tight binding hopping parameters are $\gamma_0 = 3.0$ eV, $\gamma_1 = 0.4$ eV, $\gamma_3 = 0.38$ eV, $\gamma_4 = 0.015$ eV [28].

2.5 Two component Hamiltonian

The Fermi level is generally located near zero energy where only two bands are present. Thus, we study the low–energy Hamiltonian of bilayer graphene which is

a 2×2 matrix related to the non–dimer sites [13; 19]. This two component model is valid at low energy where $\epsilon \ll \gamma_1$. The basis of this Hamiltonian is $(A_1, B_2)^\dagger$.

To derive a two component Hamiltonian, we divide the 4×4 Hamiltonian into four blocks [20]. We also divide the eigenstate of the Hamiltonian into low–energy, $\psi_l = (\psi_{A_1}, \psi_{B_2})^T$, and dimer, $\psi_d = (\psi_{A_2}, \psi_{B_1})^T$, components. Consequently, we can write

$$\begin{pmatrix} h_{\psi_l} & x \\ x^\dagger & h_{\psi_d} \end{pmatrix} \begin{pmatrix} \psi_l \\ \psi_d \end{pmatrix} = E \begin{pmatrix} \psi_l \\ \psi_d \end{pmatrix}. \tag{2.40}$$

The second row of Eq. 2.40 allows the dimer components to be expressed in terms of the low–energy ones

$$\psi_d = (E - h_{\psi_d})^{-1} x^\dagger \psi_l. \tag{2.41}$$

Substituting this into the first row of Eq. 2.40 gives an effective eigenvalue equation which is only for the low–energy components

$$\left[h_{\psi_l} + x(E - h_{\psi_d})^{-1} x^\dagger\right] \psi_l = E\psi_l, \tag{2.42}$$

$$\left[h_{\psi_l} - x h_{\psi_d}^{-1} x^\dagger\right] \psi_l = ES\psi_l, \tag{2.43}$$

where $S = 1 + x h_{\psi_d}^{-2} x^\dagger$, and the second equation is accurate up to linear terms in energy. Then, we perform a transformation $\Phi = S^{1/2}\psi_l$

$$\left[h_{\psi_l} - x h_{\psi_d}^{-1} x^\dagger\right] S^{-1/2}\Phi \approx ES^{-1/2}\Phi, \tag{2.44}$$

$$S^{-1/2}\left[h_{\psi_l} - x h_{\psi_d}^{-1} x^\dagger\right] S^{-1/2}\Phi \approx E\Phi. \tag{2.45}$$

This transformation ensures that the normalization of Φ is consistent with that of

the original states

$$\begin{aligned}\Phi^\dagger\Phi &= \psi_l^\dagger S\psi_l = \psi_l^\dagger(1+xh_{\psi_d}^{-2}x^\dagger)\psi_l,\\ &\approx \psi_l^\dagger\psi_l + \psi_d^\dagger\psi_d,\end{aligned} \tag{2.46}$$

where we used equation Eq. 2.41 for small E, $\psi_d = -h_{\psi_d}^{-1}x^\dagger\psi_l$. Thus, the effective Hamiltonian at low energy is given by Eq. 2.45

$$H^{(eff)} \approx S^{-1/2}\left[h_{\psi_l} - xh_{\psi_d}^{-1}x^\dagger\right]S^{-1/2}, \tag{2.47}$$

$$S = 1 + xh_{\psi_d}^{-2}x^\dagger. \tag{2.48}$$

We apply these general equations to bilayer graphene (Eq. 2.39) giving the following 2×2 blocks:

$$x = \begin{pmatrix} -v_4\pi^\dagger & v_3\pi \\ v\pi & U_2 \end{pmatrix}, \tag{2.49}$$

$$h_{\psi_l} = \begin{pmatrix} U_1 & v\pi^\dagger \\ v_3\pi^\dagger & -v_4\pi \end{pmatrix}, \tag{2.50}$$

$$h_{\psi_d} = \begin{pmatrix} U_2+\delta & v\pi^\dagger \\ \gamma_1 & -v_4\pi^\dagger \end{pmatrix}. \tag{2.51}$$

Then, using Eqs. 2.47 and 2.48, the 2×2 Hamiltonian of bilayer graphene is

$$
\begin{aligned}
H \quad &= -\frac{v^2}{\gamma_1}\left[1+\left(\frac{v_4}{v}+\frac{\delta}{\gamma_1}\right)^2-\frac{(U_1^2+U_2^2)}{2\gamma_1^2}\right]\begin{pmatrix} 0 & \pi^{\dagger 2} \\ \pi^2 & 0 \end{pmatrix} \\
&+\begin{pmatrix} U_1 & 0 \\ 0 & U_2 \end{pmatrix} \\
&+v_3\begin{pmatrix} 0 & \pi \\ \pi^\dagger & 0 \end{pmatrix} \\
&-\frac{v^2p^2}{\gamma_1^2}\begin{pmatrix} U_1-U_2-\delta & 0 \\ 0 & U_2-U_1-\delta \end{pmatrix} \\
&+\frac{2vv_4p^2}{\gamma_1}\begin{pmatrix} 1 & 0 \\ 0 & 1 \end{pmatrix}. \qquad (2.52)
\end{aligned}
$$

The first term in Eq. 2.52 describes chiral quasiparticles in bilayer graphene with the direction of pseudospin in (A_1, B_2) space lying in the graphene plane and related to that of the electronic momentum, and this term accounts for a quadratic dispersion $\epsilon \approx v^2p^2/\gamma_1$. In the following, we assume the other terms are a small perturbation with respect to this dominant one. The second term describes different on–site energies U_1, U_2 on the A_1 and B_2 sites, and the third term accounts for trigonal warping due to the presence of skew interlayer coupling γ_3 between the A_1 and B_2 sites.

For this quadratic Hamiltonian, the quadratic dispersion relation is $E_s = sp^2/2m$, where s is $+1(-1)$ for the conduction (valence) band and m, mass, is equal to $\gamma_1/2v$. The eigenstate of the essential part of the above Hamiltonian is

$$
\psi_s = \frac{1}{\sqrt{2}L}\begin{pmatrix} 1 \\ -se^{2i\xi\phi} \end{pmatrix} e^{i\mathbf{p}\cdot\mathbf{r}/\hbar}. \qquad (2.53)
$$

For the main term, the probability of the existence of electrons on A or B sites is the same. While for monolayer graphene the phase difference between electron

wave functions of A and B sublattices is $i\xi\phi$, for bilayer graphene, this phase shift is $2i\xi\phi$ (Eq. 2.53)[13]. The phase difference between A and B sublattices is dependent on the momentum direction in the space, meaning that bilayer graphene electrons are chiral.

The main term of the bilayer graphene Hamiltonian determines the main pseudospin and the graphene chirality. According to pseudospin vector definition , $\sigma = (\sigma_x, \sigma_y, \sigma_z)$, as we saw the expectation values of this operator for monolayer and bilayer graphene are $\langle\sigma\rangle_{e/h} = \pm(\xi\cos\phi, \sin\phi, 0)$ and $\langle\sigma\rangle_{e/h} = \mp(\cos 2\phi, \xi\sin 2\phi, 0)$, respectively [15]. Consequently, in monolayer graphene, if the momentum turns 2π degree, the pseudospin vector, dependent on the valley, turns parallel or anti–parallel to the momentum 2π degree. For bilayer graphene, the pseudospin vector turns twice as fast as that of monolayer graphene.

The second term of the Hamiltonian, the second line of Eq. 2.52, is related to the broken symmetry between non–dimer sites caused by applying a gate voltage. This term opens a gap in the bilayer graphene band structure [40]. The third term is the trigonal warping term which resembles the linear–in–momentum Hamiltonian of monolayer graphene [13]. However, while the linear term for monolayer graphene is the main term, the linear term here leads to a Lifshitz transition for bilayer graphene.

To summarize, we have studied theoretical background and tight–binding model of monolayer and bilayer graphene in this Chapter. To reach this aim, we have discussed about unit cell and primitive vectors of monolayer and bilayer graphene in the direct and in the reciprocal lattice. We have also defined atomic labels, layer index and on–site energies for bilayer graphene. In addition, general tight–binding model has been described based on tight–binding parameters and it has been used to derive monolayer graphene Hamiltonian. Moreover, tight binding model has been used to extract bilayer graphene Hamiltonian. Then, based on the method introduced in Ref. [20], low–energy Hamiltonian of bilayer graphene has been extracted.

Chapter 3

The Hamiltonian of bilayer graphene in the presence of an in–plane magnetic field

3.1 Four component Hamiltonian of bilayer graphene

In this Chapter, we have used orbital effect to write the Hamiltonian of bilayer graphene in a parallel magnetic field. For simplicity, we neglect Zeeman effect of the conduction band and focus on the orbital mechanisms [41]. Zeeman effect is the splitting of a band into two components in the presence of a static magnetic field. For graphene in a constant magnetic field Zeeman energy is $E = g\mu_B B$ where for μ_B as Bohr Magneton, $g \approx 2$, Zeeman energy is $\pm 11.56 \times 10^{-5}$ eV per Tesla [42]. Hence, experimentally determined Zeeman effect is of order of 10 μeV, while orbital effect is of order of meV. As a consequence, the Zeeman effect is neglected.

To derive the bilayer graphene tight–binding Hamiltonian in the parallel magnetic field, the Peierls substitution is used. The Peierls substitution method is an approximation for describing tightly-bound electrons in the presence of a slowly varying magnetic vector potential [43]. For instance, to determine the Hamiltonian

element for a process of hopping between the in–plane A and B sublattices, H_{AB}, we must evaluate the following summation over B sites at the position $\mathbf{R}_{B_j}$

$$H_{AB} = -\gamma_0 \sum_{j=1}^{3} \exp\left(i\mathbf{k}\cdot(\mathbf{R}_{B_j} - \mathbf{R}_A) - \frac{ie}{\hbar}\int_{R_{B_j}}^{R_A} \mathbf{A}.d\mathbf{l} \right). \tag{3.1}$$

Here, $\mathbf{k}$ is the electron wave vector, $d\mathbf{l}$ is the length differential, and $\mathbf{A}$ is the magnetic field vector potential and it is equal to $(zB_y, -zB_x)$ where the magnetic field is $\mathbf{B} = (B_x, B_y, 0)$. We assume the lower layer of the bilayer is located at $z = -d/2$, the upper layer at $z = +d/2$, where d is the interlayer spacing. For example, to calculate $H_{A_1B_1}$ we have

$$H_{A_1B_1} = -\gamma_0 \sum_{j=1}^{3} \exp\left(i\mathbf{k}\cdot(\mathbf{R}_{Bj} - \mathbf{R}_A) - \frac{ie}{\hbar}\int_{\mathbf{R}_{Bj}}^{\mathbf{R}_A} \mathbf{A}\cdot dl \right). \tag{3.2}$$

We have introduced the first nearest neighbour coordinate in the first chapter. Consequently, we can write

$$\begin{aligned} H_{A_1B_1} \quad &= -\gamma_0 \Bigg\{ \exp\left(i\mathbf{k}\cdot(-\delta_1) - \frac{ie}{\hbar}\int_{\mathbf{R}_{B11}}^{\mathbf{R}_A} (zB_y, -zB_x)\cdot dl \right) \\ &+ \exp\left(i\mathbf{k}\cdot(-\delta_2) - \frac{ie}{\hbar}\int_{\mathbf{R}_{B12}}^{\mathbf{R}_A} (zB_y, -zB_x)\cdot dl \right) \\ &+ \exp\left(i\mathbf{k}\cdot(-\delta_3) - \frac{ie}{\hbar}\int_{\mathbf{R}_{B13}}^{\mathbf{R}_A} (zB_y, -zB_x)\cdot dl \right) \Bigg\}. \end{aligned} \tag{3.3}$$

By the substitution of the variables we have

$$\begin{aligned} H_{A_1B_1} \quad &= -\gamma_0 \left\{ \exp\left(-ik_y\frac{a}{\sqrt{3}} - \frac{ied}{2\hbar}\int_{(0,\frac{a}{\sqrt{3}},\frac{d}{2})}^{(0,0,\frac{d}{2})} B_y dx - B_x dy \right) \right. \\ &+ \exp\left(-ik_x\frac{a}{2} + ik_y\frac{a}{2\sqrt{3}} - \frac{ied}{2\hbar}\int_{(\frac{a}{2},\frac{-a}{2\sqrt{3}},\frac{d}{2})}^{(0,0,\frac{d}{2})} B_y dx - B_x dy \right) \\ &+ \left. \exp\left(ik_x\frac{a}{2} + ik_y\frac{a}{2\sqrt{3}} - \frac{ied}{2\hbar}\int_{(\frac{-a}{2},\frac{-a}{2\sqrt{3}},\frac{d}{2})}^{(0,0,\frac{d}{2})} B_y dx - B_x dy \right) \right\}. \end{aligned} \tag{3.4}$$

So, we have

$$\begin{aligned} H_{A_1B_1} \quad &= -\gamma_0 \left\{ \exp\left(-ik_y \frac{a}{\sqrt{3}} - \frac{ied}{2\hbar}\frac{a}{\sqrt{3}} B_x\right) \right. \\ &+ \exp\left(i\left(\frac{-k_x a}{2} + \frac{k_y a}{2\sqrt{3}}\right) - \frac{ied}{2\hbar}\left(-B_y\frac{a}{2} - B_x\frac{a}{2\sqrt{3}}\right)\right) \\ &\left. + \exp\left(i\left(\frac{k_x a}{2} + \frac{k_y a}{2\sqrt{3}}\right) - \frac{ied}{2\hbar}\left(B_y\frac{a}{2} - B_x\frac{a}{2\sqrt{3}}\right)\right) \right\}. \end{aligned} \tag{3.5}$$

This equation is similar to Eq. 2.27 and 2.33 with the difference that p_x changes to $p_x - b_y$ and p_y changes to $p_y + b_x$, where $\mathbf{b} = ed\mathbf{B}/2$. Consequently, $H_{A_1B_1} = v\left(\xi(p_x - b_y) + i(p_y + b_x)\right)$. Also, $H_{B_1A_1} = (H_{A_1B_1})^*$.

As a result, we can show that the 4×4 Hamiltonian of bilayer graphene in the parallel magnetic field is

$$H = \begin{pmatrix} U_1 & v\pi_1^\dagger & -v_4\pi^\dagger & v_3\pi \\ v\pi_1 & U_1 + \delta & \gamma_1 & -v_4\pi^\dagger \\ -v_4\pi & \gamma_1 & U_2 + \delta & v\pi_2^\dagger \\ v_3\pi^\dagger & -v_4\pi & v\pi_2 & U_2 \end{pmatrix}. \tag{3.6}$$

For in–plane momentum $\mathbf{p} = (p_x, p_y, 0)$, the complex momentum operators are $\pi_1 = \pi - \xi b_y + ib_x$ for the lower layer, $\pi_2 = \pi + \xi b_y - ib_x$ for the upper layer, and $\pi = \xi p_x + ip_y$ for skew interlayer hopping. Here $b_x = edB_x/2$, $b_y = edB_y/2$, and $\xi = \pm 1$ is an index for the two non–equivalent valleys at wave vectors $\xi(4\pi/3a, 0)$.

Following the procedure described in Sec. 2.5, the low–energy Hamiltonian of bilayer graphene in a parallel magnetic field in basis $\left(A_1^{k\pm}, B_2^{k\pm}\right)$ is

$$\begin{aligned} H \quad &= -\frac{v^2}{\gamma_1}\left[1 + \left(\frac{v_4}{v} + \frac{\delta}{\gamma_1}\right)^2 - \frac{(U_1^2 + U_2^2)}{2\gamma_1^2}\right] \begin{pmatrix} 0 & \pi^{\dagger 2} \\ \pi^2 & 0 \end{pmatrix} \\ &+ \begin{pmatrix} U_1 & 0 \\ 0 & U_2 \end{pmatrix} \end{aligned}$$

$$
\begin{aligned}
&+v_3 \begin{pmatrix} 0 & \pi \\ \pi^\dagger & 0 \end{pmatrix} \\
&-\frac{v^2 p^2}{\gamma_1^2} \begin{pmatrix} U_1 - U_2 - \delta & 0 \\ 0 & U_2 - U_1 - \delta \end{pmatrix} \\
&+\frac{2vv_4 p^2}{\gamma_1} \begin{pmatrix} 1 & 0 \\ 0 & 1 \end{pmatrix} \\
&+\frac{2v^2}{\gamma_1^2}(\mathbf{p}\times\mathbf{b})_z \begin{pmatrix} U_1 - U_2 - \delta & 0 \\ 0 & U_1 - U_2 + \delta \end{pmatrix} \\
&-\frac{2vv_4}{\gamma_1}(\mathbf{p}\times\mathbf{b})_z \begin{pmatrix} 1 & 0 \\ 0 & -1 \end{pmatrix} \\
&-\frac{vv_4}{\gamma_1^2}(U_1 - U_2) \begin{pmatrix} 0 & i\pi^\dagger\beta^\dagger \\ -i\pi\beta & 0 \end{pmatrix} \\
&-\frac{v^2}{\gamma_1} \begin{pmatrix} 0 & (\xi b_x - i b_y)^2 \\ (\xi b_x + i b_y)^2 & 0 \end{pmatrix},
\end{aligned}
\tag{3.7}
$$

where $\beta = b_x + i\xi b_y$ and $p = |\mathbf{p}|$. Here, we neglect those terms which are cubic or higher in the magnetic field, cubic or higher in vp/γ_1 and cubic or higher in other small parameters (v_4/v, δ/γ_1, U_1/γ_1 and U_2/γ_1).

Including γ_3 does not produce magnetic field dependent terms in the Hamiltonian, although it will produce small cross terms in the scattering probability. The fourth and fifth terms are not field dependent but those are quadratic in momentum and lead to small corrections to the dispersion. Instead, magnetic field terms appear due to different on–site energies (6th term) or due to the inclusion of skew interlayer coupling γ_4 (7th term) and there is a cross term, too (8th term).

In the following, we neglect terms that are proportional to the unit matrix in (A_1, B_2) space. Although those which have a small effect on the dispersion relation (parameters v_4 and δ both produce electron–hole asymmetry due to the p^2 terms), they do not influence electronic scattering. In addition, we neglect

the small quadratic corrections to the first term in Eq. 3.7 because they do not feature in the results for the scattering rate. Consequently, the Hamiltonian may be simplified as

$$
\begin{aligned}
H \quad &= -\frac{v^2}{\gamma_1}\begin{pmatrix} 0 & \pi^{\dagger 2} \\ \pi^2 & 0 \end{pmatrix} \\
&+\frac{\Delta}{2}\left[1-\frac{2v^2p^2}{\gamma_1^2}\right]\begin{pmatrix} 1 & 0 \\ 0 & -1 \end{pmatrix} \\
&+v_3\begin{pmatrix} 0 & \pi \\ \pi^\dagger & 0 \end{pmatrix} \\
&-\frac{2v^2}{\gamma_1}\left[\frac{v_4}{v}+\frac{\delta}{\gamma_1}\right](\mathbf{p}\times\mathbf{b})_z\begin{pmatrix} 1 & 0 \\ 0 & -1 \end{pmatrix} \\
&-\frac{vv_4\Delta}{\gamma_1^2}\begin{pmatrix} 0 & i\pi^\dagger\beta^\dagger \\ -i\pi\beta & 0 \end{pmatrix} \\
&-\frac{v^2}{\gamma_1}\begin{pmatrix} 0 & (\xi b_x - ib_y)^2 \\ (\xi b_x + ib_y)^2 & 0 \end{pmatrix},
\end{aligned}
\tag{3.8}
$$

where we denote interlayer asymmetry by $\Delta = U_1 - U_2$. In Eq. 3.8, the first line is the main term, because it is related to γ_1 and γ_0, the largest hopping factors [20].

3.2 Symmetry analysis of the Hamiltonian

Here, we check that the Hamiltonian obeys spatial inversion symmetry. To do this, we write the Hamiltonian Eqs. 3.7 in terms of Pauli matrices in the sublattice and

the valley spaces:

$$
\begin{aligned}
H \quad &= -\frac{v^2}{\gamma_1}\left(1+\left(\frac{v_4}{v}+\frac{\delta}{\gamma_1}\right)^2-\frac{U_1^2+U_2^2}{2\gamma_1^2}\right)\left[(p_x^2-p_y^2)(\Pi_0\sigma_x)+2p_xp_y(\Pi_z\sigma_y)\right]\\
&+\left(\frac{U_1+U_2}{2}-\frac{v^2p^2\delta}{\gamma_1^2}+\frac{2v^2\Delta}{\gamma_1^2}(\mathbf{p}\times\mathbf{b})_z+\frac{2vv_4p^2}{\gamma_1}\right)\Pi_0\sigma_0\\
&+\frac{\Delta}{2}\left[1-\frac{2v^2p^2}{\gamma_1^2}\right]\Pi_0\sigma_z\\
&+v_3\left[p_x(\Pi_z\sigma_x)-p_y(\Pi_0\sigma_y)\right]\\
&-\frac{2v^2}{\gamma_1}\left[\frac{v_4}{v}+\frac{\delta}{\gamma_1}\right](\mathbf{p}\times\mathbf{b})_z\Pi_0\sigma_z\\
&+\frac{vv_4\Delta}{\gamma_1^2}\left[(p_yb_x+p_xb_y)(\Pi_0\sigma_x)+(p_yb_y-p_xb_x)(\Pi_z\sigma_y)\right]\\
&-\frac{v^2}{\gamma_1}\left[(b_x^2-b_y^2)(\Pi_0\sigma_x)+2b_xb_y(\Pi_z\sigma_y)\right]. \qquad (3.9)
\end{aligned}
$$

Here, we use a direct product of AB lattice space matrices $\sigma_{x,y,z}$ and pseudospin inter/intra valley matrices $\Pi_{0,x,y,z}$ in order to highlight the different forms of the Hamiltonian in the non–equivalent valleys (σ_i are Pauli matrices acting in the sublattice space, $\Pi_0 \equiv \widehat{1}$ is acting in the valley space) [44]. The Hamiltonian of bilayer graphene should be symmetric under inversion symmetry. The inversion symmetry operator is a $(C_6R_z)^3$ operator which is constructed of 2 generators, $\pi/3$–rotation, C_6 and mirror reflection with respect to OZ axis, R_z. While the v, δ, and γ prefactors are intrinsic parameters of the lattice and are symmetric with respect to the spatial inversion, the momentum and Δ change their sign under spatial inversion. However, the magnetic field does not change under inversion symmetry. Considering following equations

$$
\begin{aligned}
&(C_6R_z)^3U_1=U_2, \qquad (C_6R_z)^3U_2=U_1, \qquad (C_6R_z)^3I=I,\\
&(C_6R_z)^3\Pi_z\sigma_y=\Pi_z\sigma_y, \qquad (C_6R_z)^3\Pi_0\sigma_z=-\Pi_0\sigma_z, \qquad (C_6R_z)^3\Pi_0\sigma_x=\Pi_0\sigma_x,\\
&(C_6R_z)^3\Pi_z\sigma_x=-\Pi_z\sigma_x, \qquad (C_6R_z)^3\Pi_0\sigma_y=-\Pi_0\sigma_y.
\end{aligned}
$$

Consequently, the derived Hamiltonian (Eq. 3.9) is invariant under spatial inversion. It is also possible to show that this Hamiltonian is invariant under time

reversal symmetry. The appearance of the magnetic field in the form of $(\mathbf{p} \times \mathbf{b})_z$ in Eq. 3.9 causes the Hamiltonian to be invariant under time reversal symmetry.

To summarize, we have considered the orbital effect of an in-plane magnetic field on electrons in bilayer graphene. Previously, the orbital effect of an in-plane magnetic field on the electronic spectrum was modeled [45; 46; 47] using the so–called minimal tight–binding model which includes only intralayer and vertical interlayer coupling, accounting for quadratic–in–magnetic field terms in the low–energy Hamiltonian. Here, we derived linear–in–field terms in the Hamiltonian arising from skew interlayer coupling and nonuniform on–site energies. We found two types of term; the first has the form of the Lorentz force, and it causes the pseudospin (the relative amplitude of the wave function on the two layers) to acquire a small component perpendicular to the graphene plane. The second term is off diagonal in the layer space, and it creates a small perturbation of the pseudospin direction within the graphene plane.

Chapter 4

The Lifshitz transition of bilayer graphene in an in–plane magnetic field

4.1 Introduction

As mentioned in the Introduction, a Lifshitz transition occurs at very low energy in bilayer graphene. The presence of the linear–in–momentum term in the Hamiltonian (the third term in Eq. 3.8) arising from skew interlayer coupling γ_3 causes a distortion of the Fermi circle, known as trigonal warping. At very low energy, this warping leads to a breaking of the Fermi surface into four different pockets **??**, Fig. 4.1. In this Chapter, we aim to determine the influence of the in-plane magnetic field on the Lifshitz transition. Interlayer asymmetry, Δ, will be neglected because its effect is already well understood (it opens a gap) [20].

The influence of an in-plane field has been considered previously [48; 45; 46; 47; 49; 50], but simplified tight-binding models were used that neglected small tight-binding parameters such as γ_4 and δ. Thus, they included the quadratic in magnetic field term, but not the linear one, Eq. 3.8. Our aim is to include the linear one, too. To begin, we will estimate the magnitude of the linear term as

compared to the quadratic one,

$$\frac{\text{linear}}{\text{quadratic}} \sim \frac{2\Delta_4 p}{b} = \frac{4\Delta_4 |p|}{ed\,|\mathbf{B}|}, \tag{4.1}$$

where $\Delta_4 = v_4/v + \delta/\gamma_1$. We will estimate the value of this ratio at a magnetic field of 1 Tesla and a momentum value corresponding to the centre of one of the Fermi surface pockets, $p = \gamma_1 v_3/v^2$ [19]. Then, we find that

$$\frac{\text{linear}}{\text{quadratic}} \sim \frac{4\Delta_4 \gamma_1 v_3}{ed\,|B|\,v^2} \sim 28. \tag{4.2}$$

This then shows that the linear term is indeed relevant for the Lifshitz transition, at least for realistic values of magnetic field. In Section 4.2, we begin the analysis of the influence of the field on the Lifshitz transition by considering the quadratic–in–field term only. Then, in Section 4.3, we will include the full model that incorporates the linear–in–field term.

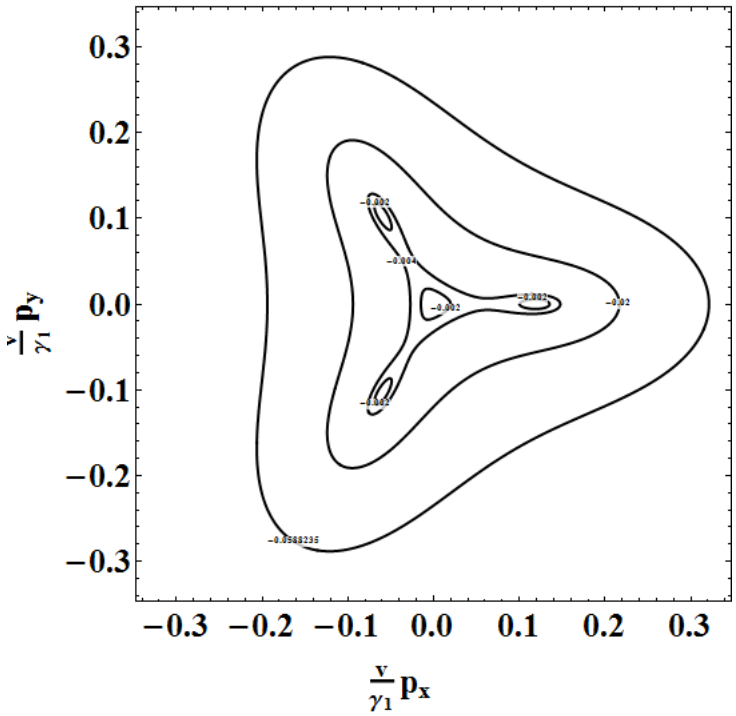

Figure 4.1: Low–energy isoenergetic contours for zero magnetic field. Figure determined with numerical calculations as described in Section 4.2. For k_+ valley the lowest energy conduction band is considered. Constant energy contours in the $(\nu p_x/\gamma_1, \nu p_y/\gamma_1)$ for $\epsilon/\gamma_1 = -0.002$, $\epsilon/\gamma_1 = -0.004$, $\epsilon/\gamma_1 = -0.020$, and $\epsilon/\gamma_1 = -0.059$ at zero magnetic field.

4.2 The effect of in–plane magnetic field on the Lifshitz transition, neglecting small parameters γ_4 and δ

To visualise the Lifshitz transition, we plot constant energy contours, as in Fig. 4.1. To derive such contours, the 4×4 Hamiltonian of bilayer graphene, Eq. 3.6, was used with $U_2 = U_1 = 0$ and $\gamma_4 = \delta = 0$. We introduce dimensionless variables

$$\frac{vp_x}{\gamma_1}, \quad \frac{vp_y}{\gamma_1} \tag{4.3}$$

and multiply the Hamiltonian by $1/\gamma_1$. Then, we choose either conduction or valence bands and depict the isoenergetic contours. The result for non–zero magnetic field is depicted in Fig. 4.2.

Fig. 4.2 shows the effect that a $200T$ in–plane magnetic field in the x direction has on the Lifshitz transition. Comparison of Fig. 4.1 and Fig. 4.2 shows that the in–plane magnetic field affects the Lifshitz transition, albeit at an extremely high field value (note, however, that we only take the quadratic–in–plane field contribution into account at this stage). To determine the possible locations of turning points and Dirac points in the spectrum, it is convenient to use the 2×2 Hamiltonian, Eq. 3.8. Then, we introduce a new set of dimensionless variables $\tilde{p_x}$, $\tilde{p_y}$, $\tilde{\beta}$:

$$\tilde{p_x} = \frac{p_x}{K_b}, \quad \tilde{p_y} = \frac{p_y}{K_b}, \quad \tilde{\beta} = \frac{\beta}{K_b} = \frac{edB}{2K_b}, \tag{4.4}$$

where the typical momentum scale is given by

$$K_b = mv_3. \tag{4.5}$$

We multiply the Hamiltonian by $2m/K_b^2$ to make the Hamiltonian dimensionless, too. Then we calculate the eigenvalues for one valley which are dependent on $\tilde{\beta}$ and the direction of the magnetic field φ. To find saddle points and maxima and

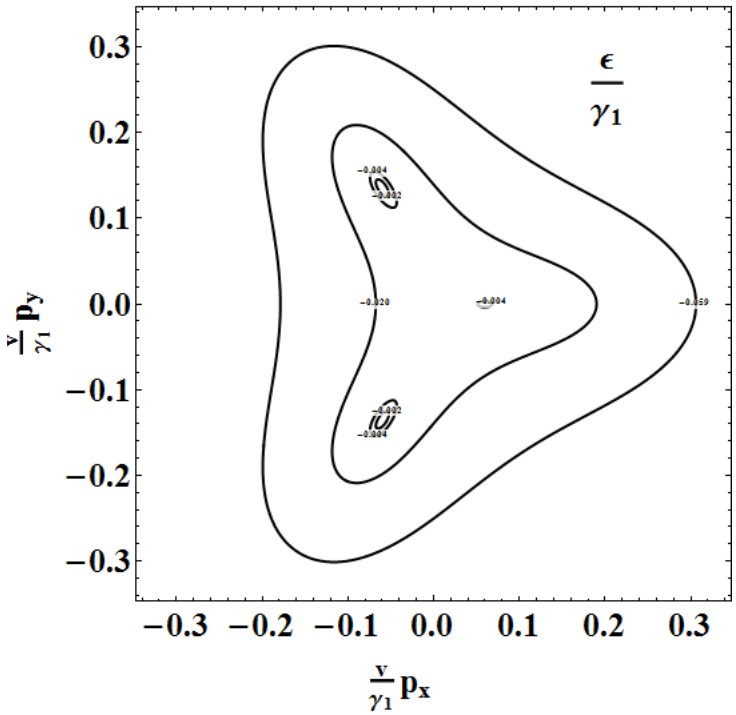

Figure 4.2: Low–energy isoenergetic contour for magnetic field along the x axis. Isoenergetic contours in k_+ valley for the first valence band are depicted, considering $v_4 = 0$ and $\delta = 0$. Constant energy contours in the $(\nu p_x/\gamma_1, \nu p_y/\gamma_1)$ for $\epsilon/\gamma_1 = -0.002$, $\epsilon/\gamma_1 = -0.004$, $\epsilon/\gamma_1 = -0.020$, and $\epsilon/\gamma_1 = -0.059$ kept in a $200T$ magnetic field in x direction. Isoenergetic contours for the conduction band are the same.

minima, first, we calculate the eigenvalue squared. Then, the partial derivative of the eigenvalue squared is determined for $\tilde{p_x}$ and for $\tilde{p_y}$. Then, we find those $(\tilde{p_x}, \tilde{p_y})$ for which the partial derivatives are simultaneously zero. Of these points, Dirac points are where the squared eigenvalue is also equal to zero. Fig. 4.3 shows the resulting contour plots for different magnetic field strengths and orientations. Consequently, we can distinguish three phases shown in Fig. 4.3. If the magnetic field is equal to zero, there are four Dirac Points (DPs) in band structure. In addition, for $0 < \beta < 2$ and the field directed along the x–axis the number of DPs is also four. For $2 < \beta < 5$, there are two DPs and one local minima in the band structure of bilayer graphene. Then, for stronger magnetic field, there are only two Dirac points.

However, these phases are dependent on the orientation of the magnetic field. As depicted in Fig. 4.3, if the magnetic field direction is $\pi/2$, by the increase of magnetic field a phase transition from four DPs to two DPs happens. In addition,

according to this figure, for stronger fields, by $\pi/2$ rotation of the magnetic field, DPs will also rotate in the p–plane as much as $\pi/2$, Fig. 4.3. In order to summarise the different situations shown in the contour plots, Fig. 4.3, we derive a phase diagram as a function of magnetic field. To do this, we use the 2×2 Hamiltonian Eq. 3.8. For $\gamma_3 = 0$, we consider the first and last terms of Eq. 3.8, and ignore all other terms. Then, the low–energy eigenvalue of this Hamiltonian is determined:

$$\epsilon^2 = \frac{p^4}{4m^2} + \frac{\beta^2}{8m^2} p^2 \cos[2(\varphi - \phi)] + \frac{\beta^2}{64m^2}. \tag{4.6}$$

The Dirac points of the spectrum are given by the roots of this equation: it has two roots for $\varphi - \phi = n\pi$, $n = \pm 1$, and $p = \pm\beta/2$.

To determine the phase diagram with $\gamma_3 \neq 0$, according to Fig. 4.3, first we distinguish the range of magnetic field where there are four DPs. The condition is fulfilled when the imaginary part and the real part of one of the off–diagonal terms of the Hamiltonian are equal to zero at the same time, so that for derived dimensionless $(\tilde{p_x}, \tilde{p_y})$ points, $\tilde{\epsilon} = 0$ is also satisfied. In Cartesian coordinates, for a non–zero magnetic field, we have

$$\begin{aligned} \tilde{\epsilon}^2 \quad &= \big(\tilde{p}_x^2 + \tilde{p}_y^2\big)^2 - 4\tilde{p_x}\big(\tilde{p}_x^2 - 3\tilde{p}_y^2\big) + 4\big(\tilde{p}_x^2 + \tilde{p}_y^2\big) \\ &+ \frac{1}{2}\tilde{\beta}_y^2\big(\tilde{p}_y^2 + 2\tilde{p}_x - \tilde{p}_x^2\big) + \frac{1}{8}\tilde{\beta}_x^2\big(- 4\tilde{p}_y^2 + 4\tilde{p}_x^2 - 8\tilde{p}_x + \beta_y^2\big) \\ &+ 2\tilde{\beta}_x\tilde{\beta}_y\big(1 + \tilde{p}_x\big)\tilde{p}_y + \frac{1}{16}\tilde{\beta}_x^4 + \frac{1}{16}\tilde{\beta}_y^4 = 0, \end{aligned} \tag{4.7}$$

The real part of one of the diagonal terms:

$$\tilde{p}_y^2 + \tilde{p}_x^2 + 2\tilde{p}_x + \frac{1}{4}\tilde{\beta}_y^2 - \frac{1}{4}\tilde{\beta}_x^2 = 0. \tag{4.8}$$

The imaginary part of one of the diagonal terms:

$$2\tilde{p}_y + 2\tilde{p}_y\tilde{p}_x + \frac{1}{2}\tilde{\beta}_x\tilde{\beta}_y = 0. \tag{4.9}$$

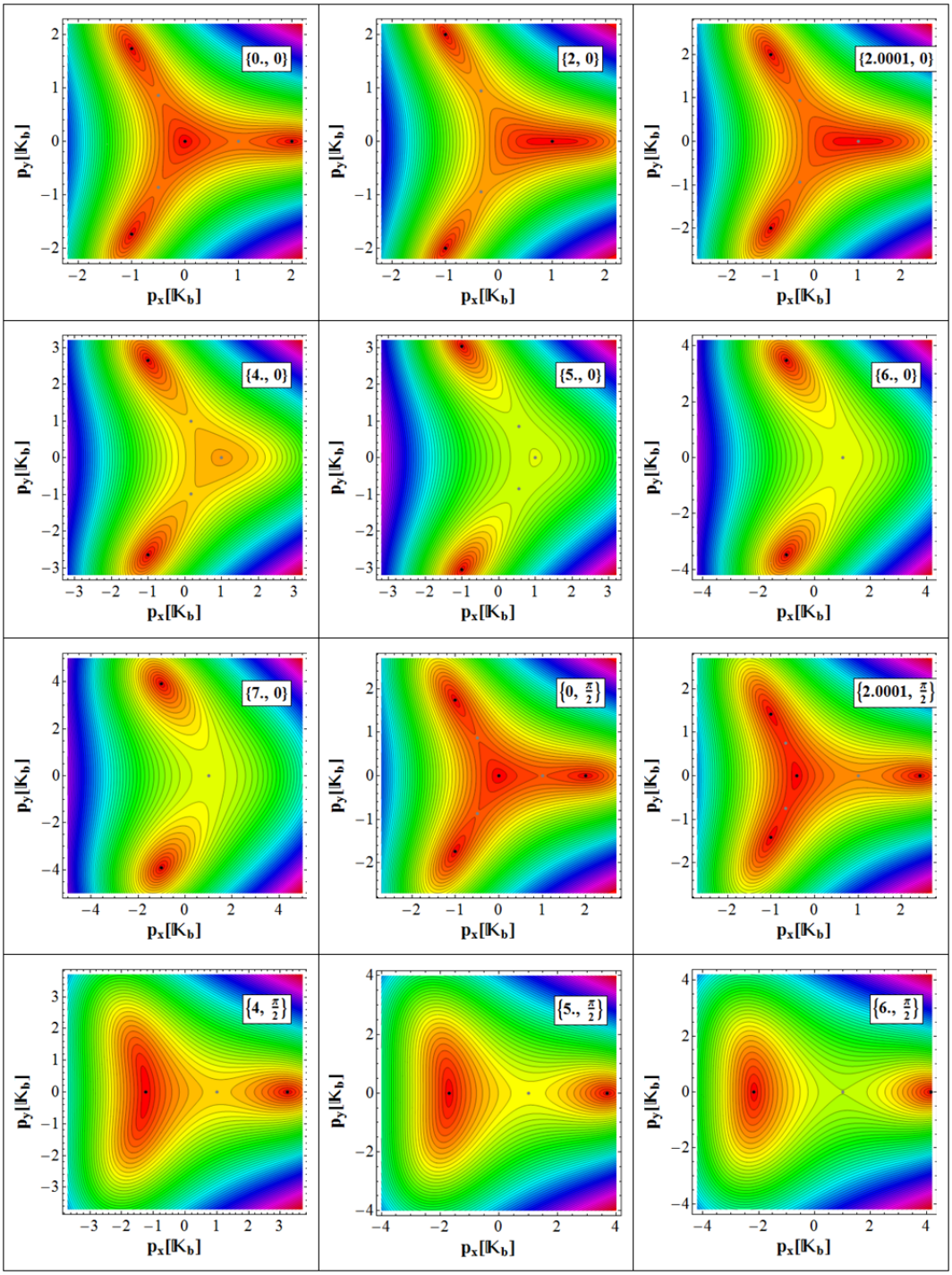

Figure 4.3: Isoenergetic contours of conduction low–energy band of bilayer graphene under in–plane magnetic field for magnetic field in the $\varphi = 0$ and the $\varphi = \pi/2$ direction, where $\left\{\tilde{\beta}, \varphi\right\}$ are determined for each diagram where black points are DPs and grey points are saddle points or minima. In addition, for all of contour diagrams, shorter wavelength of colour indicates higher energy of the band structure. We use $\delta = \gamma_4 = \Delta = 0$.

These equations can be solved numerically. The result of such a procedure is shown in Fig. 4.4 which shows the phase diagram.

In fact, the determinant of the Hessian matrix is a determining factor for the phase diagram, as well. If the determinant of the Hessian matrix is positive, there is a local extremum there. If the determinant of the Hessian matrix is negative there is a saddle point and if it is zero, no conclusion can be made.

The area of the phase diagram where there are two DPs should be separated into two parts. One part contains two DPs and one minimum, and the other contains two DPs only. To find the borders between these parts, first, the determinant of the Hessian matrix of the second derivative should be equal to zero:

$$\begin{aligned} \det \quad \text{Hessian} \quad & = 16(4 + 28\tilde{p}^2 + 3\tilde{p}^4 + 12\tilde{p}^3 \cos 3\phi\big) \\ & -\big(\tilde{\beta}_x^2 + \tilde{\beta}_y^2\big)^2 + 8\tilde{p}^2\big(\tilde{\beta}_x^2 - \tilde{\beta}_y^2\big)\cos 2\phi \\ & +16\big(\tilde{\beta}_x\tilde{\beta}_y\tilde{p}^2 \sin 2\phi + 6\tilde{\beta}_x\tilde{\beta}_y\tilde{p}\sin\phi \\ & +3\big(\tilde{\beta}_x^2 - \tilde{\beta}_y^2\big)\tilde{p}\cos\phi\big) = 0. \end{aligned} \tag{4.10}$$

In addition, two derivatives of the dispersion relation should be equal to zero

$$\tilde{p}\big(8{+}4\tilde{p}^2\big)\cos\phi{-}12\tilde{p}^2\cos 2\phi{+}2\tilde{p}\tilde{\beta}_x\tilde{\beta}_y\sin\phi{+}\tilde{p}\cos\phi\big(\tilde{\beta}_x^2{-}\tilde{\beta}_y^2\big){+}\tilde{\beta}_y{}^2{-}\tilde{\beta}_x{}^2 = 0, \tag{4.11}$$

$$\tilde{p}\sin\phi\big(8 + 4\tilde{p}^2 + 24\tilde{p}\cos\phi\big) - \tilde{p}\sin\phi\big(\tilde{\beta}_x{}^2 - \tilde{\beta}_y{}^2\big) + 2\tilde{\beta}_x\tilde{\beta}_y\big(1 + \cos\phi\big) = 0. \tag{4.12}$$

Solutions of these equations occur for $\tilde{p} = 1$ (i.e. $p = K_b$). For this magnitude of $\tilde{p}$, if the magnetic field is zero, saddle point are a distance K_b from the origin [21]. Then, we determine the values of $\tilde{\beta}_x$, $\tilde{\beta}_y$ and ϕ which solve the above equations. The boundaries of the phase diagram are thus found by plotting all these ($\tilde{\beta}_x$,$\tilde{\beta}_y$) values for $0 \leq \phi \leq \pi/2$.

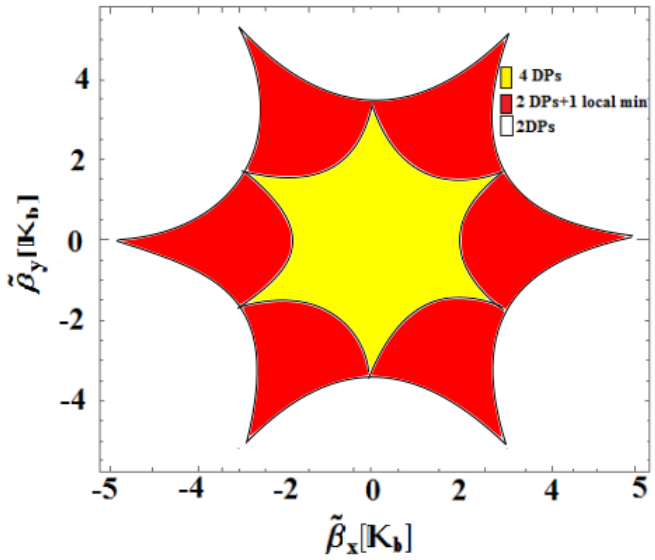

Figure 4.4: Phase diagram of bilayer graphene in a parallel magnetic field where $(\tilde{\beta}_x, \tilde{\beta}_y)$ indicates dimensionless magnetic field as described in the main text. The yellow region is where the low–energy dispersion of bilayer graphene has four DPs, the red region is where there are two DPs and one minimum. The white part is where there are two DPs. We set $\delta = \gamma_4 = \Delta = 0$. Note that $\tilde{\beta} = 1K_b$ is equal to a magnetic field strength about 138 Tesla.

4.3 The effect of in–plane magnetic field on the Lifshitz transition taking small parameters γ_4 and δ into account

To take account of γ_4 and δ, we consider the Hamiltonian of bilayer graphene in a parallel magnetic field (Eq. 3.8 with $\Delta = 0$):

$$\begin{aligned} H \quad &= -\frac{v^2}{\gamma_1}\begin{pmatrix} 0 & \left(\xi p_x - i p_y\right)^2 \\ \left(\xi p_x + i p_y\right)^2 & 0 \end{pmatrix} + v_3 \begin{pmatrix} 0 & \xi p_x + i p_y \\ \xi p_x - i p_y & 0 \end{pmatrix} \\ &\quad -\frac{2v^2}{\gamma_1}\left(\frac{v_4}{v} + \frac{\delta}{\gamma_1}\right)\left(\mathbf{p}\times\boldsymbol{b}\right)_z \begin{pmatrix} 1 & 0 \\ 0 & -1 \end{pmatrix} - \frac{v^2}{\gamma_1}\begin{pmatrix} 0 & \left(\xi b_x - i b_y\right)^2 \\ \left(\xi b_x + i b_y\right)^2 & 0 \end{pmatrix}. \end{aligned} \tag{4.13}$$

The linear–in–magnetic field term was not considered in Section 4.2. We make H dimensionless by dividing by γ_1 and we use $\mathbf{Z} = v\mathbf{p}/\gamma_1$, $x = vp_x/\gamma_1$, $y = vp_y/\gamma_1$,

$\beta = v\mathbf{b}/\gamma_1$, $\Delta_4 = v_4/v + \delta/\gamma_1$ and $\Delta_3 = v_3/v$, to show that

$$\begin{aligned}\frac{H}{\gamma_1} &= -\begin{pmatrix} 0 & \big(\xi x - iy\big)^2 \\ \big(\xi x + iy\big)^2 & 0 \end{pmatrix} + \Delta_3 \begin{pmatrix} 0 & \xi x + iy \\ \xi x - iy & 0 \end{pmatrix} \\ &\quad -2\Delta_4\big(\mathbf{Z}\times\beta\big)\begin{pmatrix} 1 & 0 \\ 0 & -1 \end{pmatrix} - \begin{pmatrix} 0 & \big(\xi\beta_x - i\beta_y\big)^2 \\ \big(\xi\beta_x + i\beta_y\big)^2 & 0 \end{pmatrix}. \end{aligned} \tag{4.14}$$

Consequently, we have

$$\frac{E}{\gamma_1} - \frac{H}{\gamma_1} = \begin{pmatrix} \varepsilon + 2\Delta_4\big(\mathbf{Z}\times\beta\big)_z & \Theta \\ \Theta^\dagger & \varepsilon - 2\Delta_4\big(\mathbf{Z}\times\beta\big)_z \end{pmatrix}, \tag{4.15}$$

where $\Theta = \big(\xi x - iy\big)^2 - \Delta_3\big(\xi x + iy\big) + \big(\xi\beta_x - i\beta_y\big)^2$ and $\varepsilon = E/\gamma_1$. The eigenvalue of this Hamiltonian is given by

$$\varepsilon = \left[4\Delta_4^2\big(\mathbf{Z}\times\beta\big)_z^2 + \Big|\big(\xi x - iy\big)^2 - \Delta_3\big(\xi x + iy\big) + \big(\xi\beta_x - i\beta_y\big)^2\Big|^2\right]^{\frac{1}{2}}. \tag{4.16}$$

To get a DP the eigenvalue should be zero. The Δ_4 term tends to open a gap in the spectrum, dependent on the relative direction of $\mathbf{p}$ and $\mathbf{B}$. It is either positive or zero. In addition, the second part is the modulus of a complex number, so it is also either zero or a positive number. For the first term to be zero, we must have $\mathbf{p} \parallel \mathbf{B}$. Note that $\mathbf{p} = 0$ is not a DP, because of the finite magnetic field in the second term.

To find a DP, the second part of Eq. 4.16 should be equal to zero under the constraint that $\mathbf{p} \parallel \mathbf{B}$. To find these zeroes, we set the magnetic field direction to be parallel to the momentum:

$$\beta_x = s\alpha x, \quad \beta_y = s\alpha y, \quad \alpha = \frac{|\beta|}{Z}, \tag{4.17}$$

where $s = +1(-1)$ for parallel (anti–parallel) magnetic field and momentum, $|\beta| =$

$\sqrt{\beta_x^2+\beta_y^2}$ and $Z=\left|\bar{Z}\right|=\sqrt{x^2+y^2}$. Then, we need to solve

$$2^{\text{nd}}\text{term}=\left|\left(\xi x-iy\right)^2-\Delta_3\left(\xi x+iy\right)+\left(\xi s\alpha x-is\alpha y\right)^2\right|^2=0, \quad (4.18)$$

$$\Rightarrow\left|(1+\alpha^2)\left(\xi x-iy\right)^2-\Delta_3\left(\xi x+iy\right)\right|^2=0. \quad (4.19)$$

To solve this equation, we use polar coordinates with $\xi x+iy=\xi Z\exp(i\xi\phi)$ and determine the modulus squared,

$$\left(1+\frac{|\beta|^2}{Z^2}\right)^2 Z^2-2\xi\Delta_3\left(1+\frac{|\beta|^2}{Z^2}\right)Z\cos 3\phi+\Delta_3^2=0. \quad (4.20)$$

We define a new variable $\zeta=\left(1+|\beta|^2/Z^2\right)Z$ giving

$$\zeta^2-2\xi\Delta_3\zeta\cos 3\phi+\Delta_3^2=0. \quad (4.21)$$

However, this is just the equation that would have come from the Hamiltonian for field $\mathbf{B}=0$ for which the location of the DPs is known as shown in Fig. 4.1 [19].

To find a Dirac point, because the first part and the last part are always positive, the second term should always be negative and its angular part should be a maximum. Hence, for $\xi=1$, ϕ should be $0°$, $120°$ and $-120°$. For the other valley ($\xi=1$) these angles should be $180°$, $60°$ and $-60°$ and magnitude of the momentum is $\zeta=\Delta_3$, i.e. $p=\gamma_1 v_3/v^2$ [19].

For the magnetic field dependent answer, we can use the same solution $\zeta=\Delta_3$ in combination with the definition of ζ, $\zeta=(1+|\beta|^2/Z^2)Z$, for $|\beta|\neq 0$, yielding $Z^2-Z\Delta_3+\beta^2=0$. The two solutions of the equation $Z^2-Z\Delta_3+\beta^2=0$ are

$$Z=\frac{1}{2}\left(-\sqrt{\Delta_3^2-4\beta^2}+\Delta_3\right), \quad (4.22)$$

and

$$Z=\frac{1}{2}\left(+\sqrt{\Delta_3^2-4\beta^2}+\Delta_3\right). \quad (4.23)$$

Hence, we have

$$p = \frac{\gamma_1}{2v}\left(-\sqrt{\frac{v_3}{v} - 4\left(\frac{v}{\gamma_1}\frac{ed}{2}B\right)^2} + \frac{v_3}{v}\right), \tag{4.24}$$

and

$$p = \frac{\gamma_1}{2v}\left(\sqrt{\frac{v_3}{v} - 4\left(\frac{v}{\gamma_1}\frac{ed}{2}B\right)^2} + \frac{v_3}{v}\right). \tag{4.25}$$

Consequently, for $0 < \beta < \Delta_3/2$ there are two Dirac points, and as the value of β increases, they move towards each other. At $\beta = \Delta_3/2$, they annihilate and, for higher magnetic field values, there are no DPs, only a gapped spectrum. The value $\beta = \Delta_3/2$ corresponds to an actual field value of $B = 138$T. Note, however, that such DPs, only occur at certain angles $0°$, $120°$, $-120°$ for the first valley ($\xi = +1$), and there is an additional constraint that $\mathbf{p} \parallel \mathbf{B}$. In other words, there can only be Dirac points for the first valley ($\xi = +1$) if $\mathbf{B}$ is oriented in directions $0°$, $60°$, $120°$, $180°$, $-60°$, $-120°$ ($\mathbf{B}$ can be in the opposite direction to $\mathbf{p}$, too). Numerical results are derived based on the method described in Sec. 4.2 by Eq. 4.4. The analytical results are consistent with numerical results (Fig. 4.5).

For magnetic field in the opposite direction, the band structure is the same. So, the phase diagram of bilayer graphene in a parallel magnetic field is as shown in Fig. 4.6. For most directions of $\mathbf{B}$, the spectrum is gapped but, for 6 special directions, there are two Dirac points (assuming $|\mathbf{B}| < 138$ T). This Chapter has shown, comparing Fig. 4.4 and 4.6, that the linear–in–magnetic field term, arising from the presence of small parameters γ_4 and δ, has a dramatic effect on the band structure at low energy. Nevertheless, such effects should only be noticeable in an experiment using extremely high magnetic field values. In the next Chapter, we consider the influence of the magnetic field on electronic scattering, this requires much smaller magnetic fields to produce an experimentally relevant effect as compared to band structure changes.

To summarize, we have studied the topology of the low–energy band structure of bilayer graphene. At low energy, small parameters skew interlayer coupling and nonuniform on–site energies have been considered. We have shown that as the

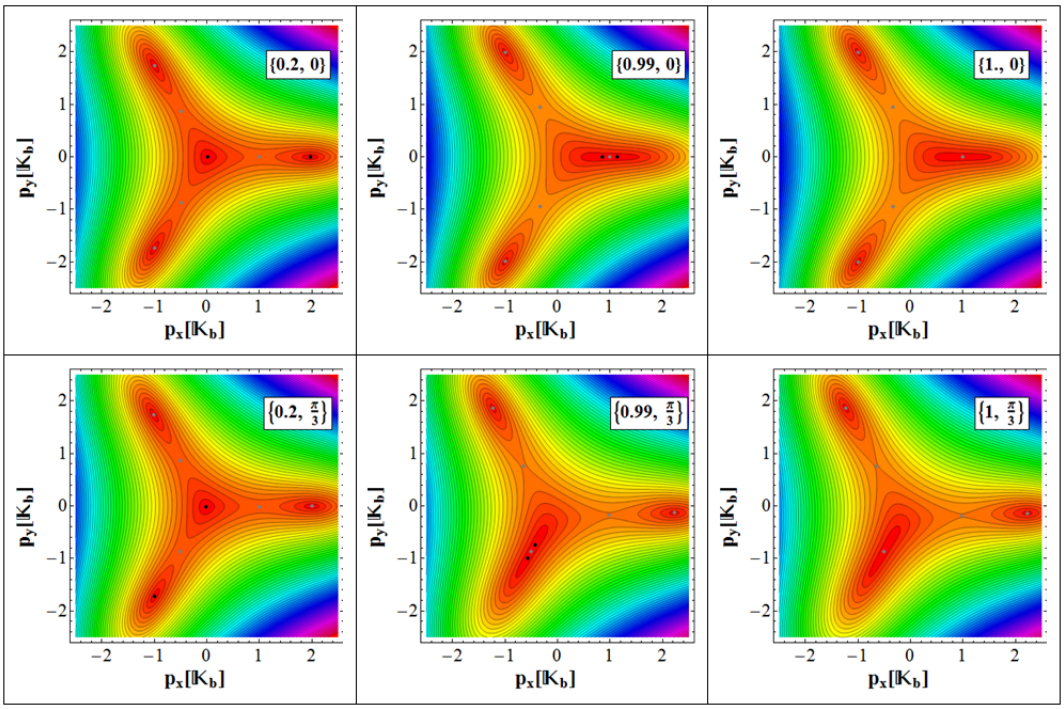

Figure 4.5: Schematic of isoenergetic contours for k_+ valley for $\gamma_4 \neq 0$, $\delta \neq 0$ considering the lowest energy conduction band; dark black points are DPs while the grey points are extrema. $\{\tilde{\beta}, \varphi\}$ is written on each diagram.

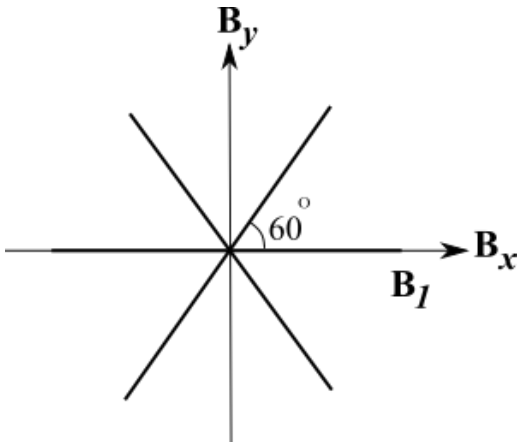

Figure 4.6: Schematic of the phase diagram of bilayer graphene considering all hopping factors (including γ_4 and δ) where $B_1 = (v_3\gamma_1)/(v^2ed)$ is about 138 T. Black lines determine the magnetic field strength and direction where there are 2DPs in the band structure and the white area is the area where there are no DPs in the band structure of bilayer graphene (the spectrum is gapped).

result of this consideration, phase diagram is changed drastically, so that there are only two phases in this diagram. For one phase, in specific directions, there are only two Dirac points for magnetic field under 138 T and other phase is no Dirac point phase.

Chapter 5

Ratchet current in bilayer graphene

5.1 Introduction

The magnetic ratchet effect is the production of a dc electric current in response to a steady in–plane magnetic field and an alternating electric field, in the presence of spatial asymmetry [31]. This is similar to what happens in a mechanical ratchet machine in which an alternating applied force causes a one way rotation of a ratchet wheel. The magnetic ratchet effect has been studied theoretically in semiconductor quantum wells [31; 41; 51] in which the inversion symmetry has been broken and a laser radiation creates an alternating electric field [30]. Experimental observation of the magnetic ratchet effect has been reported in monolayer graphene with symmetry broken by the presence of adatoms [29] or a superlattice [30] (for a review of nonlinear optical and optoelectronic effects in graphene see Ref. [52]).

The magnetic quantum ratchet effect is more intriguing in bilayer graphene. We describe two different mechanisms to break inversion symmetry, either a different density of impurities on the two layers of the bilayer or interlayer–symmetry breaking due to the presence of an external gate, the latter mechanism provid-

ing a natural way to tune the ratchet effect. By comparison with the analysis of Ref. [29], we predict the ratchet effect to be up to two orders of magnitude greater in bilayer graphene than in monolayer. According to Fig. 5.1, for bilayer

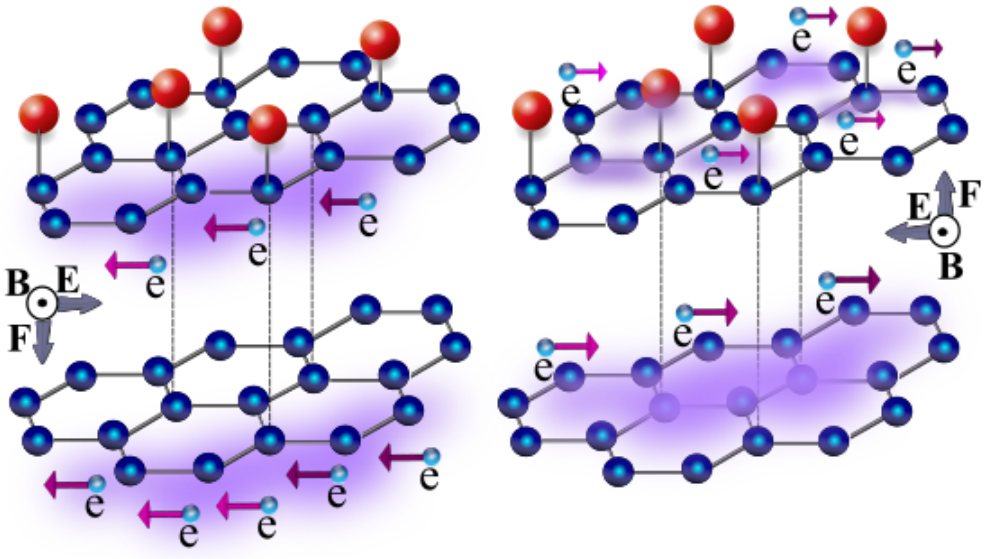

Figure 5.1: Bilayer graphene (blue circles) illustrating the ratchet effect in the presence of an in–plane magnetic field **B** (out of the page), an alternating electric field **E** (to the right or to the left) and layer asymmetry illustrated by impurities (red circles) on the upper layer. Electrons are driven towards the lower or upper layer by the Lorentz force, resulting in a relatively high or low mobility, depending on the presence of impurities.

graphene where the asymmetry is caused by a larger density of impurities on the upper layer, laser radiation which produces an alternating electric field breaks the equilibrium. For a given direction of electric field (to the right as shown in the left side of Fig. 5.1), electrons are driven downwards by the Lorentz force towards the lower layer where, owing to an absence of impurities, the mobility is relatively high. When the electric field alternates to the opposite direction, electrons are driven upwards towards the upper layer where, owing to the presence of impurities, the mobility is relatively low. Asymmetry in mobility depending on the direction of electron motion leads to the presence of a non–zero dc current [51; 29]. Here, we contend that bilayer graphene is a natural system in which spatial symmetry may be broken and, thus, in which the magnetic ratchet could be observed.

To model it, we use the tight–binding model in the presence of a magnetic field as described in Chapter 3 and we employ the Boltzmann kinetic equation (BKE)

to calculate the current. To begin, we make some remarks about the general form of the magnetic ratchet current and the response to different polarisations of light.

5.1.1 Symmetry of the current

In the presence of an alternating electric field with components $\mathbf{E}_x$, $\mathbf{E}_y$, and a steady magnetic field with components $\mathbf{B}_x$, $\mathbf{B}_y$, the resulting current density is $\mathbf{J}$. $\mathbf{J}$ and $\mathbf{E}$ are vectors and $\mathbf{B}$ is an axial vector. Under a $\pi/2$ degree rotation of the coordinates, in the $x-y$ plane, we can show that

$$\mathbf{J}_x^{new} = \mathbf{J}_y, \quad \mathbf{J}_y^{new} = -\mathbf{J}_x, \quad \mathbf{E}_x^{new} = \mathbf{E}_y, \quad \mathbf{E}_y^{new} = -\mathbf{E}_x, \quad \mathbf{B}_x^{new} = \mathbf{B}_y, \quad \mathbf{B}_y^{new} = -\mathbf{B}_x,$$

while the direction of a perpendicular magnetic field (if present) remains unchanged. Also, reflection from the $z-y$ plane results in

$$\mathbf{J}_x^{new} = -\mathbf{J}_x, \quad \mathbf{J}_y^{new} = \mathbf{J}_y, \quad \mathbf{E}_x^{new} = -\mathbf{E}_x, \quad \mathbf{E}_y^{new} = \mathbf{E}_y, \quad \mathbf{B}_x^{new} = -\mathbf{B}_x, \quad \mathbf{B}_y^{new} = \mathbf{B}_y,$$

and, for perpendicular magnetic field, $\mathbf{B}_z^{new} = \mathbf{B}_z$. Using these symmetry relations, it is possible to derive the general form of the dc ratchet current [52]:

$$\begin{aligned} J_x \quad &= M_1[B_y(|E_x|^2 - |E_y|^2) - B_x(E_x E_y^* + E_y E_x^*)] \\ &+ M_2 B_y |E|^2 + M_3 B_x i(E_x E_y^* - E_y E_x^*), \end{aligned} \tag{5.1}$$

$$\begin{aligned} J_y \quad &= M_1[B_x(|E_x|^2 - |E_y|^2) + B_y(E_x E_y^* + E_y E_x^*)] \\ &- M_2 B_x |E|^2 + M_3 B_y i(E_x E_y^* - E_y E_x^*). \end{aligned} \tag{5.2}$$

Here, the coefficients M_1, M_2, M_3 describe the current response to different light polarizations. The coefficients M_1, M_2, M_3 are zero in systems with spatial inversion symmetry because current density $\mathbf{J}$ and electric field $\mathbf{E}$ are odd with respect to spatial inversion, whereas the magnetic field $\mathbf{B}$, being an axial vector, is even

(this is the case for the second-order nonlinear susceptibility in general) [22**?**].

Linearly polarized light- For linearly polarized light, the form of the electric field in the x and y directions are

$$\mathbf{E}_{\|x} = E_0 \cos\theta, \tag{5.3}$$

$$\mathbf{E}_{\|y} = E_0 \sin\theta, \tag{5.4}$$

where θ is the polarization angle. By substitution of these equations in Eqs. 5.1 and 5.2, we have

$$J_x = M_1[B_y E_0^2 \cos 2\theta - B_x E_0^2 \sin 2\theta] + M_2 B_y E_0^2. \tag{5.5}$$

So, the M_1 and M_2 terms are non–zero, but the M_3 term is zero. A similar analysis could be done for y direction.

Unpolarized light- Unpolarized light can be considered to be linearly–polarized light with a time–dependent polarization angle. The response of the electronic system to unpolarized light is the average of such radiation with respect to the time. As a result, the mathematical form of an unpolarized light is

$$\mathbf{E}_{\|x}(t) = |\mathbf{E}| \cos\theta_t, \tag{5.6}$$

$$\mathbf{E}_{\|y}(t) = |\mathbf{E}| \sin\theta_t, \tag{5.7}$$

and the t index indicates time dependent parameters. By substitution of 5.6 and 5.7 in Eqs. 5.1 and 5.2, we can show that the M_2 term is non–zero, but the M_1 and M_3 terms are zero. This can be seen from Eq. 5.5, where an average over θ_t of the M_1 term yields zero because the averages of $\cos 2\theta_t$ and $\sin 2\theta_t$ are zero.

Circular polarized light- If $\mu = +1$ and $\mu = -1$ are referred to as left–hand and right–hand circular polarized light, respectively, then, for circularly–polarized

light, the form of $E_{\parallel x}$ and $E_{\parallel y}$ are

$$\mathbf{E}_{\parallel x} = E_0, \tag{5.8}$$

$$\mathbf{E}_{\parallel y} = i\mu E_0. \tag{5.9}$$

Substitution into Eqs. 5.1 and 5.2 shows that the M_2 and M_3 terms remain non–zero, but the M_1 term is zero. Thus, to summarize, M_2 characterizes the effect of unpolarized light, M_1 describes additional terms if the light is linearly–polarized, M_3 describes additional terms for circular polarization.

To calculate the ratchet current, we use the Boltzmann kinetic equation and we calculate the electron scattering rate by use of the eigenstates of the low–energy Hamiltonian of bilayer graphene discussed in the previous Chapter. This is described in the next Section.

5.2 Boltzmann kinetic equation

In statistical mechanics, the equilibrium distribution of particles over a set of energy levels obeys the Fermi–Dirac distribution function. In a non–equilibrium statistical system, δf describes the change of the Fermi distribution function defined by the BKE. BKE describes the statistical behaviour of a thermodynamic system not in thermodynamic equilibrium [53]. The Boltzmann kinetic equation, which is a semiclassical point of view, suggests a method to calculate the time dependent distribution function of electrons out of equilibrium; the non–equilibrium distribution of a 2D electron gas produced by an external force could be the source of a current. The general form of the Boltzmann kinetic equation is

$$\frac{\partial f}{\partial t} = \left(\frac{\partial f}{\partial t}\right)_{\text{force}} + \left(\frac{\partial f}{\partial t}\right)_{\text{diff}} + \left(\frac{\partial f}{\partial t}\right)_{\text{coll}}. \tag{5.10}$$

Based on the above equation, the change of the electron distribution function with time is caused by the applied external force, time dependent internal forces and the

force acting on the electrons during collisions, respectively. For a 2D electron gas in a parallel magnetic field and under perpendicular laser radiation, the in–plane electric field of the laser is the source of the external force and, consequently, the in–plane current. Because the Lorentz force caused by the in–plane magnetic field pushes electrons perpendicular to the graphene plane, the in–plane electric field, $\mathbf{E}_{\parallel}(\mathbf{t})$, is the source of the in–plane alternating electron motion.

If $\mathbf{E}_{\parallel}(t)$ is considered as a complex amplitude of the electric field, we have

$$\mathbf{E}_{\parallel}(t) = \mathbf{E}_{\parallel} e^{-i\omega t} + \mathbf{E}_{\parallel}^{*} e^{i\omega t}, \tag{5.11}$$

where ω is the angular frequency of the laser radiation. Consequently, the Boltzmann kinetic equation for a 2D electron gas under laser radiation and consisting of particles with energy ϵ and momentum $\mathbf{p} = (p_x, p_y)$ is

$$\frac{\partial f(\mathbf{p},t)}{\partial t} - e\mathbf{E}_{\parallel}(t) \cdot \frac{\partial f(\mathbf{p},t)}{\partial \mathbf{p}} = Stf(\mathbf{p},t). \tag{5.12}$$

In this equation, the electron distribution function, $f(\mathbf{p},t)$, is dependent on the electron momentum and the time, e is the electron charge, and $Stf(\mathbf{p},t)$ is the collision integral [51]. For $W_{\mathbf{p'p}}$ as the rate of the elastic scattering between incoming electrons with a momentum $\mathbf{p}$ and outgoing electrons with a momentum $\mathbf{p'}$, the collision integral is

$$Stf(\mathbf{p},t) = \sum_{\mathbf{p'}} [W_{\mathbf{pp'}} f(\mathbf{p'},t) - W_{\mathbf{p'p}} f(\mathbf{p},t)]. \tag{5.13}$$

Additionally, according to the golden rule, the transition rate between $\mathbf{p}$ and $\mathbf{p'}$ states under a scattering potential, $V_{\mathbf{p'p}}$, is

$$W_{\mathbf{p'p}} = \frac{2\pi}{\hbar} \langle |V_{\mathbf{p'p}}|^2 \rangle \delta(\epsilon_{\mathbf{p}} - \epsilon_{\mathbf{p'}}), \tag{5.14}$$

where angular brackets indicate an average over impurity positions. For a per-

turbed electron gas the scattering rate may be written as

$$W_{\mathbf{p'p}} = W^{(0)}_{\mathbf{p'p}} + \delta W_{\mathbf{p'p}}, \tag{5.15}$$

where $W^{(0)}_{\mathbf{p'p}}$ is the rate of the electron scattering in the absence of parallel magnetic field, and $\delta W_{\mathbf{p'p}}$ is the change of the scattering rate because of the magnetic field.

5.3 General expression of Boltzmann kinetic equation

For electrons in a huge box with periodic boundary conditions, the density of states is $\Gamma = p/(2\pi\hbar^2 v_g)$, where $v_g = \mathrm{d}\epsilon/\mathrm{d}p$. To solve the Boltzmann kinetic equation (Eq. 5.12), we use cylindrical coordinates:

$$-e\mathbf{E}\cdot\nabla_\rho f(\mathbf{p},t) + \frac{\partial f(\mathbf{p},t)}{\partial t} = St(f), \tag{5.16}$$

where

$$\nabla_\rho = \frac{\partial f}{\partial \rho}\mathbf{e}_\rho + \frac{1}{\rho}\frac{\partial f}{\partial \phi}\mathbf{e}_\phi + \frac{\partial f}{\partial z}\mathbf{e_z}. \tag{5.17}$$

The z dependence for our system (a 2D material) is equal to zero. Consequently, the BKE in cylindrical coordinates is

$$-e\mathbf{E}\cdot\left(\frac{\partial f}{\partial p}\mathbf{e_p} + \frac{1}{p}\frac{\partial f}{\partial \phi}\mathbf{e}_\phi\right) + \frac{\partial f}{\partial t} = St(f). \tag{5.18}$$

By substitution of $\mathbf{e}_\phi = (-\sin\phi, \cos\phi, 0)$ and $\mathbf{e_p} = (\cos\phi, \sin\phi, 0)$ in Eq. 5.18, we have

$$-e(E_x\cos\phi + E_y\sin\phi)\frac{\partial f}{\partial p} - \frac{e}{p}\frac{\partial f}{\partial \phi}(-E_x\sin\phi + E_y\cos\phi) + \frac{\partial f}{\partial t} = St(f). \tag{5.19}$$

In a parallel magnetic field, we write the linear–in–field part of the scattering rate of a system of length L as

$$\begin{aligned}\delta W_{\mathbf{p'p}} \quad &= \frac{1}{L^2}\left|u(\mathbf{p'}-\mathbf{p})\right|^2 \delta(\epsilon_{\mathbf{p}}-\epsilon_{\mathbf{p'}}) \\ &\times\Big\{ \left(\Omega_0 - \Omega_c \cos[2(\phi'-\phi)]\right)\left[B_x\left(p_y+p'_y\right) - B_y\left(p_x+p'_x\right)\right] \\ &+\Omega_s \sin[2(\phi'-\phi)]\left[B_x\left(p'_x-p_x\right) + B_y\left(p'_y-p_y\right)\right]\Big\}, \end{aligned} \tag{5.20}$$

this form will be justified when considering bilayer graphene in Section 5.4 We perform a harmonic expansion of the impurity potential,

$$\left|u(\mathbf{p'}-\mathbf{p})\right|^2 = \sum_m \nu_m e^{im(\phi'-\phi)}. \tag{5.21}$$

The fact that it is an even function of $(\phi'-\phi)$ leads to the constraint that $\nu_m = \nu_{-m}$. To determine the current by the Boltzmann kinetic equation (Eq. 5.12) we use a harmonic expansion method. We write that $f(\mathbf{p},t)$ as a series with two indices (n,m):

$$f(\mathbf{p},t) = \sum_{n,m} f_m^n e^{(im\phi - in\omega t)}, \tag{5.22}$$

where ϕ is the polar angle of momentum. To quantify the dc current caused by an alternating electric field, it is necessary to determine time–independent asymmetric parts of the distribution function: the $f^0_{\pm 1}$ terms. Considering the f_m^n prefactors as a function of energy, we can show that BKE has the form

$$\begin{aligned} e(E_x\cos\phi + E_y\sin\phi)\frac{\mathrm{d}\epsilon}{\mathrm{d}p}\sum_{n,m}\frac{\mathrm{d}f_m^n}{\mathrm{d}\epsilon}e^{im\phi-in\omega t} \\ -\frac{ie}{p}(-E_x\sin\phi + E_y\cos\phi)\sum_{n,m} m f_m^n e^{im\phi-in\omega t} \\ +i\omega\sum_{n,m} n f_m^n e^{im\phi-in\omega t} \\ = -St(f). \end{aligned} \tag{5.23}$$

We consider E_x and E_y to be complex numbers

$$E_{\|x}(t) = E_{\|x}e^{-i\omega t} + E^*_{\|x}e^{-i\omega t}, \tag{5.24}$$

$$E_{\|y}(t) = E_{\|y}e^{-i\omega t} + E^*_{\|y}e^{-i\omega t}. \tag{5.25}$$

Multiplying the Boltzmann equation Eq. 5.23 by a factor $\exp(-ij\phi + il\omega t)$, where j, l are integers, and integrating over a period 2π of angle ϕ and a period of time T, leads to coupled equations between different harmonic coefficients. For simplicity, we write these coupled equations using six different parts, named as A, B to G terms. In addition, by considering $\partial f/\partial p = (\mathrm{d}\epsilon/\mathrm{d}p)\mathrm{d}f/\mathrm{d}\epsilon$, we have

$$e\frac{\mathrm{d}\epsilon}{\mathrm{d}p}\,(A+B) + \frac{ie}{p}(C+D) + i\omega F = -G - \delta S, \tag{5.26}$$

where

$$A = \frac{1}{2}\frac{\mathrm{d}}{\mathrm{d}\epsilon}\left[E_{\|x}\left(f^{l-1}_{j-1} + f^{l-1}_{j+1}\right) + E^*_{\|x}\left(f^{l+1}_{j-1} + f^{l+1}_{j+1}\right)\right], \tag{5.27}$$

$$B = \frac{-i}{2}\left[E_{\|y}\left(\frac{\mathrm{d}f^{l-1}_{j-1}}{\mathrm{d}\epsilon} - \frac{\mathrm{d}f^{l-1}_{j+1}}{\mathrm{d}\epsilon}\right) + E^*_{\|y}\left(\frac{\mathrm{d}f^{l+1}_{j-1}}{\mathrm{d}\epsilon} - \frac{\mathrm{d}f^{l+1}_{j+1}}{\mathrm{d}\epsilon}\right)\right], \tag{5.28}$$

$$C = \frac{i}{2}\left[E_{\|x}\left((j-1)f^{l-1}_{j-1} - (j+1)f^{l-1}_{j+1}\right) + E^*_{\|x}\left((j-1)f^{l+1}_{j-1} - (j+1)f^{l+1}_{j+1}\right)\right], \tag{5.29}$$

$$D = \frac{1}{2}\left[E_{\|y}\left((j-1)f^{l-1}_{j-1} + (j+1)f^{l-1}_{j+1}\right) + E^*_{\|y}\left((j-1)f^{l+1}_{j-1} + (j+1)f^{l+1}_{j+1}\right)\right], \tag{5.30}$$

$$F = lf^l_j, \tag{5.31}$$

$$G = -\tau^{-1}_{|j|}f^l_j, \tag{5.32}$$

and we will discuss δS which is the perturbed term explicitly later. Here, we show explicitly how term A is derived:

$$\begin{aligned} A &= \int_0^{2\pi}\int_0^T e^{il\omega t}E_x\cos\phi\sum\frac{\mathrm{d}f^n_m}{\mathrm{d}\epsilon}e^{i(m-j)\phi - in\omega t}\frac{\mathrm{d}t}{T}\frac{\mathrm{d}\phi}{2\pi}, \\ &= \int_0^{2\pi}\int_0^T e^{il\omega t}\left(E_{\|x}e^{-i\omega t} + E^*_{\|x}e^{-i\omega t}\right)\cos\phi\sum\frac{\mathrm{d}f^n_m}{\mathrm{d}\epsilon}e^{i(m-j)\phi - in\omega t}\frac{\mathrm{d}t}{T}\frac{\mathrm{d}\phi}{2\pi}, \end{aligned}$$

$$
\begin{aligned}
&= \int_0^{2\pi} \cos\phi \sum \frac{\mathrm{d}f_m^n}{\mathrm{d}\epsilon} e^{i(m-j)\phi} \frac{\mathrm{d}\phi}{2\pi} \int_0^T e^{i(l-n)\omega t} \left(E_{\parallel x} e^{-i\omega t} + E_{\parallel x}^* e^{-i\omega t} \right) \frac{\mathrm{d}t}{T}, \\
&= \int_0^{2\pi} \cos\phi \sum \frac{\mathrm{d}f_m^n}{\mathrm{d}\epsilon} e^{i(m-j)\phi} \frac{\mathrm{d}\phi}{2\pi} \int_0^T \left(E_{\parallel x} e^{i(l-1-n)\omega t} + E_{\parallel x}^* e^{i(l+1+n)\omega t} \right) \frac{\mathrm{d}t}{T}, \\
&= \int_0^{2\pi} \cos\phi \sum \frac{\mathrm{d}f_m^n}{\mathrm{d}\epsilon} e^{i(m-j)\phi} \frac{\mathrm{d}\phi}{2\pi} \left(E_{\parallel x} \delta_{n,l-1} + E_{\parallel x}^* \delta_{n,l+1} \right), \\
&= \sum \frac{\mathrm{d}f_m^n}{\mathrm{d}\epsilon} \left(E_{\parallel x} \delta_{n,l-1} + E_{\parallel x}^* \delta_{n,l+1} \right) \int_0^{2\pi} \cos\phi e^{i(m-j)\phi} \frac{\mathrm{d}\phi}{2\pi}, \\
&= \sum \frac{\mathrm{d}f_m^n}{\mathrm{d}\epsilon} \left(E_{\parallel x} \delta_{n,l-1} + E_{\parallel x}^* \delta_{n,l+1} \right) \int_0^{2\pi} \frac{1}{2} \left(e^{i\phi} + e^{-i\phi} \right) e^{i(m-j)\phi} \frac{\mathrm{d}\phi}{2\pi}, \\
&= \sum \frac{\mathrm{d}f_m^n}{\mathrm{d}\epsilon} \left(E_{\parallel x} \delta_{n,l-1} + E_{\parallel x}^* \delta_{n,l+1} \right) \int_0^{2\pi} \frac{1}{2} \left(e^{i(m-(j-1))\phi} + e^{i(m-(j+1))\phi} \right) \frac{\mathrm{d}\phi}{2\pi}, \\
&= \frac{1}{2} \sum \frac{\mathrm{d}f_m^n}{\mathrm{d}\epsilon} \left(E_{\parallel x} \delta_{n,l-1} + E_{\parallel x}^* \delta_{n,l+1} \right) \left(\delta_{m,j-1} + \delta_{m,j+1} \right), \\
&= \frac{1}{2} \left(E_{\parallel x} \frac{\mathrm{d}f_m^{l-1}}{\mathrm{d}\epsilon} + E_{\parallel x}^* \frac{\mathrm{d}f_m^{l+1}}{\mathrm{d}\epsilon} \right) \left(\delta_{m,j-1} + \delta_{m,j+1} \right), \\
&= \frac{1}{2} \frac{\mathrm{d}}{\mathrm{d}\epsilon} \left[E_{\parallel x} \left(f_{j-1}^{l-1} + f_{j+1}^{l-1} \right) + E_{\parallel x}^* \left(f_{j-1}^{l+1} + f_{j+1}^{l+1} \right) \right]. \qquad (5.33)
\end{aligned}
$$

The calculations related to other terms are provided in Appendix A. By combining terms, we can show that Eq. 5.26 may be written as

$$
f_j^{(l)} \left(\tau_{|j|}^{-1} - il\omega \right) = \alpha_{j-1} f_{j-1}^{(l-1)} + \eta_{j+1} f_{j+1}^{(l-1)} + \tilde{\alpha}_{j-1} f_{j-1}^{(l+1)} + \tilde{\eta}_{j+1} f_{j+1}^{(l+1)} + \delta S_j^{(l)}, \qquad (5.34)
$$

where the scattering rate (in the absence of magnetic field) is defined as

$$
\tau_{|j|}^{-1} = \frac{2\pi}{\hbar} \sum_{p'} \left| \langle \mathbf{p}' \left| \delta H \right| \mathbf{p} \rangle \right|^2 \delta(\epsilon_{\mathbf{p}} - \epsilon_{\mathbf{p}'}) \left[1 - \cos\left(j[\phi' - \phi] \right) \right], \qquad (5.35)
$$

in the following, we write $\tau_1 = \tau$ for simplicity. Operators arising from the electric field in the Boltzmann kinetic equation are

$$
\alpha_j = \frac{e(E_x - iE_y)}{2} \left(-\frac{j}{p} + \frac{\partial}{\partial p} \right), \qquad (5.36)
$$

$$
\tilde{\alpha}_j = \frac{e(E_x^* - iE_y^*)}{2} \left(-\frac{j}{p} + \frac{\partial}{\partial p} \right), \qquad (5.37)
$$

$$
\eta_j = \frac{e(E_x + iE_y)}{2} \left(\frac{j}{p} + \frac{\partial}{\partial p} \right), \qquad (5.38)
$$

$$\tilde{\eta}_j = \frac{e(E_x^* + iE_y^*)}{2}\left(\frac{j}{p} + \frac{\partial}{\partial p}\right). \tag{5.39}$$

The factors δS_j^l in Eq. 5.34 describe the correction to scattering caused by the magnetic field. Substitution of this expression into the collision integral Eq. 5.13 gives the terms δS_j^l; the relevant ones have small values of j;

$$\begin{aligned}
\delta S_0^l &= 0, \\
\delta S_1^l &= \frac{1}{2}p\Gamma(\epsilon)(B_y - iB_x)\Lambda_1 f_2^l, \\
\delta S_{-1}^l &= \frac{1}{2}p\Gamma(\epsilon)(B_y + iB_x)\Lambda_1 f_{-2}^l, \\
\delta S_2^l &= \frac{1}{2}p\Gamma(\epsilon)\left[(B_y + iB_x)\Lambda_1 f_1^l + (B_y - iB_x)\Lambda_2 f_3^l\right], \\
\delta S_{-2}^l &= \frac{1}{2}p\Gamma(\epsilon)\left[(B_y - iB_x)\Lambda_1 f_{-1}^l + (B_y + iB_x)\Lambda_2 f_{-3}^l\right],
\end{aligned} \tag{5.40}$$

where

$$\Lambda_1 = \Omega(\nu_0 - \nu_2) + \frac{1}{2}\Omega_c(\nu_0 - 2\nu_2 + \nu_4) + \frac{1}{2}\Omega_s(\nu_0 - 2\nu_1 + 2\nu_3 - \nu_4), \tag{5.41}$$

$$\Lambda_2 = \Omega(\nu_0+\nu_1-\nu_2-\nu_3)+\frac{1}{2}\Omega_c(\nu_0-2\nu_2-\nu_3+\nu_4+\nu_5)-\frac{1}{2}\Omega_s(\nu_0-\nu_3-\nu_4+\nu_5). \tag{5.42}$$

The current density is [54]

$$\mathbf{J} = -\frac{g}{L^2}\sum_{\mathbf{p}} e\mathbf{v}_g f(\mathbf{p}, t), \tag{5.43}$$

where $f(\mathbf{p}, t)$ is defined by Eq. 5.22, g is degeneracy factor of electrons, and $\mathbf{v}_g$ is group velocity, the velocity of an electronic wave produced in the material.

In this thesis the total derived current for bilayer graphene is

$$\mathbf{J} = \mathbf{J}^{(0)} + \mathbf{J}^{(1)} + \mathbf{J}^{(2)} + ..., \tag{5.44}$$

where we have

$$\mathbf{J}^{(0)} = -\frac{g}{L^2}\sum_{\mathbf{p}} e\mathbf{v}_g\left(f_1^0 e^{i\phi} + f_{-1}^0 e^{-i\phi}\right), \tag{5.45}$$

$$\mathbf{J}^{(1)} = -\frac{g}{L^2}\sum_{\mathbf{p}} e\mathbf{v}_g \left(f_1^1 e^{i\phi - i\omega t} + f_1^{-1} e^{i\phi + i\omega t} + c.c\right), \tag{5.46}$$

$$\mathbf{J}^{(2)} = -\frac{g}{L^2}\sum_{\mathbf{p}} e\mathbf{v}_g \left(f_{-1}^{-2} e^{i\phi - 2i\omega t} + f_{-1}^{2} e^{i\phi + 2i\omega t} + c.c\right). \tag{5.47}$$

To derive this current we have used two equations:

$$\int_0^{2\pi} \mathbf{v}_g (A\cos\phi + B\sin\phi)\frac{d\phi}{2\pi} = \frac{v_g}{2}(\mathbf{i}A + \mathbf{j}B), \tag{5.48}$$

and

$$\begin{aligned}\sum_{\mathbf{p}}(...) &= L^2\Gamma(\epsilon)\int_0^{2\pi}\frac{\mathrm{d}\phi}{2\pi}\int(...)\mathrm{d}\epsilon, \\ &= \frac{L^2}{4\pi^2\hbar^2}\int_0^{2\pi}\mathrm{d}\phi\int_0^{\infty}(...)p\mathrm{d}p.\end{aligned} \tag{5.49}$$

To derive $J^{(0)}$, we define $\delta f = f_1^0\exp(i\phi) + f_{-1}^0\exp(-i\phi)$. According to Eq. 5.43 [51**?**], we have

$$\begin{aligned}\delta f \quad &= \frac{e^2\Lambda_1\Gamma(\epsilon)B_y\tau\tau_2}{4} \\ &\times\left[(|E_x|^2 - (|E_y|^2)\cos\phi + (E_xE_y^* + E_yE_x^*)\sin\phi\right] \\ &\times\left(p\frac{\partial}{\partial p} - 1\right)\left(\frac{1}{1+i\omega t} + \frac{1}{1-i\omega t}\right)\tau\frac{\partial f_0^0}{\partial p} \\ &+\frac{e^2B_y\tau}{4}\Bigg\{\left[(|E_x|^2 + (|E_y|^2)\cos\phi - (E_xE_y^* - E_yE_x^*)\sin\phi\right] \\ &\times\left(\frac{2}{p} + \frac{\partial}{\partial p}\right)\frac{\Lambda_1\Gamma(\epsilon)p\tau\tau_2}{(1-i\omega\tau_2)(1-i\omega\tau)}\frac{\partial f_0^0}{\partial p} \\ &+\left[(|E_x|^2 + |E_y|^2)\cos\phi + (E_xE_y^* - E_yE_x^*)\sin\phi\right] \\ &\times(\frac{2}{p} + \frac{\partial}{\partial p})\frac{\Lambda_1\Gamma(\epsilon)p\tau\tau_2}{(1+i\omega\tau_2)(1+i\omega\tau)}\frac{\partial f_0^0}{\partial p}\Bigg\}.\end{aligned} \tag{5.50}$$

Based on Eq. 5.50, one can determine that M_i coefficients in Eqs. 5.1 and 5.2 are

$$M_1 = -\frac{ge^3}{16\pi^2\hbar^4}\frac{1}{1+\omega^2\tau^2}[4\Lambda_1 p^2\tau^2\tau_2 + v_g p^3\tau(\Lambda_1\tau\tau_2)'], \tag{5.51}$$

$$M_2 = \frac{ge^3}{16\pi^2\hbar^4}\frac{\Lambda_1 p^2\tau^2\tau_2(1-\omega^2\tau\tau_2)}{(1+\omega^2\tau_2^2)(1+\omega^2\tau^2)}(1 - {v_g}' - \frac{v_g p}{\tau}\tau'), \tag{5.52}$$

$$M_3 = -\frac{ge^3}{16\pi^2\hbar^4}\frac{\Lambda_1 p^2\tau^2\tau_2\omega(\tau+\tau_2)}{(1+\omega^2\tau_2^2)(1+\omega^2\tau^2)}(1 - pv_g{}' - \frac{v_g p}{\tau}\tau'). \tag{5.53}$$

These equations, which generalize those in Refs. [51; 55], describe the ratchet effect in a 2D material with isotropic dispersion. Parameters such as the scattering times τ, τ_2, Eq. 5.35, and Λ_1, Eq. 5.41, describing the effect of in–plane magnetic field will be specific to the given material, in this case bilayer graphene. The frequency dependence of the M_i coefficients is plotted in Fig. 5.2 for the case $\tau_2 = \tau$.

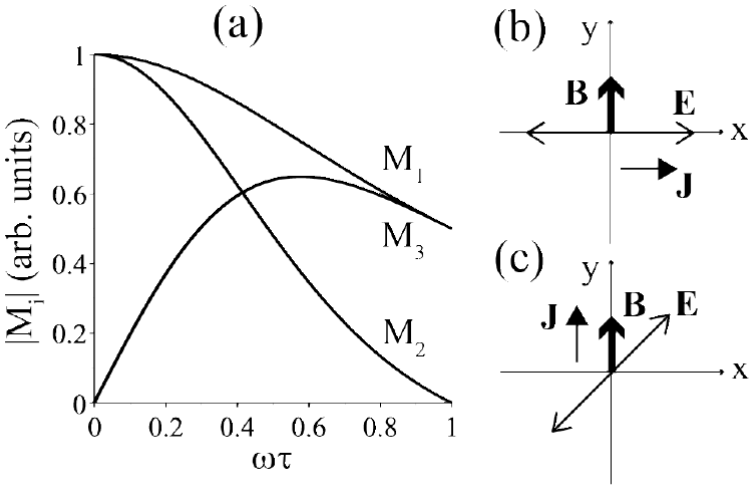

Figure 5.2: (a) frequency dependence of the coefficients M_i, Eq. 5.54 to 5.56, characterizing the polarization dependence of the ratchet current Eq. 5.1 and 5.2. For simplicity, we set $\tau_2 = \tau$. (b) and (c) illustrate the direction of the ratchet current **J** in the graphene $(x - y)$ plane for linear polarization (and $M_1 > 0$) in (b) the x direction, and (c) at 45 to the x–axis [56].

In the following, we assume that the dispersion of bilayer graphene is quadratic $\epsilon = v^2p^2/\gamma_1$ and $v_g = 2v^2p/\gamma_1$, (note that $v_g \neq v$ where v is the group velocity of monolayer graphene). Hence, the M_i factors are

$$M_1 = -\frac{ge^3\Lambda_1 m^*}{4\pi^2\hbar^4}\frac{\epsilon_F\tau[2\tau\tau_2 + \epsilon_F(\tau\tau_2)']}{1+\omega^2\tau^2}, \tag{5.54}$$

$$M_2 = -\frac{ge^3\Lambda_1 m^*}{4\pi^2\hbar^4}\frac{\epsilon_F^2\tau'\tau\tau_2(1-\omega^2\tau\tau_2)}{(1+\omega^2\tau^2)(1+\omega^2\tau_2^2)}, \tag{5.55}$$

$$M_3 = \frac{ge^3\Lambda_1 m^*}{4\pi^2\hbar^4}\frac{\epsilon_F^2\tau'\omega\tau\tau_2(\tau+\tau_2)}{(1+\omega^2\tau^2)(1+\omega^2\tau_2^2)}. \tag{5.56}$$

Here, m^* is the effective mass of the electron, and the derivative is respect to the energy. Parameters such as the scattering time τ, τ_2, Eq. 5.35, and Λ_1, Eq. 5.41,

describing the effect of in–plane magnetic field will be specific to the given material, in this case bilayer graphene.

5.4 Results and discussion for bilayer graphene

Eigenvalues and eigenstates of the perturbed Hamiltonian, Eq. 3.8, can be determined by the first order Born approximation. In particular, we determine the scattering rate of electrons in the perturbed bilayer graphene for two different, representative scattering potentials. If both layers are under the same scattering potential, for instance impurities are equally distributed over both layers, V is proportional to a unit matrix. However, if we assume that the top (bottom) layer is decorated by adatoms, the scattering potential is an asymmetric matrix

$$V = u(r)\frac{I + \zeta\sigma_z}{2}. \tag{5.57}$$

where u(r) is the impurity potential in the $x - y$ plane and $\zeta = +1(-1)$ refers to the disordered top (bottom) layer. According to Eqs. 5.54 to 5.56, the existence of non–zero M_2 and M_3 relies on the energy dependence of the scattering rate τ, irrespective of the effect of the in–plane field. Furthermore, in bilayer graphene, overscreened Coulomb impurities act like short–range scatters [57]

$$u(\mathbf{r} - \mathbf{R}_j) = u_0\delta(\mathbf{r} - \mathbf{R}_j), \tag{5.58}$$

in which case $\tilde{u}(\mathbf{p}' - \mathbf{p}) = u_0$ and the scattering rate is simplified as

$$\text{symmetric disorder:} \quad \tau^{-1} = 2\tau_2^{-1} = \frac{n_i u_0^2 \gamma_1}{4\hbar^3 v^2}, \tag{5.59}$$

$$\text{asymmetric disorder:} \quad \tau^{-1} = \tau_2^{-1} = \frac{n_i u_0^2 \gamma_1}{8\hbar^3 v^2}. \tag{5.60}$$

Furthermore, if u_0 is independent of energy, then so is τ and $M_2 = M_3 = 0$. As the potential is isotropic, $\nu = u_0^2$ is the only non–zero harmonic and parameter Λ_1

simplifies as $\Lambda_1 = u_0^2[\Omega + (\Omega_c + \Omega_s)/2]$.

Symmetric scattering potential or diagonal disorder

According to Eq. 5.14 to 5.20, for the elastic scattering of electrons in a bilayer graphene of dimension L^2, the rate of the scattering under diagonal disorder is 5.14

$$\begin{aligned} W_{p'p} \quad &= \frac{2\pi n_i}{\hbar L^2} \left|u_{\mathbf{p}'-\mathbf{p}}\right|^2 \delta(\epsilon_p - \epsilon_{p'}) \Bigg\{ \frac{1}{2}(1 + \cos[2(\phi' - \phi)]) \\ &+ \frac{\xi\gamma_1\gamma_3\hbar \sin[2(\phi - \phi')]}{\sqrt{3}a\gamma_0^2 p} (\sin 3\phi' - \sin 3\phi) \\ &+ \frac{\gamma_4 \Delta}{2\gamma_0\gamma_1 p^2} \sin 2(\phi' - \phi)(\mathbf{p} - \mathbf{p}') \cdot \mathbf{b} \\ &- \frac{\Delta\gamma_1}{2v^2p^4} \left(\frac{v_4}{v} + \frac{\delta}{\gamma_1}\right) \left(1 - \frac{2v^2p^2}{\gamma_1^2}\right) [1 - \cos[2(\phi' - \phi)]] \left[(\mathbf{p}' + \mathbf{p}) \times \mathbf{b}\right]_z \Bigg\}. \end{aligned} \tag{5.61}$$

In the above equation, n_i is the concentration of impurities, $u_{\mathbf{p}'-\mathbf{p}}$ is the Fourier transform of the impurity potential, $u(\mathbf{r})$, in the $(x-y)$ plane, and it is equal to

$$u_{\mathbf{p}'-\mathbf{p}} = \int_0^\infty u(\mathbf{r}) e^{i(\mathbf{p}-\mathbf{p}')\cdot\mathbf{r}/\hbar} d\mathbf{r}. \tag{5.62}$$

According to Eq. 5.61, for bilayer graphene, the dominant term of the scattering rate is proportional to $[1 + \cos 2(\phi - \phi')]/2$ [13; 57]. In contrast, for a 2D electron gas whose Hamiltonian is not chiral, the scattering rate is 1, and for monolayer, it is proportion to $[1 + \cos(\phi - \phi')]/2$ [57].

According to 5.20, the angular independent factors Ω_0, Ω_c, Ω_s are obtained from the derived scattering rates and those are angle–independent factors

$$\begin{aligned} \Omega_0^{(s)} = \Omega_c^{(s)} \quad &= \frac{\pi e d n_i \Delta\gamma_1}{2\hbar v^2 p^4} \left(\frac{\gamma_4}{\gamma_0} + \frac{\delta}{\gamma_1}\right) \left(1 - \frac{2v^2p^2}{\gamma_1^2}\right), \\ \Omega_s^{(s)} \quad &= \frac{\pi e d n_i \Delta\gamma_4}{2\hbar p^2 \gamma_1\gamma_0}. \end{aligned} \tag{5.63}$$

The evaluation of variables has been done on the Fermi surface for bilayer graphene.

Consequently, we predict a ratchet current caused by asymmetry in the non–dimer on–site energies and the in–plane magnetic field.

According to Eq. 5.54, for symmetric disorder we can show that

$$M_1^{(s)} = \frac{e^4 d\tau^2}{\pi\hbar^2 m(1+\omega^2\tau^2)} \frac{\Delta}{\gamma_1} \left(\frac{5}{2}\frac{\gamma_4}{\gamma_0} + 3\frac{\delta}{\gamma_1} \right), \tag{5.64}$$

where the mass is $m = \gamma_1/2v^2$.

Asymmetric scattering potential

For asymmetric disorder, the scattering potential acts similarly to the σ_z Pauli matrix. This scattering potential alters an out of plane perturbed or unperturbed pseudospin into an in–plane vector, and inversely. As a result, the rate of electron scattering under asymmetric disorder is

$$\begin{aligned} W_{p'\to p} \quad &= \frac{2\pi n_i}{\hbar L^2} \left| u_{\mathbf{p}'-\mathbf{p}} \right|^2 \delta(\epsilon_p - \epsilon_{p'}) \Bigg\{ \frac{1}{4} + \frac{s\zeta\Delta\gamma_1}{4v^2p^2} \left(1 - \frac{2v^2p^2}{\gamma_1^2} \right) \\ &- \left(\frac{v_4}{v} + \frac{\delta}{\gamma_1} \right) \left(s\zeta - \frac{\Delta}{\gamma_1} + \frac{\Delta\gamma_1}{2v^2p^2} \right) \frac{[(\mathbf{p}+\mathbf{p}')\times\mathbf{b}]_z}{2p^2} \\ &- \left(\frac{s\zeta\xi\gamma_1\gamma_3\gamma_4\hbar}{\sqrt{3}a\gamma_0^3} \right) \frac{\cos 3\phi(\mathbf{p}\times\mathbf{b})_z + \cos 3\phi'(\mathbf{p}'\times\mathbf{b})_z}{p^3} \Bigg\}. \end{aligned} \tag{5.65}$$

In the case of asymmetric disorder, considering the essential part of the Hamiltonian causes the rate of the scattering to be independent of the momentum direction in the graphene plane. In fact, the asymmetric disorder destroys the chirality of the incoming electron wave vector. As a result, the dot product of the incoming electron wave vector and the outgoing electron wave vector is independent of momentum directions in the space.

For asymmetric disorder, refer to Eq. 5.20, we have

$$\begin{aligned} \Omega^{(a)} \quad &= \frac{\pi e d n_i}{2\hbar p^2} \left(\frac{\gamma_4}{\gamma_0} + \frac{\delta}{\gamma_1} \right) \left(s\xi - \frac{\Delta}{\gamma_1} + \frac{\Delta\gamma_1}{2v^2p^2} \right), \\ \Omega_c^{(a)} \quad &= \Omega_s^{(a)} = 0. \end{aligned} \tag{5.66}$$

In the case of asymmetric disorder, the switch of the electric field alters the current magnitude. Consequently, the study of the ratchet current under the change of an applied gate voltage provides information about the structure of bilayer graphene.

For bilayer graphene with asymmetric disorder, we can show that

$$M_1^{(a)} = \frac{e^4 d\tau^2}{\pi\hbar^2 m(1+\omega^2\tau^2)} \left(\frac{\delta}{\gamma_1} + \frac{\gamma_4}{\gamma_0}\right) \left(\frac{\Delta}{\gamma_1} - s\zeta\right), \tag{5.67}$$

The expressions for M_1 in Eqs. 5.64 and 5.67 are independent of the Fermi level other than through the factor $s = \pm 1$ for conduction/valence bands. Linear dependence on gate–induced interlayer asymmetry Δ/γ_1 occurs for symmetric disorder because interlayer asymmetry is required to break symmetry in this case, whereas interlayer asymmetry Δ/γ_1 is a small correction for asymmetric disorder (as $\Delta/\gamma_1 << 1$ in general). Note that for linear polarization $E_x = E_0 \cos\theta$, $E_y = E_0 \sin\theta$, where E_0 is real, and $M_2 = M_3 = 0$; so the expression for the ratchet current Eq. 5.1 and 5.2 simplifies as

$$J_x = M_1 E_0^2 (B_y \cos 2\theta - B_x \sin 2\theta), \tag{5.68}$$

$$J_y = M_1 E_0^2 (B_x \cos 2\theta + B_y \sin 2\theta). \tag{5.69}$$

This indicates that the direction of the ratchet current is given by a rotation of the magnetic field direction by an amount determined by the polarization angle, as illustrated in Fig. 5.2 (b) and (c). Assuming the scattering time for bilayer graphene and monolayer graphene is the same, we can show that the magnitude of the ratchet effect in bilayer graphene should be substantial. Parameter values determined by infrared spectroscopy [58] include $\gamma_0 = 3.0eV$, $\gamma_1 = 0.4eV$, $\gamma_4 = 0.015eV$, $\delta = 0.018eV$ and we also use interlayer spacing $d \approx 3.3A^\circ$, $m \approx 0.05m^*$. We compare the magnitude of M_1^{asym} for asymmetric disorder Eq. 5.67 with the theoretical prediction of Ref. [29]. Assuming a typical value $\tau = 0.5$ ps of the scattering time in bilayer graphene and using parameters $|\mathbf{E}| = 10$ kV cm^{-1}, $|B|$

= 7 T, $\omega = 2 \times 10^{-13}$ rad s^{-1} from the experimental results in Ref. [29] for monolayer graphene, we estimate that the ratchet current density for asymmetric disorder is 1 mA cm^{-1}. To the best of our knowledge, there is not any experimental result for bilayer graphene.

5.5 Ratchet current and cyclotron resonance effect

In the presence of a perpendicular magnetic field, electrons will tend to move in circles, an effect known as cyclotron motion. If the angular frequency ω_c (the cyclotron frequency) of this motion coincides with the ac laser frequency ω, there will be a cyclotron resonance effect.

To model cyclotron motion, the Boltzmann kinetic equation is modified as

$$\frac{\partial f(\mathbf{p},t)}{\partial t} - e\left(\mathbf{E}_{\parallel}(t) + \mathbf{v}\times\mathbf{B}\right)\cdot\frac{\partial f(\mathbf{p},t)}{\partial \mathbf{p}} = Stf(\mathbf{p},t), \tag{5.70}$$

where $\mathbf{p}$ is the momentum, $\mathbf{E}_{\parallel}(t) = E_{\parallel}e^{-i\omega t} + E_{\parallel}^{*}e^{i\omega t}$, $\mathbf{v} = d\varepsilon_p/d\mathbf{p}$ and ε_p are the electron energy and velocity for electrons distributed in Fermi distribution function $f(\mathbf{p},t)$ with the collision integral $Stf(\mathbf{p},t)$. Here, we define the magnetic field $\mathbf{B} = (B_x, B_y, B_z)$, with corresponding vector potential $\mathbf{A} = (zB_y - yB_z/2, -zB_x + xB_z/2, 0)$. The cyclotron motion of electrons caused by the Lorentz force changes the form of the ratchet current [59]. The general form of the ratchet current in a 2D electron gas is:

$$\begin{aligned}
\mathbf{J}^{(0)} \quad &= \left(\mathbf{B}_{\parallel}\times\mathbf{n}_z\right)|\mathbf{E}|^2\,\mathrm{Re}[M_2] + \mathbf{B}_{\parallel}\left(i(\mathbf{E}\times\mathbf{E}^*).\mathbf{n}_z\right)\mathrm{Re}[M_3] \\
&-\left\{\left[(\mathbf{n}_z\times\mathbf{B})\cdot\mathbf{E}\right]\mathbf{E}^* + c.c - \left(\mathbf{n}_z\times\mathbf{B}_{\parallel}\right)|\mathbf{E}|^2\right\}\mathrm{Re}[M_1] \\
&-\mathbf{B}_{\parallel}|\mathbf{E}|^2\,\mathrm{Im}[M_2] + \mathbf{B}_{\parallel}\times i(\mathbf{E}\times\mathbf{E}^*)\mathrm{Im}[M_3] \\
&+\left[\mathbf{E}\left(\mathbf{B}_{\parallel}\cdot\mathbf{E}^*\right) + \mathbf{E}^*\left(\mathbf{B}_{\parallel}\cdot\mathbf{E}\right) - \mathbf{B}_{\parallel}|\mathbf{E}|^2\right]\mathrm{Im}[M_1].
\end{aligned} \tag{5.71}$$

In terms of components, it may be written as

$$\begin{aligned} J_x^{(0)} \quad &= |E|^2 \left(B_y \mathrm{Re}[M_2] - B_x \mathrm{Im}[M_2]\right) \\ &+ i\left(E_{\parallel x} E_{\parallel y}^* - E_{\parallel y} E_{\parallel x}^*\right)\left(B_x \mathrm{Re}[M_3] + B_y \mathrm{Im}[M_3]\right) \\ &+ \left(\left|E_{\parallel x}\right|^2 - \left|E_{\parallel y}\right|^2\right)\left(B_x \mathrm{Im}[M_1] + B_y \mathrm{Re}[M_1]\right) \\ &+ \left(E_{\parallel x} E_{\parallel y}^* + E_{\parallel y} E_{\parallel x}^*\right)\left(B_y \mathrm{Im}[M_1] - B_x \mathrm{Re}[M_1]\right), \end{aligned} \tag{5.72}$$

$$\begin{aligned} J_y^{(0)} \quad &= -|E|^2 \left(B_x \mathrm{Re}[M_2] + B_y \mathrm{Im}[M_2]\right) \\ &- i\left(E_{\parallel x} E_{\parallel y}^* - E_{\parallel y} E_{\parallel x}^*\right)\left(B_x \mathrm{Im}[M_3] - B_y \mathrm{Re}[M_3]\right) \\ &+ \left(\left|E_{\parallel x}\right|^2 - \left|E_{\parallel y}\right|^2\right)\left(B_x \mathrm{Re}[M_1] - B_y \mathrm{Im}[M_1]\right) \\ &+ \left(E_{\parallel x} E_{\parallel y}^* + E_{\parallel y} E_{\parallel x}^*\right)\left(B_x \mathrm{Im}[M_1] + B_y \mathrm{Re}[M_1]\right), \end{aligned} \tag{5.73}$$

where the imaginary terms are only non–zero in the presence of non–zero perpendicular magnetic field. In addition, based on Eqs. 5.72 to 5.73, it is possible to show that [59] the general forms of the complex M_i prefactors are

$$M_1 = -\frac{ge^3}{32\pi^2\hbar^4}\left(\frac{1}{\Upsilon^{-1,1}} + \frac{1}{\Upsilon^{1,1}}\right)\left(\frac{4p^2\Lambda_1}{\Upsilon^{0,1}\Upsilon^{0,2}} + v_g p^3 \left(\frac{\Lambda_1}{\Upsilon^{0,1}\Upsilon^{0,2}}\right)'\right), \tag{5.74}$$

$$M_2 = \frac{ge^3}{32\pi^2\hbar^4} p^2 \Lambda_1 \left(\frac{1}{\Upsilon^{1,2}\Upsilon^{1,1}} + \frac{1}{\Upsilon^{-1,2}\Upsilon^{-1,1}}\right)\left(\frac{1}{\Upsilon^{0,1}} - p\left(\frac{v_g}{\Upsilon^{0,1}}\right)'\right), \tag{5.75}$$

$$M_3 = i\frac{ge^3}{32\pi^2\hbar^4} p^2 \Lambda_1 \left(\frac{1}{\Upsilon^{1,2}\Upsilon^{1,1}} - \frac{1}{\Upsilon^{-1,2}\Upsilon^{-1,1}}\right)\left(\frac{1}{\Upsilon^{0,1}} - p\left(\frac{v_g}{\Upsilon^{0,1}}\right)'\right). \tag{5.76}$$

For e as the magnitude of electron charge, $g = g_s g_v$ degeneracy factor, m as the effective mass of electron, Λ_1 is the material specific and $(...)' \equiv \partial(...)/\partial\varepsilon$ when all parameters are evaluated on the Fermi surface. For $\omega_c = 0$ these expressions are the same as Eqs 5.54 to 5.56.

Here, cyclotron frequency is $\omega_c = -eB_z/m$, $\Upsilon^{n,m} = 1/\tau_m - in\omega - im\omega_c$, where n is time contribution and m is angular momentum contribution. The resonance effect in bilayer graphene happens if $n\omega + m\omega_c = 0$. For an electron in bilayer

graphene under 1 T magnetic field, the ω_c and resonance frequency are around 5.524 Trad/s and 0.88 THz, respectively. These amounts correspond to an energy scale equal to 3.62 meV which is much smaller than 100 meV Fermi energy.

Similar to the previous situation without perpendicular magnetic field, the coefficients M_1, M_2, M_3 describe the response to different polarizations of light: M_2 characterizes the effect of unpolarized light, M_1 describes additional terms that appear if the light is linearly polarized, M_3 includes additional terms that occur for circularly polarized light. Accordingly for the case of linear polarized light (Eqs. 5.3 and 5.4), the current density may be expressed as

$$\begin{aligned}\mathbf{J}^{(0)} \quad &= E_0^2 B_\parallel |M_1| \left\{ \hat{\mathbf{i}} \cos\left(2\theta - \varphi - \chi_1 + \frac{\pi}{2}\right) + \hat{\mathbf{j}} \sin\left(2\theta - \varphi - \chi_1 + \frac{\pi}{2}\right) \right\} \\ &+ E_0^2 \Big\{ \left(\mathbf{B}_\parallel \times \hat{\mathbf{n}}_z \mathrm{Re}[M_2] - \mathbf{B}_\parallel \mathrm{Im}[M_2]\right) \Big\}, \end{aligned} \tag{5.77}$$

where $\chi_1 = \arg(M_1)$ and φ is the polar angle of the in–plane magnetic field. The M_1 term produces current in a direction determined by the polarization angle θ and magnetic field direction and the phase of the M_1 coefficient, wherease M_2 describes current in a direction only determined by the parallel field. For unpolarized light, the M_1 related term is zero but the M_2 current survives.

For circularly polarized light, Eqs. 5.8 and 5.9, the current density is

$$\begin{aligned}\mathbf{J}^{(0)} \quad &= 2E_0^2 B_\parallel |M_2| \left\{ \hat{\mathbf{i}} \cos\left(\varphi - \chi_2 - \frac{\pi}{2}\right) + \hat{\mathbf{j}} \sin\left(\varphi - \chi_2 - \frac{\pi}{2}\right) \right\} \\ &+ 2\mu E_0^2 B_\parallel |M_3| \left\{ \hat{\mathbf{i}} \cos\left(\varphi - \chi_3\right) + \hat{\mathbf{j}} \sin\left(\varphi - \chi_3\right) \right\}, \end{aligned} \tag{5.78}$$

where $\chi_2 = \arg(M_2)$ and $\chi_3 = \arg(M_3)$ indicting that the direction of the current is determined by the magnetic field direction and the phase of the M_2 and M_3 coefficients.

For an energy–independent electron scattering rate and quadratic and linear

dispersion, M_2 and M_3 prefactors are zero, and

$$M_1 = -\frac{ge^3}{32\pi^2\hbar^4}\frac{1}{\Upsilon^{0,1}\Upsilon^{0,2}}\left(\frac{1}{\Upsilon^{-1,1}}+\frac{1}{\Upsilon^{1,1}}\right)\left(4p^2\Lambda_1+v_g p^3\Lambda_1'\right). \tag{5.79}$$

In contrast, for a linear energy dispersion, monolayer graphene, we have $\Lambda_1 = \pi\hbar^2 e z_{\pi\sigma}/m^2\epsilon_{\pi\sigma}\tau$ [29], where $z_{\pi\sigma}$ is the coordinate matrix element between the $\pi-$ and $\sigma-$ band states, $\epsilon_{\pi\sigma}$ is the energy distance between the two bands, $V_{\pi\pi}$ and $V_{\pi\sigma}$ are the intraband and interband matrix elements of scattering at zero magnetic field. Hence, we find that

$$M_1 = -\frac{e^4 z_{\pi\sigma}}{2\pi\hbar^2 m^2\epsilon_{\pi\sigma}\tau}p_f^2\frac{1}{\Upsilon^{0,1}\Upsilon^{0,2}}\left(\frac{1}{\Upsilon^{-1,1}}+\frac{1}{\Upsilon^{1,1}}\right). \tag{5.80}$$

For bilayer graphene's quadratic dispersion relation, Λ_1 is

$$\Lambda_1^{(s)} = \frac{\pi e d\hbar^2}{\tau}\Delta\left\{\frac{3}{p^4}\left(\frac{\gamma_4}{\gamma_0}+\frac{\delta}{\gamma_1}\right)-\frac{v^2}{p^2\gamma_1^2}\left(5\frac{\gamma_4}{\gamma_0}+6\frac{\delta}{\gamma_1}\right)\right\}, \tag{5.81}$$

$$\Lambda_1^{(a)} = \frac{2\pi e d\hbar^2}{m\tau}\frac{v^2}{p^2}\left(\frac{\gamma_4}{\gamma_0}+\frac{\delta}{\gamma_1}\right)\left(s\zeta-\frac{\Delta}{\gamma_1}\right), \tag{5.82}$$

where $s = +1(-1)$ for conduction(valence) band and $\zeta = +1(-1)$ where the scattering is limited to the lower (upper layer). For bilayer graphene M_1 is dependent on the symmetry type because Λ_1 is dependent on the type of symmetry or asymmetry condition. Hence, it is shown

$$M_1^{(s)} = \frac{e^4 d}{8\pi\hbar^2 m\tau}\frac{\Delta}{\gamma_1}\left(5\frac{\gamma_4}{\gamma_0}+6\frac{\delta}{\gamma_1}\right)\frac{1}{\Upsilon^{0,1}\Upsilon^{0,2}}\left(\frac{1}{\Upsilon^{-1,1}}+\frac{1}{\Upsilon^{1,1}}\right), \tag{5.83}$$

$$M_1^{(a)} = -\frac{e^4 d}{2\pi\hbar^2 m\tau}\left(s\zeta-\frac{\Delta}{\gamma_1}\right)\left(\frac{\delta}{\gamma_1}+\frac{\gamma_4}{\gamma_0}\right)\frac{1}{\Upsilon^{0,1}\Upsilon^{0,2}}\left(\frac{1}{\Upsilon^{-1,1}}+\frac{1}{\Upsilon^{1,1}}\right). \tag{5.84}$$

The resonance frequencies come from definition of $\Upsilon^{n,m}$ where $n\omega = m\omega_c$. Accordingly, M_1 that is linear response has Drude absorption peculiarity where $\omega = \pm\omega_c$. For M_2 and M_3, the resonance also happens for $\omega = \pm 2\omega_c$ means that the transition between n and $n+2$ becomes possible in the presence of scattering [59].

According to Fig. 5.3, the major effect is related Re[M_1] where there are two res-

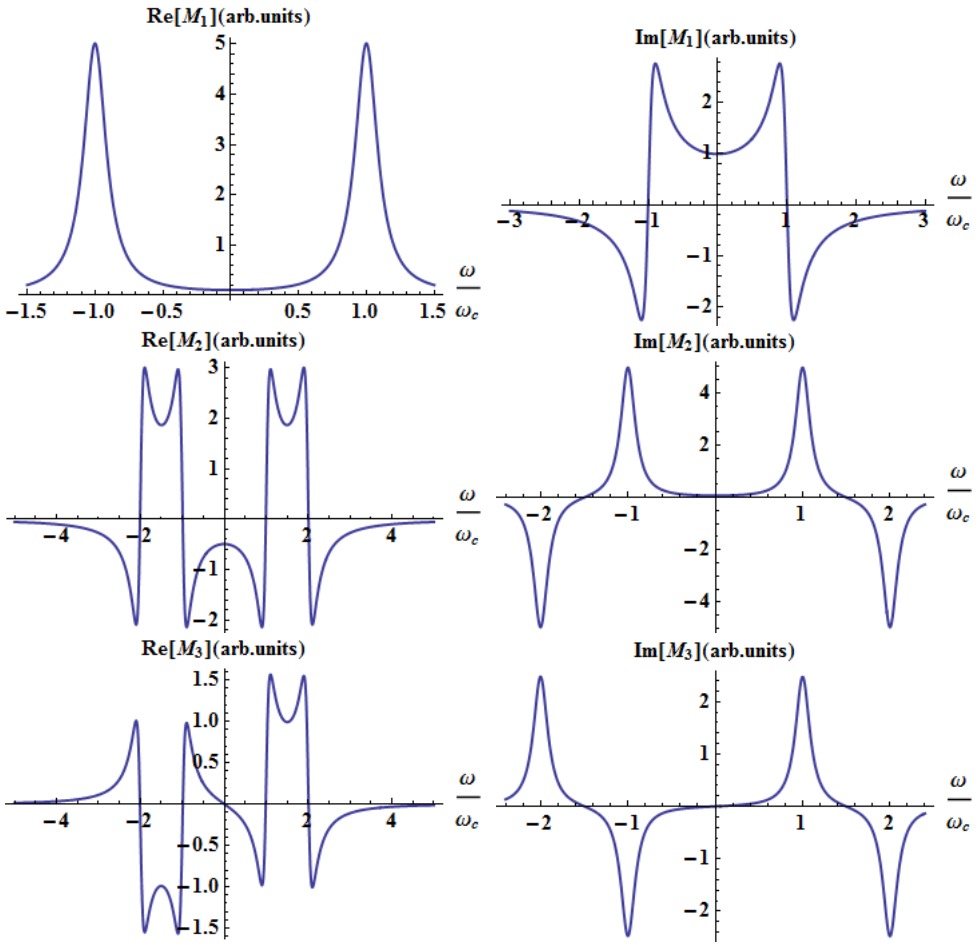

Figure 5.3: Fixed ω_c: Real and imaginary parts of M_i prefactors for asymmetric disorder have been depicted separately. (a) Frequency dependence of the M_1 coefficient (Eq. 5.74) (b) diagram of the resonance effect related to M_2 prefactor (Eq. 5.75), (c) and M_3 prefactor based on Eq. 5.76. We have set $\tau = \tau_2$ and $\tau' = 0$ and $\omega_c\tau = 10$.

onance frequencies there $\omega = \pm\omega_c$. However, Re[M_2] and Re[M_3] each have 4 different resonances; the first one is the stronger effect. These diagrams are related to experiments with $B_\perp$ fixed and a laser radiation whose frequency varies. However, for an experiment with a fixed laser frequency and a changing $B_\perp$ the results are according to Fig. 5.4. Comparing of Fig. 5.3 and 5.4 for the M_1 prefactor shows that, for $\omega_c = 0$, there is a maximum in the current. It means that the cyclotron resonance effect does not actually increase the current with respect to its value at $\omega_c = 0$.

To summarize, we modelled the influence of the new linear term in magnetic field on electronic scattering and its manifestation in the magnetic ratchet effect.

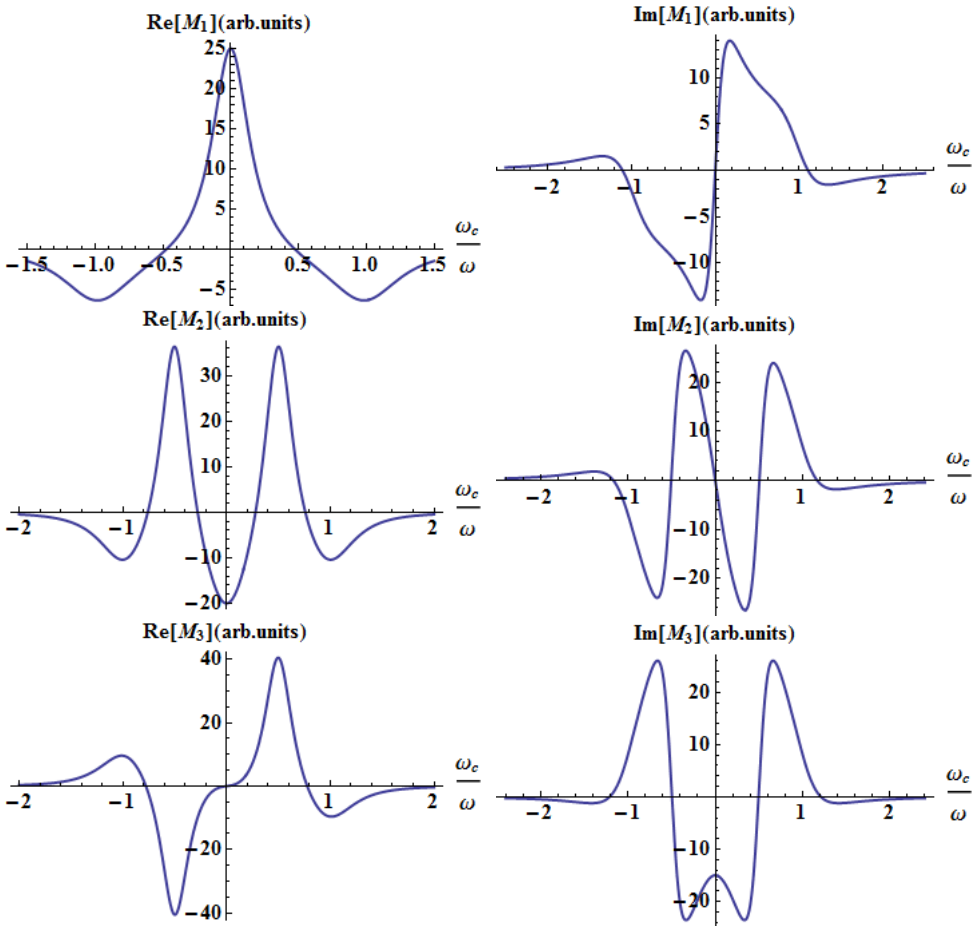

Figure 5.4: Fixed ω: Real and imaginary parts of M_i prefactors for asymmetric disorder where $B \perp$ changes have been depicted separately. (a) Frequency dependence of the M_1 coefficient (Eq. 5.74) (b) diagram of the resonance effect related to M_2 prefactor (Eq. 5.75)(c) M_3 prefactor have been depicted based on Eq. 5.76. We have set $\tau = \tau_2$ and $\tau' = 0$ and $\omega\tau = 3$.

We estimate that the effect should be substantial, two orders of magnitude greater than that in monolayer graphene [29], as well as being sensitive to the nature of disorder and tunable by gate voltage. As detailed in Section 5.5, we have determined the dc current, Eq. 5.71, for the magnetic ratchet in a two-dimensional electron system. These results apply to systems with arbitrary, isotropic dispersion and energy-dependent scattering rates. For the particular case of bilayer graphene, we assume a perfectly quadratic dispersion relation to produce simplified expressions for the dc current under tilted magnetic field, Eqs. 5.74 to 5.76. In addition, in the presence of a tilted field, we find that the dc current has a resonance at $\omega_c = \omega$ but that the current value is actually largest at $\omega_c = 0$.

Chapter 6

Second harmonic generated current

6.1 Introduction

Magneto–optical modulators are in high demand for photonic and optoelectronic devices [60]. They are divided into wave length [61], amplitude [62; 63; 64], phase [62] and polarization modulator [65; 61]. One important phase–modulator mechanism is based on the magneto–optical Faraday–Kerr effect. The Faraday–Kerr effect is the rotation of the polarization angle of a linearly polarized light beam when it passes or reflected from a material kept in a constant magnetic field. For example, the optical property of a material with a refractive index depended on the polarization and propagation direction of light is important for laser application processes. In fact, the majority of optical modulators are based on the strong non–linear optical response of a 2–dimensional material (mainly the third order susceptibility) [60].

It has been shown that the maximum Faraday rotation angle is 6 degrees for far–infrared monolayer graphene kept in a parallel magnetic field of order of $7T$ [66]; for far–infra red radiation the amount of parallel magnetic field to observe the effect is $1T$. Current graphene optoelectronic modulators work under 10 THz frequencies

and graphene plasmonic electro–optic modulators have been demonstrated. It is also reported that a pseudo–magnetic field caused by strain results in a 0.3 rad Faraday–Kerr rotation [67]. The Faraday rotation angle of graphene is small because of the graphene structure.

In this Chapter, we will study ac currents produced in graphene. In addition, we will study different responses of graphene under different light polarization and we will also discuss about the response polarization and characteristics.

6.2 Semi–classical point of view, distribution function of the electron under a time–dependent electric field

Two essential equations to derive the current based on BKE and in the semi–classical regime are Eqs. 5.22 and 5.11; the time dependent electric field changes the electron momentum direction and its magnitude. Hence, 2DEG is not in termal equilibrium, and such an unsteady distribution of electron motion is the origin of the current in the system.

In fact, the magnetic quantum ratchet effect results in a dc current caused by the imbalance of the motion of electrons. As it is shown, the dc current is related to the change of the electron distribution function, the time independent part of $\delta f = f_1^0 \exp(i\phi) + f_{-1}^0 \exp(-i\phi)$. For response to first order ac current, we should consider $f_{\pm 1}^{\pm 1}$, and second harmonic generated current, $\delta f = f_1^2 \exp(i\phi - 2\omega t) + f_1^{-2} \exp(i\phi + 2\omega t) + c.c$, is defined by $f_{\pm 1}^{\pm 2}$ terms of the harmonic expansion of the distribution function Eq. 5.22. This results in a second order ac current in graphene based materials under a parallel magnetic field. To study the interaction of THz with microwave radiation, the Boltzmann kinetic equation is used. As mentioned before, for an in–plane ac field $\mathbf{E}_\parallel(t) = \mathbf{E}_\parallel e^{-i\omega t} + \mathbf{E}_\parallel^* e^{i\omega t}$, the current has been calculated based on distribution functions, Eq. 5.44.

6.3 First order ac current

The first order ac current is the result of Fermi distribution function related to f_1^1 and f_1^{-1} and the complex conjugate of those terms. This current is the result of coupled equations determined by Eq. 5.34 with linear in $\mathbf{E}$ terms where δS is irrelevant,

$$\mathbf{J}^{(1)} = -\frac{g}{L^2}\sum_{\mathbf{p}} e\mathbf{v}_g \left(f_1^1 e^{i\phi - i\omega t} + f_1^{-1} e^{i\phi + i\omega t} + c.c\right). \tag{6.1}$$

In order to determine the first order ac current, in Eq. 5.26 with $\delta S = 0$, we have

$$f_{\pm 1}^{(1)} = \frac{e\tau\left(E_x \mp weE_y\right)}{2\left(1 - i\omega\tau \pm we\omega_c\tau\right)}\frac{\partial f_0^{(0)}}{\partial p}; \qquad f_{\pm 1}^{(-1)} = \left(f_{\mp 1}^{(1)}\right)^*. \tag{6.2}$$

Hence, for a degenerate electron gas, it has been found that $\mathbf{J}^{(1)} = 2\mathrm{Re}\{\sigma\mathbf{E}e^{-i\omega t}\}$ where σ is the first order ac conductivity tensor independent of the radiation polarization, impurity potential and external in–plane magnetic field. Consequently, the ac conductivity of bilayer graphene is

$$\sigma_0 = \frac{ge^2\tau}{2\pi\hbar^2}\epsilon_f, \tag{6.3}$$

which is proportional to the Fermi level ($\epsilon_f = pv_g/2$). This result agrees with previous results [68], where it was shown that the ac conductivity of bilayer graphene is twice that of monolayer graphene and metals based on Drude–Boltzmann theory [69]. The response to linearly polarized light is similar to monolayer graphene; and, for circular polarized light there is circular radiation [70]. In addition, the resonance effect happens when $\omega = \pm\omega_c$.

6.4 Second order ac current, SHG current

The study of SHG is important because non–reversible optoelectronic devices act based on SHG effects. In order to have a second order effect, both time reversal and inversion symmetry should be broken. For bilayer graphene, time reversal is

broken by the magnetic field and the field related terms come with γ_4 and δ factor. Inversion symmetry is broken by on–site energies and by disorder.

To find the second order ac current, we should consider four terms in the Fermi distribution function (Eq. 5.47 and 5.34) where f_{-1}^{-2}, f_{-1}^{2}, coefficients are

$$\begin{aligned} f_{-1}^{-2} \quad &= \frac{1}{\Upsilon^{-2,-1}}\Bigg\{\widetilde{\alpha}_{-2}\frac{1}{\Upsilon^{-1,-2}}\frac{p\Gamma}{2}\Lambda_1(B_y-iB_x)\frac{1}{\Upsilon^{1,-1}}\widetilde{\eta}_0 f_0^0 \\ &+\frac{p\Gamma}{2}\Lambda_1(B_y+iB_x)\frac{1}{\Upsilon^{-2,-2}}\widetilde{\eta}_{-1}\frac{1}{\Upsilon^{-1,-1}}\widetilde{\eta}_0 f_0^0\Bigg\}, \end{aligned} \tag{6.4}$$

$$\begin{aligned} f_{-1}^{2} \quad &= \frac{1}{\Upsilon^{2,-1}}\Bigg\{\alpha_{-2}\frac{1}{\Upsilon^{1,-2}}\frac{p\Gamma}{2}\Lambda_1(B_y-iB_x)\frac{1}{\Upsilon^{1,-1}}\eta_0 f_0^0 \\ &+\frac{p\Gamma}{2}\Lambda_1(B_y+iB_x)\frac{1}{\Upsilon^{2,-2}}\eta_{-1}\frac{1}{\Upsilon^{1,-1}}\eta_0 f_0^0\Bigg\}. \end{aligned} \tag{6.5}$$

For a 2D electronic system with an isotropic dispersion relation, it is possible to show that [71]

$$\begin{aligned} \mathbf{J}^{(2)} \quad &= 2\mathrm{Re}\Bigg[\Bigg\{-2N_1\Big[(\mathbf{n}_z\times\mathbf{B})\cdot\mathbf{E}\mathbf{E}+\left(\mathbf{B}_\parallel\times\mathbf{n}_z\right)\mathbf{E}^2\Big]-N_2\Big[2\mathbf{E}\left(\mathbf{B}_\parallel\cdot\mathbf{E}\right)-\mathbf{B}_\parallel\mathbf{E}^2\Big] \\ &+N_3\left(\mathbf{B}_\parallel\times\mathbf{n}_z\right)\mathbf{E}^2+N_4\mathbf{B}_\parallel\mathbf{E}^2\Bigg\}e^{-2i\omega t}\Bigg], \end{aligned} \tag{6.6}$$

where $\mathbf{E}^2\equiv\mathbf{E}\cdot\mathbf{E}=E_x^2+E_y^2$. Explicitly in terms of components, this is

$$J_x = 2\mathrm{Re}\Bigg\{\left[N_1\left(B_y\Theta_4-B_x\Theta_5\right)-N_2\left(B_x\Theta_4+B_y\Theta_5\right)+\Theta_6\left(B_yN_3+B_xN_4\right)\right]e^{-2i\omega t}\Bigg\}, \tag{6.7}$$

$$J_y = 2\mathrm{Re}\Bigg\{\left[N_1\left(B_x\Theta_4+B_y\Theta_5\right)+N_2\left(B_y\Theta_4-B_x\Theta_5\right)+\Theta_6\left(-B_xN_3+B_yN_4\right)\right]e^{-2i\omega t}\Bigg\}, \tag{6.8}$$

where $\Theta_4=\left(E_x^2-E_y^2\right)$, $\Theta_5=2E_xE_y$, $\Theta_6=\left(E_x^2+E_y^2\right)$. For defined $\mathbf{J}^{(2)}$, Eq. 6.6, we can show that the N_i coefficients are

$$N_1 = -\frac{ge^3v_gp}{32\pi\hbar^2}\Bigg\{\frac{1}{\Upsilon^{1,1}}\left(\frac{v_gp\Gamma\Lambda_1}{\Upsilon^{2,1}\Upsilon^{2,2}}\right)'+\frac{1}{\Upsilon^{1,-1}}\left(\frac{v_gp\Gamma\Lambda_1}{\Upsilon^{2,-1}\Upsilon^{2,-2}}\right)'\Bigg\}, \tag{6.9}$$

$$N_2 = -\frac{ige^3 v_g p}{32\pi\hbar^2}\left\{\frac{1}{\Upsilon^{1,1}}\left(\frac{v_g p\Gamma\Lambda_1}{\Upsilon^{2,1}\Upsilon^{2,2}}\right)' - \frac{1}{\Upsilon^{1,-1}}\left(\frac{v_g p\Gamma\Lambda_1}{\Upsilon^{2,-1}\Upsilon^{2,-2}}\right)'\right\}, \tag{6.10}$$

$$\begin{aligned} N_3 \quad &= \frac{ge^3 v_g p\Gamma\Lambda_1}{32\pi\hbar^2}\left\{\frac{1}{\Upsilon^{2,1}\Upsilon^{1,2}\Upsilon^{1,1}} + \frac{1}{\Upsilon^{2,-1}\Upsilon^{1,-2}\Upsilon^{1,-1}} - \frac{p}{\Upsilon^{1,2}\Upsilon^{1,1}}\left(\frac{v_g}{\Upsilon^{2,1}}\right)'\right. \\ &\left. -\frac{p}{\Upsilon^{1,-2}\Upsilon^{1,-1}}\left(\frac{v_g}{\Upsilon^{2,-1}}\right)'\right\}, \end{aligned} \tag{6.11}$$

$$\begin{aligned} N_4 \quad &= \frac{ige^3 v_g p\Gamma\Lambda_1}{32\pi\hbar^2}\left\{\frac{1}{\Upsilon^{2,1}\Upsilon^{1,2}\Upsilon^{1,1}} - \frac{1}{\Upsilon^{2,-1}\Upsilon^{1,-2}\Upsilon^{1,-1}} - \frac{p}{\Upsilon^{1,2}\Upsilon^{1,1}}\left(\frac{v_g}{\Upsilon^{2,1}}\right)'\right. \\ &\left. +\frac{p}{\Upsilon^{1,-2}\Upsilon^{1,-1}}\left(\frac{v_g}{\Upsilon^{2,-1}}\right)'\right\}. \end{aligned} \tag{6.12}$$

Note that N_2 and N_4 coefficients are only non-zero in the presence of non-zero perpendicular field $\mathbf{B}_\perp$.

6.4.1 Results and discussion

If the electron scattering rate is independent of the electron energy then the N_i coefficients simplify as

$$N_1 = -\frac{ge^3 v_g p}{32\pi\hbar^2}\left(\frac{1}{\Upsilon^{2,1}\Upsilon^{2,2}\Upsilon^{1,1}} + \frac{1}{\Upsilon^{2,-1}\Upsilon^{2,-2}\Upsilon^{1,-1}}\right)(v_g p\Gamma\Lambda_1)', \tag{6.13}$$

$$N_2 = -i\frac{ge^3 v_g p}{32\pi\hbar^2}\left(\frac{1}{\Upsilon^{2,1}\Upsilon^{2,2}\Upsilon^{1,1}} - \frac{1}{\Upsilon^{2,-1}\Upsilon^{2,-2}\Upsilon^{1,-1}}\right)(v_g p\Gamma\Lambda_1)', \tag{6.14}$$

$$N_3 = \frac{ge^3 v_g p\Gamma\Lambda_1}{32\pi\hbar^2}\left\{\left(1 - pv_g'\right)\left(\frac{1}{\Upsilon^{1,2}\Upsilon^{1,1}\Upsilon^{2,1}} + \frac{1}{\Upsilon^{1,-2}\Upsilon^{1,-1}\Upsilon^{2,-1}}\right)\right\}, \tag{6.15}$$

$$N_4 = i\frac{ge^3 v_g p\Gamma\Lambda_1}{32\pi\hbar^2}\left\{\left(1 - pv_g'\right)\left(\frac{1}{\Upsilon^{1,2}\Upsilon^{1,1}\Upsilon^{2,1}} - \frac{1}{\Upsilon^{1,-2}\Upsilon^{1,-1}\Upsilon^{2,-1}}\right)\right\}. \tag{6.16}$$

SHG in monolayer graphene

For monolayer graphene, $\Lambda_1 = \pi\hbar^2 e z_{\pi\sigma}/m^2\epsilon_{\pi\sigma}\tau$ [29; 56], and $v_g = v$, we can show that N_1 and N_2 are equal to zero and N_3 and N_4 are

$$N_3 = \frac{ge^4 z_{\pi\sigma}}{64\pi\hbar^2 m^2\epsilon_{\pi\sigma}\tau} p_f^2 \left(\frac{1}{\Upsilon^{2,1}\Upsilon^{1,2}\Upsilon^{-1,1}} + \frac{1}{\Upsilon^{2,-1}\Upsilon^{1,-2}\Upsilon^{1,-1}} \right), \tag{6.17}$$

$$N_4 = i\frac{ge^4 z_{\pi\sigma}}{64\pi\hbar^2 m^2\epsilon_{\pi\sigma}\tau} p_f^2 \left(\frac{1}{\Upsilon^{2,1}\Upsilon^{1,2}\Upsilon^{-1,1}} - \frac{1}{\Upsilon^{2,-1}\Upsilon^{1,-2}\Upsilon^{1,-1}} \right). \tag{6.18}$$

For monolayer graphene, the increase of the Fermi level by gating increases the electron momentum p_f.

SHG in bilayer graphene

For quadratic dispersion relation of bilayer graphene, $v_g = 2v^2 p/\gamma_1$; and Λ_1 is dependent on the symmetry types as defined in Eqs. 5.81 and 5.82. Consequently, $N_3 = N_4 = 0$, while N_1 and N_2 coefficients for the case of symmetric bilayer graphene are

$$N_1^{(s)} = \frac{3e^4 d}{8\pi\hbar^2\tau}\frac{\Delta}{p^2}\left(\frac{\gamma_4}{\gamma_0} + \frac{\delta}{\gamma_1}\right)\left(\frac{1}{\Upsilon^{2,1}\Upsilon^{2,2}\Upsilon^{1,1}} + \frac{1}{\Upsilon^{2,-1}\Upsilon^{2,-2}\Upsilon^{1,-1}} \right), \tag{6.19}$$

$$N_2^{(s)} = i\frac{3e^4 d}{8\pi\hbar^2\tau}\frac{\Delta}{p^2}\left(\frac{\gamma_4}{\gamma_0} + \frac{\delta}{\gamma_1}\right)\left(\frac{1}{\Upsilon^{2,1}\Upsilon^{2,2}\Upsilon^{1,1}} - \frac{1}{\Upsilon^{2,-1}\Upsilon^{2,-2}\Upsilon^{1,-1}} \right). \tag{6.20}$$

For asymmetric disorder, N_1 and N_2 coefficients are

$$N_1^{(a)} = \frac{e^4 d}{4\pi\hbar^2\tau}\frac{\Delta}{p^2}\left(\frac{\gamma_4}{\gamma_0} + \frac{\delta}{\gamma_1}\right)\left(\frac{1}{\Upsilon^{2,1}\Upsilon^{2,2}\Upsilon^{1,1}} + \frac{1}{\Upsilon^{2,-1}\Upsilon^{2,-2}\Upsilon^{1,-1}} \right), \tag{6.21}$$

$$N_2^{(a)} = i\frac{e^4 d}{4\pi\hbar^2\tau}\frac{\Delta}{p^2}\left(\frac{\gamma_4}{\gamma_0} + \frac{\delta}{\gamma_1}\right)\left(\frac{1}{\Upsilon^{2,1}\Upsilon^{2,2}\Upsilon^{1,1}} - \frac{1}{\Upsilon^{2,-1}\Upsilon^{2,-2}\Upsilon^{1,-1}} \right). \tag{6.22}$$

Note that this is a remarkable result: asymmetric disorder on its own does not produce second harmonic generation, interlayer asymmetry Δ is required.

For linearly polarized light at angle θ and magnetic field direction φ we assume that $\mathbf{B}_\parallel = B_\parallel(\cos\varphi, \sin\varphi, 0)$ and $B_\parallel = \left|\mathbf{B}_\parallel\right|$. SHG related current in response to

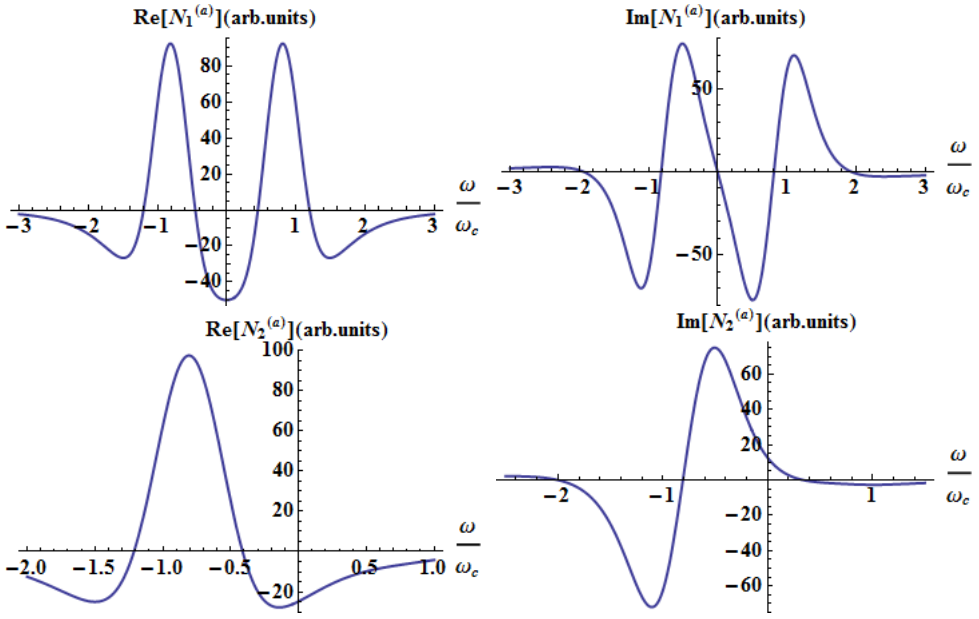

Figure 6.1: Fixed ω_c: $N_1^{(a)}$ and $N_2^{(a)}$ phase related coefficients for SHG current considering the cyclotron resonance effect.

linearly polarized light is

$$\begin{aligned}
\mathbf{J}^{(2)} \quad &= 2E_0^2 B_{\parallel} |N_1| \cos(2\omega t - \psi_1)\{\hat{\mathbf{i}} \cos(2\theta - \varphi + \pi/2) + \hat{\mathbf{j}} \sin(2\theta - \varphi + \pi/2)\} \\
&+2E_0^2 B_{\parallel} |N_2| \cos(2\omega t - \psi_2)\{\hat{\mathbf{i}} \cos(2\theta - \varphi + \pi) + \hat{\mathbf{j}} \sin(2\theta - \varphi + \pi)\} \\
&+2E_0^2 |N_3| \left(\mathbf{B}_{\parallel} \times \hat{\mathbf{n}}_z\right) \cos(2\omega t - \psi_3) \\
&+2E_0^2 |N_4| \mathbf{B}_{\parallel} \cos(2\omega t - \psi_4), \qquad (6.23)
\end{aligned}$$

where the phases $\psi_i = \arg(N_i)$ describe a time lag between the incoming light and produced current. For the N_1 and N_2 terms, the in–plane magnetic field rotates the polarization direction as in the Faraday effect. For the N_3 and N_4 terms, the out going linear polarization direction is only determined by the parallel field (it is independent of the incoming polarization direction θ). For unpolarized light, N_1 and N_2 related currents are zero but the N_3 and N_4 currents survive. Consequently, for unpolarized light, monolayer graphene has a polarized response whose phase rotates as the in–plane magnetic field is rotating. This similarity to the Faraday effect is essential for applications in the field of optical birefringence under polarized light.

For incoming circularly–polarized light, the N_3 and N_4–related currents are zero, and the deduced ac current stimulated by radiation is

$$J_x = 4E_0^2 B_{\parallel} \left[|N_1| \cos\left(2\omega t - \mu\varphi - \psi_1 + \mu\frac{\pi}{2}\right) + |N_2| \cos\left(2\omega t - \mu\varphi - \psi_2 - \pi\right) \right], \tag{6.24}$$

$$J_y = 4E_0^2 B_{\parallel} \left[|N_1| \cos\left(2\omega t - \mu\varphi - \psi_1\right) + |N_2| \cos\left(2\omega t - \mu\varphi - \psi_2 + \mu\frac{\pi}{2}\right) \right], \tag{6.25}$$

and it is also circularly polarized light.

For a varing ω_c and a constant laser radiation frequency, according to Fig. 6.2, we can say that the cyclotron resonance is essential to have a strong SHG current, i.e. in contrast to the M_1 coefficient for the dc current, the cyclotron resonances are generally much stronger than the signal at $\omega_c = 0$.

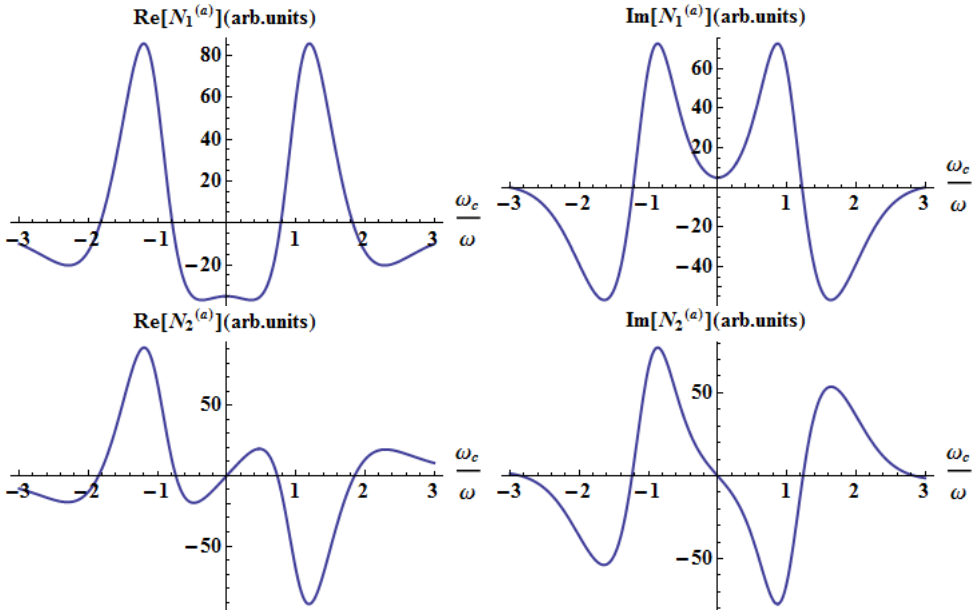

Figure 6.2: Fixed ω: $N_1^{(a)}$ and $N_2^{(a)}$ phase related coefficients for SHG current considering cyclotron resonance effect for a varying magnetic field and a constant Laser radiation frequency

To summarize, we have determined the second harmonic generation, Eq. 6.6, for the magnetic ratchet in the semiclassical regime ($E_F \gg \omega$) in a two-dimensional electron system. These results apply to systems with arbitrary, isotropic dispersion and energy-dependent scattering rates. For the particular case of bilayer graphene, we assume a perfectly quadratic dispersion relation $\epsilon = p^2/2m$ and relaxation rates that are independent of energy to produce simplified expressions Eqs. 6.13 to 6.16.

We take into account inversion symmetry breaking by disorder and by interlayer asymmetry, the latter may potentially be induced by using an external gate and is thus tunable. In the presence of a tilted field, for the second harmonic, resonances at $\omega_c = \omega$ and $\omega_c = 2\omega$ generally produce currents significantly greater than that at $\omega_c = 0$. In principle, cyclotron resonances could be observed in experiments either as a function of laser frequency ω for fixed ω_c (as in Fig. 6.1) or as a function of cyclotron frequency ω_c for fixed ω (as in Fig. 6.2), and the width of such resonance peaks can be related to the relaxation times τ and τ_2.

Chapter 7

Conclusion

We have introduced Lifshitz transition, non–linear optics and non–linear optical effects, ratchet effect and SHG effect in graphene based structures.

Moreover, we have introduced theoretical background to write low–energy Hamiltonian of bilayer graphene under perpendicular magnetic field. We have considered the orbital effect of an in-plane magnetic field on electrons in bilayer graphene. Previously the orbital effect of an in-plane magnetic field on the electronic spectrum was modelled using the so-called minimal tight-binding model which includes only intralayer and vertical interlayer coupling, accounting for quadratic in magnetic field terms in the low-energy Hamiltonian. At low energy, these terms have a similar effect as homogeneous lateral strain in producing a change in topology of the band structure [49; 50; 72; 73; 74], although, owing to the small interlayer distance, a huge magnetic field of magnitude $\approx 100T$ would be required to observe this. Here, we derived linear-in-field terms in the Hamiltonian arising from skew interlayer coupling and non-uniform on-site energies. We found two types of term: the first has the form of the Lorentz force and it causes the pseudospin (the relative amplitude of the wave function on the two layers) to acquire a small component perpendicular to the graphene plane; the second term is off-diagonal in the layer-space and it creates a small perturbation of the pseudospin direction within the graphene plane. We modelled the influence of these terms on electronic scattering and their manifestation in the magnetic ratchet ef-

fect. We estimate that the effect should be substantial, two orders of magnitude greater than that in monolayer graphene, as well as being sensitive to the nature of disorder and tunable by gate voltage.

In addition, we have shown that the Lifshitz transition of bilayer graphene is strongly related to skew interlayer coupling and interlayer potential asymmetry. Accordingly, there is only one phase with two DPs for bilayer graphene under a magnetic field smaller than something about 138 T and only in certain magnetic field directions. For larger magnetic fields, there are no Dirac Points. While, for zero magnetic field, there are 4 DPs in the phase diagram of bilayer graphene. Whithout considering γ_4 and δ, the phase diagram is schemed in Fig. 4.4 where by the change of the size and the direction of magnetic field, there are three different phases.

In the next step, we have found a first order and a second harmonic generated current in bilayer and monolayer graphene caused by laser radiation. SHG currents are sensitive to the material, monolayer and bilayer graphene, and sensitive to the radiation polarization. In addition, it has been shown that for an unpolarized light a linear polarized light whose direction is proportional to the direction of magnetic field will be produced.

In bilayer graphene in a tilted magnetic field, the dc current has a resonance at $\omega_c = \omega$ but the current value is actually largest at $\omega_c = 0$. For the second harmonic, however, resonances at $\omega_c = \omega$ and $\omega_c = 2\omega$ generally produce currents significantly greater than that at $\omega_c = 0$.

Appendix A

Boltzmann kinetic equation solution for a 2D electron gas under a laser radiation

To calculate the B parameter in Eq. 5.26, we have

$$
\begin{aligned}
B \quad &= \int_0^{2\pi}\int_0^{T} e^{il\omega t}E_y\sin\phi\sum\frac{\mathrm{d}f_m^n}{\mathrm{d}\epsilon}e^{i(m-j)\phi-in\omega t}\frac{\mathrm{d}t}{T}\frac{\mathrm{d}\phi}{2\pi},\\
&= \int_0^{2\pi}\int_0^{T} e^{il\omega t}\left(E_{\parallel x}e^{-i\omega t}+E^*_{\parallel x}e^{-i\omega t}\right)\sin\phi\sum\frac{\mathrm{d}f_m^n}{\mathrm{d}\epsilon}e^{i(m-j)\phi-in\omega t}\frac{\mathrm{d}t}{T}\frac{\mathrm{d}\phi}{2\pi},\\
&= \int_0^{2\pi}\sin\phi\sum\frac{\mathrm{d}f_m^n}{\mathrm{d}\epsilon}e^{i(m-j)\phi}\frac{\mathrm{d}\phi}{2\pi}\int_0^{T} e^{i(l-n)\omega t}\left(E_{\parallel y}e^{-i\omega t}+E^*_{\parallel x}e^{-i\omega t}\right)\frac{\mathrm{d}t}{T},\\
&= \int_0^{2\pi}\sin\phi\sum\frac{\mathrm{d}f_m^n}{\mathrm{d}\epsilon}e^{i(m-j)\phi}\frac{\mathrm{d}\phi}{2\pi}\int_0^{T}\left(E_{\parallel y}e^{i(l-1-n)\omega t}+E^*_{\parallel x}e^{i(l+1+n)\omega t}\right)\frac{\mathrm{d}t}{T},\\
&= \int_0^{2\pi}\sin\phi\sum\frac{\mathrm{d}f_m^n}{\mathrm{d}\epsilon}e^{i(m-j)\phi}\frac{\mathrm{d}\phi}{2\pi}\left(E_{\parallel y}\delta_{n,l-1}+E^*_{\parallel x}\delta_{n,l+1}\right),\\
&= \sum\frac{\mathrm{d}f_m^n}{\mathrm{d}\epsilon}\left(E_{\parallel y}\delta_{n,l-1}+E^*_{\parallel x}\delta_{n,l+1}\right)\int_0^{2\pi}\sin\phi e^{i(m-j)\phi}\frac{\mathrm{d}\phi}{2\pi},\\
&= \sum\frac{\mathrm{d}f_m^n}{\mathrm{d}\epsilon}\left(E_{\parallel y}\delta_{n,l-1}+E^*_{\parallel x}\delta_{n,l+1}\right)\int_0^{2\pi}\frac{-i}{2}\left(e^{i\phi}-e^{-i\phi}\right)e^{i(m-j)\phi}\frac{\mathrm{d}\phi}{2\pi},\\
&= \sum\frac{\mathrm{d}f_m^n}{\mathrm{d}\epsilon}\left(E_{\parallel y}\delta_{n,l-1}+E^*_{\parallel x}\delta_{n,l+1}\right)\int_0^{2\pi}\frac{1}{2}\left(e^{i(m-(j-1))\phi}-e^{i(m-(j+1))\phi}\right)\frac{\mathrm{d}\phi}{2\pi},\\
&= \frac{-i}{2}\sum\frac{\mathrm{d}f_m^n}{\mathrm{d}\epsilon}\left(E_{\parallel y}\delta_{n,l-1}+E^*_{\parallel x}\delta_{n,l+1}\right)\left(\delta_{m,j-1}-\delta_{m,j+1}\right),\\
&= \frac{-i}{2}\left(E_{\parallel x}\frac{\mathrm{d}f_m^{l-1}}{\mathrm{d}\epsilon}+E^*_{\parallel y}\frac{\mathrm{d}f_m^{l+1}}{\mathrm{d}\epsilon}\right)\left(\delta_{m,j-1}-\delta_{m,j+1}\right),\\
&= \frac{-i}{2}\left[E_{\parallel y}\left(\frac{\mathrm{d}f_{j-1}^{l-1}}{\mathrm{d}\epsilon}-\frac{\mathrm{d}f_{j+1}^{l-1}}{\mathrm{d}\epsilon}\right)+E^*_{\parallel y}\left(\frac{\mathrm{d}f_{j-1}^{l+1}}{\mathrm{d}\epsilon}-\frac{\mathrm{d}f_{j+1}^{l+1}}{\mathrm{d}\epsilon}\right)\right].
\end{aligned}
\tag{A.1}
$$

While the calculation of C is similar to B, the calculation of D is similar to A, but the differences come from the prefactor and omit the differential sign for f_m^n. The calculation of the E related part is straights forward and it will be equal to lf_j^l. In addition, the calculations of G related part needs some description. First, we assume that the change of scattering rate δW, which is related to the appearance of the magnetic field, is equal to zero. Hence

$$W_{p'p} = W_{p'p}^0, \quad W_{pp'} = W_{pp'}^0. \tag{A.2}$$

If we assume that $W_{p'p}^0$ is a general function of p and p', then

$$W_{p'p}^0 = g\left(p', p\right) \delta\left(\epsilon_p - \epsilon_{p'}\right), \tag{A.3}$$

where according to the Fermi golden rule

$$g\left(p', p\right) = \frac{2\pi}{\hbar} \left\langle \left|V_{p'p}\right|^2 \right\rangle. \tag{A.4}$$

We can show that $g\left(p', p\right)$ is just dependent on the $\cos\theta_{p'p}$. So

$$\begin{aligned} S\left(f\right) \quad &= \sum_{p'} W_{pp'}^0 f\left(p', t\right) - W_{p'p}^0 f\left(p, t\right), \\ &= \sum_{p'} g\left(p, p'\right) \left(f\left(p', t\right) - f\left(p, t\right)\right) \delta\left(\epsilon_p - \epsilon_{p'}\right), \\ &= \sum_{p'} g\left(p, p'\right) \left(\sum f_m^n e^{im\phi' - in\omega t} - \sum f_m^n e^{im\phi' - in\omega t}\right) \delta\left(\epsilon_p - \epsilon_{p'}\right). \end{aligned} \tag{A.5}$$

After multiplication of above equation by $\int_0^T e^{il\omega t} \mathrm{d}t/T$, $\int_0^{2\pi} e^{-ij\phi} \mathrm{d}\phi/2\pi$, we have

$$G = L^2 \Gamma\left(\epsilon\right) \sum_m f_m^l \int_0^{2\pi} \frac{\mathrm{d}\phi'}{2\pi} \int_0^{2\pi} \frac{\mathrm{d}\phi}{2\pi} g\left(\phi' - \phi\right) \left(e^{im\phi'} - e^{im\phi}\right) e^{-ij\phi}. \tag{A.6}$$

By the change of variables $\theta = \phi' - \phi$ and $\mu = \left(\phi' + \phi\right)/2$, we can show that

$$G = \frac{-L^2 \Gamma\left(\epsilon\right)}{\pi} f_j^l \int_0^{\pi} g\left(\theta\right) \left(1 - \cos j\theta\right) d\theta. \tag{A.7}$$

If we introduce $\tau_{|j|}$, so that

$$\tau_{|j|}^{-1} = \frac{L^2\Gamma(\epsilon)}{\pi}\int_0^\pi g(\theta)(1-\cos j\theta)\,d\theta, \tag{A.8}$$

then, we can write

$$G = -\tau_{|j|}^{-1} f_j^l, \tag{A.9}$$

So, in total the BKE is

$$\begin{aligned}
&\frac{e}{2}\left(\frac{\mathrm{d}\epsilon}{\mathrm{d}p}\frac{\mathrm{d}}{\mathrm{d}\epsilon} - \frac{j-1}{p}\right)\left[\left(E_{\parallel x} - iE_{\parallel y}\right)f_{j-1}^{l-1} + \left(E_{\parallel x}^* - iE_{\parallel y}^*\right)f_{j-1}^{l+1}\right] \\
&+\frac{e}{2}\left(\frac{\mathrm{d}\epsilon}{\mathrm{d}p}\frac{\mathrm{d}}{\mathrm{d}\epsilon} + \frac{j+1}{p}\right)\left[\left(E_{\parallel x} + iE_{\parallel y}\right)f_{j+1}^{l-1} + \left(E_{\parallel x}^* + iE_{\parallel y}^*\right)f_{j+1}^{l+1}\right] \\
&= \left(\tau_{|j|}^{-1} - i\omega l\right)f_j^l,
\end{aligned} \tag{A.10}$$

as described in Eq.5.34. The only difference is that δS_j^l has been added to S_j^l.

Bibliography

[1] H. W. Kroto, J. R. Heath, S. C. O'Brien, R. F. Curl and R. E. Smalley, Nature **56**, 318 (1985).

[2] S. Ijima, Nature **56**, 354 (1991).

[3] S. Ray, *Applications of Graphene and Graphene-Oxide based Nanomaterials* (Elsevier, 2015).

[4] P. Wallace, Phys. Rev. **71**, 622 (1947).

[5] K. Novoselov, A. Geim, S. Morozov, D. Jiang, Y. Zhang, S. Dubonos, I. Grigorieva and A. Firsov, Science **306**, 666 (2004).

[6] K. S. Novoselov, V. I. Fal'ko, L. Colombo, P. R. Gellert, M. G. Schwab and P. Kim, Nature **490**, 192 (2012).

[7] V. Skakalova and A. B. Kaiser, *Graphene: Properties, Preparation, Characterisation and Devices* (Elsevier, 2014).

[8] P. Tassin, T. Koschny and C. M. Soukoulis, Science **341**, 620 (2014).

[9] C. Lee, X. Wei, J. W. Kysar and J. Hone, Science **321**, 385 (2008).

[10] A. K. Geim and K. S. Novoselov, Nat. Mater. **6**, 183 (2007).

[11] L. Ju, B. Geng, J. Horng, C. Girit, M. Martin, Z. Hao, H. A. Bechtel, X. Liang, A. Zettl, Y. R. Shen and F. Wang, Nat. Nanotechnol. **6**, 630 (2011).

[12] Y. M. Lin, C. Dimitrakopoulos, K. A. Jenkins, D. B. Farmer, H. -Y. Chiu, A. Grill and Ph. Avouris, Science **327**, 662 (2010).

[13] E. McCann, *Graphene Nanoelectronics*, 237 (Springer, Berlin Heidelberg, 2012).

[14] N. Kheirabadi, RSC Adv. **6**, 18156 (2016).

[15] A. H. Castro Neto, F. Guinea, N. M. R. Peres, K. S. Novoselov and A. K. Geim, Rev. Mod. Phys. **81**, 109 (2009).

[16] Y.Zhang, Z. Jiang, J. P. Small, M. S. Purewal, Y. -W. Tan, M. Fazlollahi, J. D. Chudow, J. A. Jaszczak, H. L. Stormer and P. Kim, Phys. Rev. Lett. **96**, 136806 (2006).

[17] E. Mostaani, N. Drummond and V. I. Fal'ko. Phys. Rev. Lett. **115**, 115501 (2015).

[18] K. S. Novoselov, E. McCann, S. V. Morozov, V. I. Fal'ko, M. I. Katsnelson, U. Zeitler, D. Jiang, F. Schedin and A. K. Geim, Nat. Phys. **2**, 177 (2006).

[19] E. McCann and V. I. Fal'ko, Phys. Rev. Lett. **96**, 086805 (2006).

[20] E. McCann and M. Koshino, Rep. Prog. Phys. **76**, 056503 (2013).

[21] M. Mucha-Kruczyski, I. L. Aleiner and V. I. Fal'ko, Phys. Rev. B. **84**, 041404 (2011).

[22] G. New, *Introduction to nonlinear optics* (Cambridge University, 2011).

[23] F. Bonaccorso, Z. Sun, T. Hasan and A. C. Ferrari. Nat. Photonics **4**, 611 (2010).

[24] C. Casiraghi, A. Hartschuh, E. Lidorikis, H. Qian , H. Harutyunyan, T. Gokus, K. S. Novoselov and A. C. Ferrari, Nano Lett. **7**, 2711 (2007).

[25] P. Blake, E. W. Hill, A. H. Castro Neto, K. S. Novoselov, D. Jiang, R. Yang and A. K. Geim, App. Phys. Lett. **91**, 063124 (2007).

[26] R. R. Nair, P. Blake, A. N. Grigorenko, K. S. Novoselov, T. J. Booth, T. Stauber, N. M. Peres and A. K. Geim, Science **6**, 1308 (2008).

[27] K. F. Mak, M. Y. Sfeir, Y. Wu, CH. Lui and J. A. Misewich, Phys. Rev. Lett. **101**, 196405 (2008).

[28] Z. Q. Li, E. A. Henriksen, Z. Jiang, Z. Hao, M. C. Martin, P. Kim, H. L. Stormer and D. N. Basov, Nat. Phys **4**, 532 (2008).

[29] C. Drexler, S. A. Tarasenko, P. Olbrich, J. Karch, M. Hirmer, F. Muller, M. Gmitra, J. Fabian, R. Yakimova, S. Lara-Avila, S. Kubatkin, M. Wang, R. Vajtai, P. M. Ajayan, J. Kono and S. D. Ganichev, Nat. Nanotechnol. **8**, 104 (2013).

[30] P. Olbrich, J. Kamann, M. Knig, J. Munzert, L. Tutsch, J. Eroms, D. Weiss, M. -H. Liu, L. E. Golub, E. L. Ivchenko, V. V. Popov, D. V. Fateev, K. V. Mashinsky, F. Fromm, Th. Seyller and S. D. Ganichev, Phys. Rev. B **93**, 075422 (2016).

[31] V. I. Fal'ko, Sov. Phys. Solid State **31**, 561 (1989).

[32] J. J. Dean and H. M. van Driel. App. Phys. Lett. **28**, 261910 (2009).

[33] A. Y. Bykov, T. V. Murzina, M. G. Rybin and E. D. Obraztsova. Phys. Rev. B **85**, 121413 (2012).

[34] R. Saito, G. Dresselhaus and M. S. Dresselhaus, World Scientific (1998).

[35] W. A. Harrison, *Solid State Theory* (McGraw Hill, New York, 1970).

[36] C. Kittel, *Quantum Theory of Solids* (John Wiley, New York,1963).

[37] E. Kogan and V. Nazarov, Phys. Rev. B **85**, 115418 (2012).

[38] N. W. Ashcroft and N. D. Mermin ND, *Solid State Physics* (Holt, Rinehart and Winston, New York, 1976).

[39] J. Nilsson, A. H. Castro Neto, F. Guinea and N. M. R. Peres, Phys. Rev. B **78**, 045405 (2008).

[40] P. San-Jose, E. Prada, E. McCann and H. Schomerus, Phys. Rev. Lett. **102**, 247204 (2009).

[41] S. A. Tarasenko, Phys. Rev. B **77**, 085328 (2008).

[42] M. B. Lundeberg and J. A. Folk, Nat. Phys. **5**, 894 (2009).

[43] R. Peierls, Z. Phys. **80**, 763 (1933).

[44] K. Kechedzhi, E. McCann, V. I. Fal'ko, H. Suzuura, T. Ando and B. L. Altshuler, Eur. Phys. J. Special Topics **148**, 39 (2007).

[45] S. S. Pershoguba and V. M. Yakovenko, Phys. Rev. B **82**, 205408 (2010).

[46] B. Roy and K. Yang, Phys. Rev. B **88**, 241107(R) (2013).

[47] M. Van der Donck, F. M. Peeters and B. Van Duppen, Phys. Rev. B **93**, 115423 (2016).

[48] E. Mariani, A. J. Pearce and F. von Oppen, Phys. Rev. B **86**, 165448 (2012).

[49] M. Mucha-Kruczyski, A. I. L. Aleiner and V. I. Fal'ko, Phys. Rev. B **84**, 041404 (2011).

[50] Y. -W. Son, S. -M. Choi, Y. P. Hong, S. Woo and S. -H. Jhi, Phys. Rev. B **84**, 155410 (2011).

[51] S. A. Tarasenko, Phys. Rev. B **83**, 035313 (2011).

[52] M. M. Glazov and S. D. Ganichev, Phys. Rep. **535**, 101 (2014).

[53] H. Haug and S. W. Koch, World Scientific **5**, 1990.

[54] S. Datta, *Electronic transport in mesoscopic systems* (Cambridge university press, 1997).

[55] A. V. Nalitov, L. E. Golub and E. L. Ivchenko, Phys. Rev. B **86**, 115301 (2012).

[56] N. Kheirabadi, E. McCann and V. I. Fal'ko, Phys. Rev. B **94**, 165404 (2016).

[57] S. Adam and S. D. Sarma, Phys. Rev. B **77**, 115436 (2008).

[58] L. M. Zhang, Z. Q. Li, D. N. Basov, M. M. Fogler, Z. Hao and M. C. Martin, Phys. Rev. B **78**, 235408 (2008).

[59] G. V. Budkin and S. A. Tarasenko, Phys. Rev. B **93**, 075306 (2016).

[60] Z. Sun, A. Martinez and F. Wang, Nat. Photonics **40**, 227 (2016).

[61] H. Yan, X. Li, B. Chandra, G. Tulevski, Y. Wu, M. Freitag, W. Zhu, P. Avouris and F. Xia. Nat. Nanotechnol. **7**, 330 (2012).

[62] S. H. Lee, M. Choi, T. -T. Kim, S. Lee, Ming Liu, X. Yin, H. K. Choi, S. S. Lee, C. -Gi Choi, S. -Y Choi, X. Zhan and B. Min, Nat. Mater. **11**, 936 (2012).

[63] N. Papasimakis, Z. Luo, Z. X. Shen, F. De Angelis, E. Di Fabrizio, A. E. Nikolaenko and N. I. Zheludev, Opt. Express **18** , 8353 (2010).

[64] Y. Yao, R. Shankar, M. A. Kats, Y. Song, J. Kong, M. Loncar and F. Capasso, Nano Lett. **14** , 6526 (2014).

[65] L. Ju, B. Geng, J. Horng, C. Girit, M. Martin, Z. Hao, H. A. Bechtel, X. Liang, A. Zettl, Y. Ron Shen and F. Wang, Nat. Nanotechnol. **6**, 630 (2011).

[66] R. Shimano, G. Yumoto, J. Y. Yoo, R. Matsunaga, S. Tanabe, H. Hibino, T. Morimoto and H. Aoki, Nat. Commun. **4**, 1841 (2013).

[67] J. Schiefele, L. Martin-Moreno and F. Guinea, Phys. Rev. B **94**, 035401 (2016).

[68] S. D. Sarma, S. Adam, E. H. Hwang and E. Rossi, Rev. Mod. Phys. **83**, 407 (2011).

[69] I. T. Lin, *Optical properties of graphene from the THz to the visible spectral region* (University of California, USA, 2012).

[70] S. D. Sarma, S. Adam, E. H. Hwang and E. Rossi, Rev. Mod. Phys **83**, 407 (2011).

[71] N. Kheirabadi, E. McCann and V. I. Fal'ko. arXiv:1711.05513 (2017).

[72] E. Mariani, A. J. Pearce and F. von Oppen, Phys. Rev. B **86**, 165448 (2012).

[73] W. -Y. He, Y. Su, M. Yang and L. He, Phys. Rev. B **89**, 125418 (2014).

[74] M. Van der Donck, F. M. Peeters and B. Van Duppen, Phys. Rev. B **93**, 247401 (2016).